DETECTION OF THE INVERSION LAYER OVER THE CENTRAL NORTH PACIFIC OCEAN USING GPS RADIO OCCULTATION

A THESIS SUBMITTED TO THE GRADUATE DIVISION OF THE UNIVERSITY OF HAWAI'I AT MĀNOA IN PARTIAL FULFILLMENT OF THE REQUIREMENTS FOR THE DEGREE OF

MASTER OF SCIENCE

IN

METEOROLOGY

AUGUST 2014

By

Thomas E. Winning Jr.

Thesis Committee:

Yi-Leng Chen, Chairperson
Gary Barnes
Michael Bell
Jennifer Griswold

Acknowledgments

I would first like to thank my advisor, Dr. Yi-Leng Chen for his help, guidance, and patience through this entire process. It has been a struggle at times, but it was worth it. I would also like to thank Dr. Gary Barnes, Dr. Michael Bell, and Dr. Jennifer Griswold for the edits, reviews, and general motivation that was necessary in keeping this process moving in the right direction. I also owe many thanks to Tom Robinson for all of the help with Fortran90 programming and Gary Grunseich and Kavina Dayal likewise, for their help with Matlab. I would also like to extend my gratitude to Feng Hsiao for the work put in over the last couple of years to generate the WRF data and David Hitzl for taking time away from his work to provide whatever data graphics from the WRF model I requested, especially the integration of the refractivity values.

Abstract

Sparse observations over the central North Pacific have inhibited our understanding of the spatial variations of the trade wind inversion. Since the launch of the Constellation Observing System for Meteorology, Ionosphere, and Climate (COSMIC) in 2006, Global Positioning System radio occultation (GPS RO) observations allow for high-resolution atmospheric profiling with a vertical resolution on the order of 100 m to be extended over the open ocean where conventional data are sparse. In this study, the GPS RO data during the years 2006-2012 will be used to study the spatial variations of the inversion throughout the annual cycle over the region 5°N-45°N and 120°W-180°W. In addition, the impacts of El Niño and the diurnal heating cycle on the spatial and temporal variations of the inversion base height were also examined.

Identification of the horizontal distribution of the inversion was achieved by combining seasonal data for the years 2007-2012 over the entire domain into 5° x 5° grids. The resulting horizontal distribution showed an annual difference in inversion height of approximately 200 m in the wake of the islands. When low level flow was restricted to northeasterly trade wind flow, the inversion base heights increased for each season, however the annual difference remained 200 m. Comparisons between El Niño and La Niña events as well as the diurnal variation during the summer season show a difference in the height of the inversion base of approximately 100 m, however, a larger data sample would be desirable for a more robust analysis.

A two-tailed t test was performed for three 2.5° x 2.5° grid boxes in the wake of the islands to compare the annual variation of the inversion base height. The annual change within each of the two western most grid boxes is statistically significant at a 95% confidence interval. The third point, immediately downwind of the Big Island only showed a significant difference when low level flow was restricted to trade wind flow. The goal of this thesis is to determine if the effect the Hawaiian Islands have on the otherwise uniform flow within the marine boundary layer (BL) is detectable by the GPS RO observations method.

Table of Contents

Acknowledgments……..ii
Abstract…….……iii
Table of Contents……...……iv
List of Tables…….……vi
List of Figures…….……..vii
Chapter 1. Introduction…….……1
1.1 Overview.....1
1.2 Horizontal Distribution of Inversion Height..……2
1.3 Refractivity Measured Inversion Base Height...……3
1.4 Motivation..……6
1.5 Objectives...……7
Chapter 2. Climatology..……9
2.1 Sea Level Pressure ……9
2.2 Surface Wind……12
2.3 250 hPa Wind ..……13
2.4 Vertical Velocity……..16
2.5 ENSO Influence…….. ….17
2.5.1 El Niño…… 17
2.5.2 La Niña……....20
Chapter 3. Data and Procedures…….….……..23
3.1 Data…….. ……23
3.1.1 Constellation Observing System for Meteorology, Ionosphere, and Climate (COSMIC) ……..23
3.1.2 National Center for Environmental Prediction-Final (NCEP-FNL)……....23
3.1.3 El Niño-Southern Oscillation (ENSO) Index……..…….…...24
3.1.4 CMORPH Precipitation Estimates…….…….25
3.1.5 High Resolution WRF-ARW 6km……..……25
3.2 Procedures……..……..26
3.2.1 Grid Size Selection and Observation Distribution…….…….26
3.2.2 Refractivity to Identify Inversion Base Height……..27
3.2.3 Relative Minimum Gradient (RMG)……..…….29
3.2.4 Base and Height Constraints…….……..29
3.2.5 Sounding Examples…….……30
3.2.6 Uncertainties in GPS RO Measurements……..……..33
Chapter 4. Results: GPS RO Observation of Inversion Base Height…… ……...35
4.1 Annual Climatology…….……...35
4.1.1 JJA 2007-2012……. ……...35
4.1.2 DJF 2007-2012…….……...38
4.2 Trade Wind Flow Climatology…….. ……..41
4.2.1 JJA 2007-2012 Trade Wind Flow……..…….42
4.2.2 DJF 2007-2012 Trade Wind Flow…….. ……44

4.2.3 Annual Climatology Comparison……..……...47
4.3 Diurnal Variation of Inversion Base Height……. ……...48
4.3.1 Diurnal Climatology Comparison…….……..51
4.4 Observations of Inversion Base Height during ENSO……. ……...52
4.4.1 El Niño-2010……..……52
4.4.2 La Niña-2011……...……54
Chapter 5. Statistical Analysis and Model Comparison……...55
5.1 GPS RO Difference Comparison…….. ……...59
5.1.1 Climatology Difference……...59
5.1.2 Trade Wind Climatology Difference……..…….60
5.2 JJA Inversion Base Height (z_i) in the Wake…….……61
5.2.1 Precipitable Water……..…….61
5.2.2 CMORPH……64
5.2.3 WRF-ARW 6km……...……... ...65
Chapter 6. Summary and Conclusion……...76
6.1 Summary ……..76
6.2 Conclusion ……...79
6.3 Future Work…….……80
Appendix 1. GPS RO Observation Case Study……82
A.1.1 One Day Observation Period…….……...82
A.1.2 One Week Observation Period……83
A.1.3 One Month Observation Period……. ……..85
A.1.4 Observation and Interpolation…….……88
Appendix 2. Sample Soundings…… .……89
Appendix 3. Additional GPS RO Observations…….….92
Appendix 4. Calendar of Trade Wind Dates…… ……97
Appendix 5. Two-Tailed test……..101
Bibliography…….……..114

List of Tables

Table 3.1. Total global and domain observations for JJA 2007-2012 and DJF 2007-2012. Domain defined as 5˚N-45˚N and 180˚W-120˚W……23

Table 3.2. Seasonal average of the total number of observations per grid box over the Hawaiian region 5°N – 45°N and 180°W – 120°W…….26

Table 3.3. Comparison of basic RO criteria (minimum and maximum height constraints and refractivity values) from previous research (Guo et al. 2011; Ao et al. 2012; Xie et al.2012) …….30

Table 4.1. Comparison between GPS RO and radiosonde observations of inversion base height, z_i (km) (Bingaman 2005) …….46

Table 4.2. Comparison between GPS RO and radiosonde observations of inversion base height, z_i (km) (Bingaman 2005)……..51

Table A.5.1. Calendar of trade wind climatology dates for JJA 2007-2012……97

Table A.5.2. Calendar of trade wind climatology dates for DJF 2007-2012……...99

List of Figures

Figure 1.1 Vertical cross section of the boundary layer (BL) over the Pacific Ocean. consisting of the subcloud layer, cloud layer and inversion. The inversion layer marks the boundary between the BL and and free atmosphere. (Malkus 1958)……..…3

Figure 1.2. Illustration of the progression of a radio occultation. The tangent point is the point which the radio wave between a GPS and LEO satellite comes in contact with Earth's atmosphere while passing between the two satellites. The COMET® Program - The University Corporation for Atmospheric Research, 2014 ……4

Figure 1.3. Analysis region (5˚N-45˚N, 120˚W-180˚W) and approximate locations of Hilo and Lihu'e stations ……...…7

Figure 2.1. NCEP-FNL sea-level pressure (hPa) climatology for JJA 2007-2012….10

Figure 2.2. NCEP-FNL sea-level pressure (hPa) climatology for SON 2007-2012...10

Figure 2.3. NCEP-FNL sea-level pressure (hPa) climatology for DJF 2007-2012…11

Figure 2.4. NCEP-FNL sea-level pressure (hPa) climatology for MAM 2007-2012.11

Figure 2.5. Mean surface wind vectors (m s^{-1}) and isotachs (2 m s^{-1}) for JJA 2007-2012 from NCEP-FNL……..12

Figure 2.6. Mean surface wind vectors (m s^{-1}) and isotachs (2 m s^{-1}) for DJF 2007-2012 from NCEP-FNL……..13

Figure 2.7. Mean 250 hPa wind vectors (m s^{-1}) and isotachs (10 m s^{-1}) for JJA 2007-2012 from NCEP-FNL……..14

Figure 2.8. Mean 250 hPa wind vectors (m s^{-1}) and isotachs (10 m s^{-1}) for SON 2007-2012 from NCEP-FNL…….14

Figure 2.9. Mean 250 hPa wind vectors (m s^{-1}) and isotachs (10 m s^{-1}) for DJF 2007-2012 from NCEP-FNL…….15

Figure 2.10. Mean 250 hPa wind vectors (m s^{-1}) and isotachs (10 m s^{-1}) for MAM 2007-2012 from NCEP-FNL…….15

Figure 2.11. NCEP-FNL ω_{500} vertical velocities in Pa s^{-1} climatology for JJA 2007-2012. Positive values indicate rising motion and negative values indicate sinking motion.……..16

Figure 2.12. NCEP-FNL ω_{500} vertical velocities in Pa s^{-1} climatology for DJF 2007-2012. Positive values indicate rising motion and negative values indicate sinking motion 17

Figure 2.13. NCEP-FNL sea-level pressure (hPa) climatology for DJF 2010 El Niño from NCEP-FNL.....18

Figure 2.14. Mean surface wind vectors (m s^{-1}) and isotachs (2 m s^{-1}) for DJF 2010 El Niño from NCEP-FNL……18

Figure 2.15. NCEP-FNL ω_{500} vertical velocities in Pa s^{-1} climatology for DJF 2010 El Niño. Positive values indicate rising motion and negative values indicate sinking motion……...19

Figure 2.16. Mean 250 hPa wind vectors (m s^{-1}) and isotachs (10 m s^{-1}) for DJF 2010 El Niño from NCEP-FNL.....19

Figure 2.17. NCEP-FNL sea-level pressure (hPa) climatology for DJF 2011 La Niña from NCEP-FNL.....20

Figure 2.18. Mean surface wind vectors (m s^{-1}) and isotachs (2 m s^{-1}) for DJF 2011 La Niña from NCEP-FNL.....21

Figure 2.19. NCEP-FNL ω_{500} vertical velocities in Pa s^{-1} climatology for DJF 2010 La Niña. Positive values indicate rising motion and negative values indicate sinking motion……...21

Figure 2.20. Mean 250 hPa wind vectors (m s^{-1}) and isotachs (10 m s^{-1}) for DJF 2011 La Niña from NCEP-FNL…….22

Figure 3.1. Multivariate ENSO index 1950-Present. Positive standard departures (red) represent El Niño events and negative standard departures (blue) represent La Niña events. El Niño (2010) and La Niña (2011) events used for this study are highlighted by green box. (http://www.esrl.noaa.gov/psd/enso/mei/ 2014)…24

Figure 3.2. Average distribution of GPS RO observations per 5˚x5˚ grid box for annual climatology JJA 2007-2012 …….27

Figure 3.3. Left - Vertical profiles of refractivity in N-units (blue solid), temperature in ˚C (green dashed), water vapor partial pressure in hPa (red dashed), and mixing ratio in g kg^{-1} (purple dotted). Right – Vertical profiles of refractivity gradient equation components (N' - blue solid), temperature (N_T' – green dashed), water vapor pressure (N_W' – red dashed), and mixing ratio (N_P' – purple dotted). From Ao et al. 2012 ……28

Figure 3.4. Example sounding from 2234 HST 2 June, 2007. The blue line (left) represents the dewpoint temperature profile. The black line (right) represents the temperature profile. Red arrow illustrates the reference pressure level of minimum refractivity gradient. Sounding data was obtained from the Taiwan Analysis Center for COSMIC (http://tacc.cwb.gov.tw/cdaac/ 2014)……...31

Figure 3.5. Example skew-t sounding from 0942 HST 18 July, 2011. The blue line (left) represents the dewpoint temperature profile. The black line (right) represents the temperature profile. Red arrow illustrates the reference pressure level of minimum refractivity gradient. Sounding data was obtained from the Taiwan Analysis Center for COSMIC (http://tacc.cwb.gov.tw/cdaac/ 2014) ……..32

Figure 3.6. Example sounding from 1048 HST 29 July, 2007. The blue line (left) represents the dewpoint temperature profile. The black line (right) represents the temperature profile. Red arrow illustrates the reference pressure level of minimum refractivity gradient. Sounding data was obtained from the Taiwan Analysis Center for COSMIC (http://tacc.cwb.gov.tw/cdaac/ 2014) ……..33

Figure 4.1. Central North Pacific analysis region (5˚N - 45˚N, 120˚W - 180˚W). Red dots show center of each 5˚x 5˚ analysis grid ……..35

Figure 4.2. Median inversion base height (km) for JJA 2007-2012 ……...36

Figure 4.3. Standard deviation (km) of median inversion base height for JJA 2007-2012. .....……37

Figure 4.4. Median relative minimum gradient (unitless) for JJA 2007-2012……37

Figure 4.5. Horizontal distribution of GPS RO observations per 5˚x5˚ grid point for JJA 2007 – 2012.…….……38

Figure 4.6. Median inversion base height (km) DJF 2007 – 2012.…….39

Figure 4.7. Standard deviation (km) of median inversion base height for DJF 2007 – 2012.…….39

Figure 4.8. Median relative minimum gradient (unitless) for DJF 2007 – 2012.……40

Figure 4.9. Horizontal distribution of GPS RO observations per 5˚x5˚ grid point for DJF 2007 - 2012.……..40

Figure 4.10. Example of undisturbed trade wind flow from NCEP-FNL MSLP (00Z 18 July 2012)……41

Figure 4.11. Example of disturbed trade wind flow from MSLP from NCEP-FNL (00Z 18 August 2009)……..42

Figure 4.12. Median inversion base height (km) for JJA 2007-2012 trade wind flow. ……..43

Figure 4.13. Median relative minimum gradient (unitless) for JJA 2007-2012 trade wind flow…….……43

Figure 4.14. Horizontal distribution of GPS RO observations per 5˚x5˚ grid point (JJA 2007 – 2012) trade wind flow. 44

Figure 4.15. Median inversion base height (km) DJF 2007 – 2012 trade wind flow… ..……45

Figure 4.16. Median relative minimum gradient (unitless) for DJF 2007 – 2012 trade wind flow. 45

Figure 4.17. Horizontal distribution of GPSRO observations per 5˚x5˚ grid point (DJF 2007 - 2012) trade wind flow.....46

Figure 4.18. Median inversion base height (km) for JJA-Day (1200-1800 HST).….49

Figure 4.19. Median inversion base height (km) for JJA-Night (0000-0600 HST)....49

Figure 4.20. Median relative minimum gradient (unitless) for JJA-Day....……50

Figure 4.21. Median relative minimum gradient (unitless) for JJA-Night.……..50

Figure 4.22. Median inversion base height (km) for El Niño (DJF 2010).……53

Figure 4.23. Median relative minimum gradient (unitless) for El Niño (DJF 2010)..53

Figure 4.24. Median inversion base height (km) for La Niña (DJF 2011). ……54

Figure 4.25. Median relative minimum gradient (unitless) for La Niña (DJF 2011). .....……..55

Figure 5.1. Representation of 2.5 degree analysis region (12.5˚N-37.5˚N, 147.5˚W-170˚W). Red dots mark the center of each 2.5˚ x 2.5˚ degree grid point.…...56

Figure 5.2. Median inversion base height (km) for JJA-C 2007-2012 for 12.5˚N-37.5˚N, 147.5˚W-170˚W (2.5˚x2.5˚ grid). Area within black box is the approximate domain of the JJA precipitable water climatology for 2007-2012 from the WRF-ARW in Figure 5.8 and precipitation climatology from CMORPH Figure 5.10. Black dash-dot line is the approximate location of 159˚W longitude transect for Figures 5.11, 5.13, and 5.15 and black dotted line is the approximate location of 153˚W-160˚W diagonal transect to be used for Figures 5.17, 5.18, and 5.21. ……..57

Figure 5.3. Median inversion base height (km) for DJF-C 2007-2012 for 12.5˚N-37.5˚N, 147.5˚W-170˚W (2.5˚x2.5˚ grid). Area within black box is the approximate domain of the DJF precipitable water climatology for 2007-2012 from the WRF-ARW in Figure 5.9. Black dash-dot line is the approximate location of 159˚W longitude transect for Figures 5.12, 5.14, and 5.16 and black dotted line is the approximate location of 153˚W-160˚W diagonal transect to be used for Figures 5.19, 5.20, and 5.22.……57

Figure 5.4. Median inversion base height (km) for JJA-TW 2007-2012 for 12.5˚N-37.5˚N, 147.5˚W-170˚W (2.5˚x2.5˚ grid). ……58

Figure 5.5. Median inversion base height (km) for JJA 2007-2012 for 12.5˚N-37.5˚N, 147.5˚W-170˚W (2.5˚x2.5˚ grid). 58

Figure 5.6. Climatology difference (JJA-C minus DJF-C) of GPS RO observed median inversion base height (km). Locations of the analyzed annual difference are marked by a red square (17.5˚N-165˚W), blue square (22.5˚N-162.5˚W), and green square (20˚N-157.5˚W).……60

Figure 5.7. Trade wind climatology difference (JJA-TW minus DJF-TW) of GPS RO observed median inversion base height (km). Locations of the analyzed annual difference are marked by a red square (17.5˚N-165˚W), blue square (22.5˚N-162.5˚W), and green square (20˚N-157.5˚W)……..61

Figure 5.8. Total precipitable water (mm) for JJA 2007-2012 from WRF-ARW 6 km. *Courtesy of David Hitzl ……62

Figure 5.9. Total precipitable water (mm) for DJF 2007-2012 from WRF-ARW 6 km. *Courtesy of David Hitzl ……63

Figure 5.10. CMORPH rainfall climatology (mm) for JJA 2004-2012 (0.25˚). *Courtesy of Yu-Feng Huang ……..64

Figure 5.11. JJA-C 2007-2012 6 km WRF-ARW vertical transect along 159˚W (black dash-dot line in Figure 5.2) of relative humidity (%) and zonal wind speed (filled background contours m s^{-1}). *Courtesy of David Hitzl……...65

Figure 5.12. DJF-C 2007-2012 6 km WRF-ARW vertical transect along 159˚W (black dash-dot line in Figure 5.3) of relative humidity (%) and zonal wind speed (filled background contours m s^{-1}). *Courtesy of David Hitzl ……..66

Figure 5.13. JJA-C 2007-2012, 6 km WRF-ARW vertical transect along 159˚W (black dash-dot line in Figure 5.2) of vertical motion (black contour in cm s^{-1}) with rising motion > 0 and sinking motion < 0, and wind speed (filled background contours m s^{-1}). *Courtesy of David Hitzl……67

Figure 5.14. DJF-C 2007-2012, 6 km WRF-ARW vertical transect along 159˚W (black dash-dot line in Figure 5.3) of vertical motion (black contour in cm s^{-1}) with rising motion > 0 and sinking motion < 0, and wind speed (filled background contours m s^{-1}). *Courtesy of David Hitzl……67

Figure 5.15. JJA-C 2007-2012, 6 km WRF-ARW vertical transect along 159˚W (black dash-dot line in Figure 5.2) of dN/dp (black contour in N-units hPa^{-1}) and wind speed (filled background contours m s^{-1}). *Courtesy of David Hitzl.…….68

Figure 5.16. DJF-C 2007-2012, 6 km WRF-ARW vertical transect along 159˚W (black dash-dot line in Figure 5.3) of dN/dp (black contour in N-units hPa^{-1}) and wind speed (filled background contours m s^{-1}). *Courtesy of David Hitzl.…….69

Figure 5.17. JJA-C 2007-2012, vertical cross section along diagonal 153˚W-159˚W (black dotted line in Figure 5.2) of relative humidity (black contour in %) and wind speed (filled background contours m s^{-1}). *Courtesy of David Hitzl….70

Figure 5.18. JJA-C 2007-2012, vertical cross section along diagonal 153˚W-159˚W (black dotted line in Figure 5.2) of vertical motion (black contour in cm s^{-1}) with rising motion > 0 and sinking motion < 0, and wind speed (filled background contours m s^{-1}). *Courtesy of David Hitzl ……..71

Figure 5.19. DJF-C 2007-2012, vertical cross section along diagonal 153˚W-159˚W (black dotted line in Figure 5.3) of relative humidity (black contour in %) and wind speed (filled background contours m s^{-1}). *Courtesy of David Hitzl….71

Figure 5.20. DJF-C 2007-2012, vertical cross section along diagonal 153˚W-159˚W (black dotted line in Figure 5.3) of vertical motion (black contour in cm s^{-1}) with rising motion > 0 and sinking motion < 0, and wind speed (filled background contours m s^{-1}). *Courtesy of David Hitzl ……..72

Figure 5.21. JJA-C 2007-2012, vertical cross section along diagonal 153˚W-159˚W (black dotted line in Figure 5.2) of dN/dp (black contour in N-units hPa^{-1}) and wind speed (filled background contours m s^{-1}). Courtesy of David Hitzl …..72

Figure 5.22. DJF-C 2007-2012, vertical cross section along diagonal 153˚W-159˚W (black dotted line in Figure 5.3) of dN/dp (black contour in N-units hPa^{-1}) and wind speed (filled background contours m s^{-1}). Courtesy of David Hitzl …..73

Figure 5.23. Horizontal view of 6km WRF showing wind vectors, wind speed (color fill in m s^{-1}), vertical motion (cm s^{-1}) for JJA-C 2007-2012. . Black dash-dot line is the approximate location of 159˚W longitude transect used for Figures 5.11, 5.13, and 5.15; and black dotted line is the approximate location of 153˚W-159˚W diagonal transect used for Figures 5.17, 5.18, and 5.21. *Courtesy of David Hitzl..……75

Figure 5.24. Horizontal view of 6km WRF showing wind vectors, wind speed (color fill in m s^{-1}), vertical motion (cm s^{-1}) for DJF-C 2007-2012. . Black dash-dot line is the approximate location of 159˚W longitude transect used for Figures 5.12, 5.14, and 5.16; and black dotted line is the approximate location of 153˚W-159˚W diagonal transect used for Figures 5.19, 5.20, and 5.22. *Courtesy of David Hitzl.....75

Figure A.1.1. Map of GPS RO analysis region (5˚N-45˚N,120˚W-180˚W). Red crosses show the location (surface coordinates) of each observation occurred during the 24 hour period of 21 July, 2010. ……..82

Figure A.1.2. Map of GPS RO analysis region (5˚N-45˚N,120˚W-180˚W). Red crosses show the location (surface coordinates) of each observation which occurred during the 24 hour period of 21 January, 2010 ……83

Figure A.1.3. Map of GPS RO analysis region (5˚N-45˚N, 120˚W-180˚W). Red crosses show the location (surface coordinates) of each observation which occurred during the week of 4 July, 2010 – 11 July, 2010 ……84

Figure A.1.4. Median z_i over the analysis (5˚N-45˚N, 120˚W-180˚W) during the week of 4 July, 2010 – 11 July, 2010…….84

Figure A.1.5. Map of GPS RO analysis region (5˚N-45˚N, 120˚W-180˚W). Red crosses show the location (surface coordinates) of each observation which occurred during the week of 4 January, 2010 – 11 January, 2010……..85

Figure A.1.6. Median z_i over the analysis (5˚N-45˚N, 120˚W-180˚W) during the week of 4 January, 2010 – 11 January, 2010…….85

Figure A.1.7. Map of GPS RO analysis region (5˚N-45˚N, 120˚W-180˚W) during the month of July 2010. Red crosses show the location (surface coordinates) of each observation ……...86

Figure A.1.8. Median z_i over the analysis (5˚N-45˚N, 120˚W-180˚W) during the month of July 2010……..87

Figure A.1.9. Map of GPS RO analysis region (5˚N-45˚N, 120˚W-180˚W) during the month of January 2010. Red crosses show the location (surface coordinates) of each observation……...87

Figure A.1.10. Median z_i over the analysis (5˚N-45˚N, 120˚W-180˚W) during the month of January 2010 ……88

Figure A.2.1. Example sounding from 0820 HST 23 July, 2008. The blue line (left) represents the dewpoint temperature profile. The black line (right) represents the temperature profile. Red arrow illustrates the reference pressure level of the minimum refractivity gradient. Location of observation is approximately 17.49˚N – 163.58˚W. Inversion base is observed at the approximate height of 2.1 km and a corresponding pressure level of 794 hPa. Sounding data was obtained from the Taiwan Analysis Center for COSMIC (http://tacc.cwb.gov.tw/cdaac/ 2014)..89

Figure A.2.2. Example sounding from 1145 HST 25 July, 2010. The blue line (left) represents the dewpoint temperature profile. The black line (right) represents the temperature profile. Red arrow illustrates the reference pressure level of minimum refractivity gradient. Location of observation is approximately 19.51˚N – 160.27˚W. Inversion base is observed at the approximate height of 2.1 km and a corresponding pressure level of 807 hPa. Sounding data was obtained from the Taiwan Analysis Center for COSMIC (http://tacc.cwb.gov.tw/cdaac/ 2014)..90

Figure A.2.3. Example sounding from 0419 HST 10 July, 2007. The blue line (left) represents the dewpoint temperature profile. The black line (right) represents the temperature profile. Red arrow illustrates the reference pressure level of minimum refractivity gradient. Location of observation is approximately 19.58˚N – 164.25˚W. Inversion base is observed at the approximate height of 2.1 km and a corresponding pressure level of 795 hPa. Sounding data was obtained from the Taiwan Analysis Center for COSMIC (http://tacc.cwb.gov.tw/cdaac/ 2014)..91

Figure A.3.1. Climatology standard deviation (km) of RMG (unitless) for JJA-C 2007-2012 over 5˚x5˚analysis region (5˚N-45˚N, 120˚W-180˚W) ……92

Figure A.3.2. Climatology standard deviation (km) of RMG (unitless) for DJF-C 2007-2012 over 5˚x5˚analysis region (5˚N-45˚N, 120˚W-180˚W) ……92

Figure A.3.3. Standard deviation of median inversion base height (km) for JJA 2007-2012 trade wind flow (5˚N-45˚N, 120˚W-180˚W) ……..93

Figure A.3.4. Trade wind climatology standard deviation (km) of RMG (unitless) for JJA-TW 2007-2012 over 5˚x5˚analysis region (5˚N-45˚N, 120˚W-180˚W)...93

Figure A.3.5. Figure A.3.5. Standard deviation (km) of median inversion base height for DJF 2007 – 2012 trade wind flow over 5˚x5˚analysis region (5˚N-45˚N, 120˚W-180˚W) 94

Figure A.3.6. Trade wind climatology standard deviation (km) of RMG (unitless) for DJF-TW 2007-2012 over 5˚x5˚analysis region (5˚N-45˚N, 120˚W-180˚W)...94

Figure A.3.7. Median inversion base height standard deviation (km) for El Niño (DJF 2010) over 5˚x5˚analysis region (5˚N-45˚N, 120˚W-180˚W)……..95

Figure A.3.8. El Niño standard deviation (km) of RMG (unitless) for DJF 2010 over 5˚x5˚analysis region (5˚N-45˚N, 120˚W-180˚W)……95

Figure A 3.9. Median inversion base height standard deviation (km) for La Niña (DJF 2011) over 5˚x5˚analysis region (5˚N-45˚N, 120˚W-180˚W)……..96

Figure A.3.10. La Niña standard deviation (km) of RMG (unitless) for DJF 2011 over 5˚x5˚analysis region (5˚N-45˚N, 120˚W-180˚W)……96

Figure A.5.1. Histogram of observed median inversion base height z_i (km) for 2.5˚x2.5˚ grid box centered on 17.5˚N, 165˚W during DJF 2007-2012……102

Figure A.5.2. Quantile-quantile plot (q-q plot) of observed median inversion base height z_i (km) for 2.5˚x2.5˚ grid box centered on 17.5˚N, 165˚W during DJF 2007-2012. X-axis represents standard normal quantiles; Y-axis represents quantiles of input samples. Each observation is represented by a blue cross. The red line represents the 1-to-1 relationship between a standard normal data distribution and the sampled data set. If blue crosses are oriented along the red diagonal line, the population distribution is considered to be “normal”……102

Figure A.5.3. Histogram of observed median inversion base height z_i (km) for 2.5˚x2.5˚ grid box centered on 17.5˚N, 165˚W during DJF-TW 2007-2012……103

Figure A.5.4. Quantile-quantile plot (q-q plot) of observed median inversion base height z_i (km) for 2.5˚x2.5˚ grid box centered on 17.5˚N, 165˚W during DJF-TW 2007-2012. X-axis represents standard normal quantiles; Y-axis represents quantiles of input samples. Each observation is represented by a blue cross. The red line represents the 1-to-1 relationship between a standard normal data distribution and the sampled data set. If blue crosses are oriented along the red diagonal line, the population distribution is considered to be “normal” ……103

Figure A.5.5. Histogram of observed median inversion base height z_i (km) for 2.5˚x2.5˚ grid box centered on 17.5˚N, 165˚W during JJA 2007-2012……104

Figure A.5.6. Quantile-quantile plot (q-q plot) of observed median inversion base height z_i (km) for 2.5˚x2.5˚ grid box centered on 17.5˚N, 165˚W during JJA 2007-2012. X-axis represents standard normal quantiles; Y-axis represents quantiles of input samples. Each observation is represented by a blue cross. The red line represents the 1-to-1 relationship between a standard normal data distribution and the sampled data set. If blue crosses are oriented along the red diagonal line, the population distribution is considered to be "normal" ……104

Figure A.5.7. Histogram of observed median inversion base height z_i (km) for 2.5˚x2.5˚ grid box centered on 17.5˚N, 165˚W during JJA-TW 2007-2012……105

Figure A.5.8. Quantile-quantile plot (q-q plot) of observed median inversion base height z_i (km) for 2.5˚x2.5˚ grid box centered on 17.5˚N, 165˚W during JJA-TW 2007-2012. X-axis represents standard normal quantiles; Y-axis represents quantiles of input samples. Each observation is represented by a blue cross. The red line represents the 1-to-1 relationship between a standard normal data distribution and the sampled data set. If blue crosses are oriented along the red diagonal line, the population distribution is considered to be "normal"……105

Figure A.5.9. Histogram of observed median inversion base height z_i (km) for 2.5˚x2.5˚ grid box centered on 20˚N, 157.5˚W during DJF 2007-2012……106

Figure A.5.10. Quantile-quantile plot (q-q plot) of observed median inversion base height z_i (km) for 2.5˚x2.5˚ grid box centered on 20˚N, 157.5˚W during DJF 2007-2012. X-axis represents standard normal quantiles; Y-axis represents quantiles of input samples. Each observation is represented by a blue cross. The red line represents the 1-to-1 relationship between a standard normal data distribution and the sampled data set. If blue crosses are oriented along the red diagonal line, the population distribution is considered to be "normal"……106

Figure A.5.11. Histogram of observed median inversion base height z_i (km) for 2.5˚x2.5˚ grid box centered on 20˚N, 157.5˚W during DJF-TW 2007-2012 ……107

Figure A.5.12. Quantile-quantile plot (q-q plot) of observed median inversion base height z_i (km) for 2.5˚x2.5˚ grid box centered on 20˚N, 157.5˚W during DJF-TW 2007-2012. X-axis represents standard normal quantiles; Y-axis represents quantiles of input samples. Each observation is represented by a blue cross. The red line represents the 1-to-1 relationship between a standard normal data distribution and the sampled data set. If blue crosses are oriented along the red diagonal line, the population distribution is considered to be "normal"……107

Figure A.5.13. Histogram of observed median inversion base height z_i (km) for 2.5˚x2.5˚ grid box centered on 20˚N, 157.5˚W during JJA 2007-2012……108

Figure A.5.14. Quantile-quantile plot (q-q plot) of observed median inversion base height z_i (km) for 2.5˚x2.5˚ grid box centered on 20˚N, 157.5˚W during JJA 2007-2012. X-axis represents standard normal quantiles; Y-axis represents quantiles of input samples. Each observation is represented by a blue cross. The red line represents the 1-to-1 relationship between a standard normal data distribution and the sampled data set. If blue crosses are oriented along the red diagonal line, the population distribution is considered to be "normal"……108

Figure A.5.15. Histogram of observed median inversion base height z_i (km) for 2.5˚x2.5˚ grid box centered on 20˚N, 157.5˚W during JJA-TW 2007-2012……109

Figure A.5.16. Quantile-quantile plot (q-q plot) of observed median inversion base height z_i (km) for 2.5˚x2.5˚ grid box centered on 20˚N, 157.5˚W during JJA-TW 2007-2012. X-axis represents standard normal quantiles; Y-axis represents quantiles of input samples. Each observation is represented by a blue cross. The red line represents the 1-to-1 relationship between a standard normal data distribution and the sampled data set. If blue crosses are oriented along the red diagonal line, the population distribution is considered to be "normal"……109

Figure A.5.17. Histogram of observed median inversion base height z_i (km) for 2.5˚x2.5˚ grid box centered on 22.5˚N, 162.5˚W during DJF 2007-2012…….110

Figure A.5.18. Quantile-quantile plot (q-q plot) of observed median inversion base height z_i (km) for 2.5˚x2.5˚ grid box centered on 22.5˚N, 162.5˚W during DJF 2007-2012. X-axis represents standard normal quantiles; Y-axis represents quantiles of input samples. Each observation is represented by a blue cross. The red line represents the 1-to-1 relationship between a standard normal data distribution and the sampled data set. If blue crosses are oriented along the red diagonal line, the population distribution is considered to be "normal"……110

Figure A.5.19. Histogram of observed median inversion base height z_i (km) for 2.5˚x2.5˚ grid box centered on 22.5˚N, 162.5˚W during DJF-TW 2007-2012……..111

Figure A.5.20. Quantile-quantile plot (q-q plot) of observed median inversion base height z_i (km) for 2.5˚x2.5˚ grid box centered on 22.5˚N, 162.5˚W during DJF-TW 2007-2012. X-axis represents standard normal quantiles; Y-axis represents quantiles of input samples. Each observation is represented by a blue cross. The red line represents the 1-to-1 relationship between a standard normal data distribution and the sampled data set. If blue crosses are oriented along the red diagonal line, the population distribution is considered to be "normal"……111

Figure A.5.21. Histogram of observed median inversion base height z_i (km) for 2.5˚x2.5˚ grid box centered on 22.5˚N, 162.5˚W during JJA 2007-2012……..112

Figure A.5.22. Quantile-quantile plot (q-q plot) of observed median inversion base height z_i (km) for 2.5˚x2.5˚ grid box centered on 22.5˚N, 162.5˚W during JJA 2007-2012. X-axis represents standard normal quantiles; Y-axis represents quantiles of input samples. Each observation is represented by a blue cross. The red line represents the 1-to-1 relationship between a standard normal data distribution and the sampled data set. If blue crosses are oriented along the red diagonal line, the population distribution is considered to be "normal"……...112

Figure A.5.23. Histogram of observed median inversion base height z_i (km) for 2.5˚x2.5˚ grid box centered on 22.5˚N, 162.5˚W during JJA-TW 2007-2012……..113

Figure A.5.24. Quantile-quantile plot (q-q plot) of observed median inversion base height z_i (km) for 2.5˚x2.5˚ grid box centered on 22.5˚N, 162.5˚W during JJA-TW 2007-2012. X-axis represents standard normal quantiles; Y-axis represents quantiles of input samples. Each observation is represented by a blue cross. The red line represents the 1-to-1 relationship between a standard normal data distribution and the sampled data set. If blue crosses are oriented along the red diagonal line, the population distribution is considered to be "normal"……113

Chapter 1. Introduction

1.1 Overview

The base height of the trade wind inversion (z_i) over the central North Pacific Ocean increases from northeast to southwest with an approximate average height of 2000 meters (m) over the Hawaiian Islands (Neiburger et al. 1961; Grindinger 1992; Schroeder 1993; Bingaman 2005; Cao 2007). However, analysis of the spatial variation of the inversion has been limited by data availability until the last decade. The utilization of Global Positioning System (GPS) radio occultation (RO) techniques to measure the transition between the marine boundary layer (BL) and free atmosphere allows for vertical atmospheric profiles to be examined at a much higher spatial resolution than ever before. As a result, this remote sensing technique will allow for inversion base estimations to be made over regions historically void of vertical atmospheric profile observations.

The northeasterly surface flow over the central North Pacific Ocean is a manifestation of the North Pacific sub-Tropical High (NPSTH). The resulting low level flow, referred to as the trade winds (TW), represents the world's most consistent surface wind field (Malkus 1956). Along its trajectory, the subsiding air from upper levels comes into contact with warm, moist rising air from the surface. The inversion layer represents the transition between the lowest part of the atmosphere which is directly affected by the Earth's surface and the free atmosphere (Riehl, 1979). The transition between is marked by a temperature increase accompanied by a dramatic decrease in water vapor. Visually, the cloud tops reveal the top of the BL which coincides with the base of the inversion. As a result, the presence of the inversion has important impacts on many processes within the BL such as stability, cloud cover, and precipitation (Neiburger et al. 1961; Riehl 1979; Albrecht 1984; Betts and Ridgeway 1988, 1989; Grindinger 1992; Schroeder 1993; Trenberth and Stepaniak 2003; Bingaman 2005).

1.2 Horizontal Distribution of Inversion Height

The inversion over the sub-Tropical Atlantic was first studied in 1936 when von Ficker (1936) mapped the horizontal distribution of the trade wind inversion using radiosonde data from the *Meteor*. Observation of the inversion over the subtropical Atlantic revealed a minimum base height over the western coast of Africa with increasing heights the south and west toward the intertropical convergence zone (ITCZ).

The inversion over the Pacific Ocean displays similar characteristics to those observed over the Atlantic (Riehl 1954; Malkus 1958; Malkus and Riehl 1964). A vertical cross section (Figure 1 – Malkus 1958) illustrates the height increase of the inversion from northeast to southwest. The BL, referred to as the moist layer in Figure 1, consists of the subcloud layer (surface to cloud base) and the cloud layer. Evaporation and turbulent eddies add moisture to the subcloud layer. The increase in moisture coupled with radiative surface heating causes the air to rise and condense at an approximate height of 650 m (2000 feet) marking the beginning of the cloud layer (straight-dashed line in Figure 1). Active cumuli grow vertically until they reach the inversion base (sloped-dashed line in Figure 1) which is the boundary between the convection within the BL and the stable sinking air of the free atmosphere. The increase in height of the inversion to the southwest is attributed to cumulus driven energy exchange between the BL and free atmosphere (Riehl and Malkus 1951; Malkus 1958; Riehl and Simpson 1979). Since that time, analyses of the height of the inversion base as well as the seasonal variation of the height have been conducted primarily using radiosonde observations (Neiburger 1961; Tran 1995; Bingaman 2005).

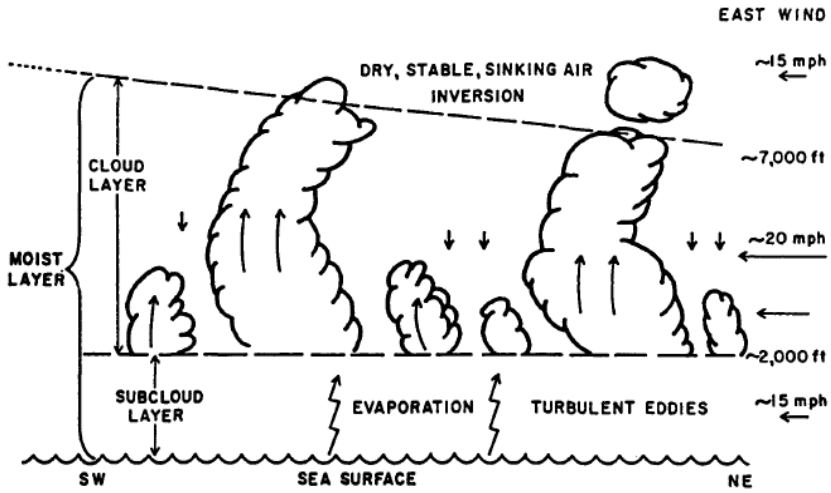

Figure 1.1. Vertical cross section of the BL over the Pacific Ocean consisting of the subcloud layer, cloud layer, and inversion. The inversion layer marks the boundary between the BL and free atmosphere. (Malkus 1958).

Grindinger (1992) used data from the Hawaiian Rainband Project (HaRP) to compare radiosonde measured inversion heights to those measured by a vertical wind profiler over the Big Island of Hawaii. The frequency (12 minute) of the profiler observations revealed details of the temporal variations of the inversion base on an intra-day, daily, and multi-day cycle (Grindinger 1992). The short period variations detected by the wind profiler go unnoticed by radiosondes due to their 12 hour sampling frequency (Grindinger 1992). However, for the majority of points between 1800 m and 3000 m, the difference between the profiler and radiosonde observations were less than 150 m (Grindinger 1992).

1.3 Refractivity Measured Inversion Base Height

Recently, estimations of the inversion base height have been conducted using GPS RO which uses the bending of radio wave signals between GPS and low earth orbiting (LEO) satellites to produce a vertical refractivity profile (Figure 1.2). Atmospheric moisture accounts for approximately 75% of the measured refractivity value (Bean and Dutton 1966). Due to the strong relationship between refractivity and water vapor, the presence of a sharp vertical moisture gradient which signifies the top of the boundary layer (inversion base) can be detected using refractivity at a vertical resolution of 100 m (Anthes et al. 2007).

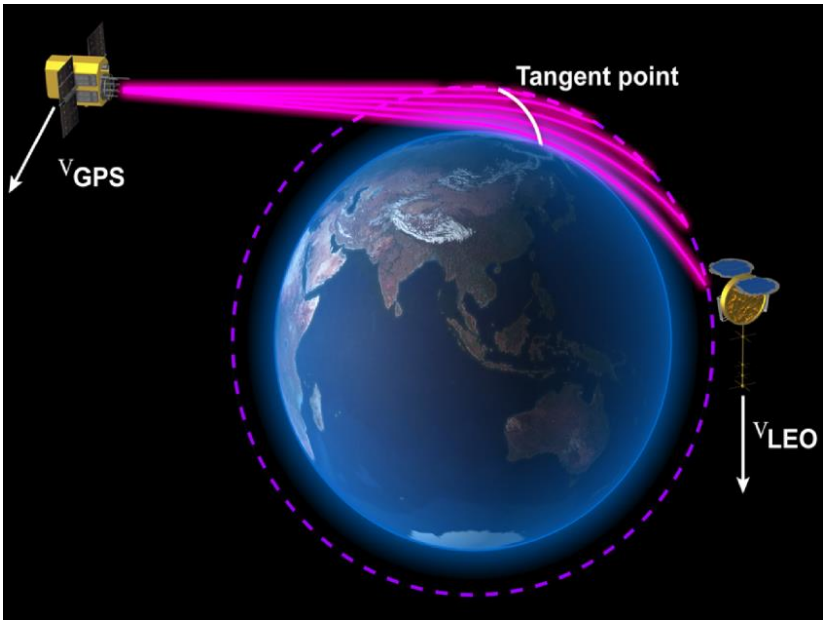

Figure 1.2. Illustration of the progression of a radio occultation. The tangent point is the point which the radio wave between a GPS and LEO satellite comes in to contact with Earth's atmosphere (purple dashed line) as it passes between the two satellites. The COMET® Program - The University Corporation for Atmospheric Research, 2014.

Using the refractivity method, Guo et al. (2011) described the transition between the BL and the free atmosphere as the area where the balance between turbulent processes and mean vertical motions associated with large scale circulations exists. Estimation of the depth of the BL utilizes the "breakpoint" in the vertical profile where refractivity values, similar to water vapor values, begin to decrease significantly with height. Boundary layer depths using the GPS RO technique were then compared with heights measured by high-resolution radiosonde data as well as modeled heights from the European Center for Medium Range Weather Forecasting (ECMWF) global analysis fields (Guo et al. 2011). This comparison is possible by using the equation which defines the thermodynamic properties of the atmosphere in terms of refractivity (N in N-units) which can be calculated using atmospheric pressure (P in hPa), temperature (T in K), and water vapor partial pressure (P_w in hPa). The microwave refractivity equation (Eq. 1.1) defined by Smith and Weintraub (1953) illustrates the dependence of N on the three components with the moisture term accounting for ~75% of the refractivity value while the temperature accounts for ~15% (Bean and Dutton 1966).

$$N = 77.6\frac{P}{T} + 3.73\ x\ 10^5\ \frac{P_w}{T^2} \qquad \text{(Eq. 1.1)}$$

In terms of N, the BL top is defined as the height of the minimum refractivity value within the lowest 6 km of the troposphere (Guo et al. 2011). The analysis resulted in global estimates of the temporal and spatial variability of the BL top with the authors concluding no discernible difference existed between GPS RO profiles and those calculated from radiosonde data. Comparison of refractivity values calculated from ECMWF data showed estimations of z_i were slightly lower (~200 m) with locations of minima/maxima varying by season.

Ao et al. (2012) studied the height of the BL using GPS RO differential refractivity and humidity profiles. The base of the inversion is identified by the minimum refractivity gradient ($\frac{dN}{dz}$) within 3.5 km of the surface. Results were compared to calculated refractivity values from the ECMWF reanalysis over two years (2007-2009). The comparison between calculated and measured refractivity gradients found similar spatial and temporal variations with model calculated inversion heights lower than GPS RO estimated heights by approximately 200 m (Ao et al. 2012). The refractivity gradient is calculated by differentiating the microwave refractivity equation (Eq. 1.1 - Smith and Weintraub 1953) with respect to height (Eq. 1.2 – Ao et al. 2012).

$$\frac{dN}{dz} = a_1\left(\frac{1}{T}\right)P' + \left[a_1\left(\frac{P}{T^2}\right) + 2a_2\left(\frac{P_w}{T^3}\right)\right]T' + a_2\left(\frac{P_w'}{T^2}\right)$$

$$a_1 = 77.6\frac{K}{hPa} \qquad a_2 = 3.73x10^5\frac{K^2}{hPa} \qquad \text{(Eq. 1.2)}$$

The components of $\frac{dN}{dz}$ (N-units km^{-1}) are such that in the absence of a sharp moisture gradient, the pressure term $a_1\left(\frac{1}{T}\right)P'$ will dominate the refractivity profile and the minimum value of $\frac{dN}{dz}$ will be located at the lowest profile height (Ao et al. 2012). For the temperature term $\left[a_1\left(\frac{P}{T^2}\right) + 2a_2\left(\frac{P_w}{T^3}\right)\right]T'$ to exceed pressure; the vertical temperature gradient must be greater than 40 K km^{-1} (Ao et al. 2012). The water vapor pressure term $a_2\left(\frac{P_w'}{T^2}\right)$ must have a gradient less than -7 hPa km^{-1} to exceed the pressure gradient term (Ao et al. 2012).

In an effort to compare the available measurements of the BL over the open ocean to the observations from GPS RO, Xie et al. (2012) conducted a study to quantify the similarities and differences between two BL parameters: (1) the height of the BL top and (2) refractivity gradient near the BL top. The comparative analysis includes high-resolution ECMWF data, radiosonde observations from the VAMOS (Variability of the American Monsoon Systems) Ocean-Cloud-Atmosphere-Land Study Regional Experiment (VOCALS-REx) field campaign (Wood et al. 2011), and GPS RO data obtained from the COSMIC Constellation. The purpose was to analyze the quality of the GPS RO data by comparing BL height measurements with other available methods. Despite the difficulties exposed by super-refractivity (a result of the presence of moisture in the BL) and the corresponding N-bias beneath the BL (Sokolovskiy 2003; Xie et al. 2006), the ability of GPS RO to detect BL height is not affected (Xie et al. 2012).

1.4 Motivation

Prior to the availability of GPS RO techniques, the most detailed analysis over the Hawaiian region was by Bingaman (2005) who studied the characteristics of the inversion layer using radiosonde data over five years (1999-2004) from Lihu'e and Hilo. The focus of the study was dedicated to identifying the characteristics and median statistics of the inversion. Analysis periods included annual and diurnal variations under normal conditions as well as those which occur under El Niño-Southern Oscillation (ENSO) conditions. Additional points of the study included the spatial variation between the two sites such as the higher inversion heights over Hilo when compared to Lihu'e. Over the five years 1999-2004, approximately 8000 radiosonde profiles between two sites were available for an analysis of inversion layer characteristics. Using the available data collected by GPS RO, approximately 30,000 vertical refractivity profiles exist over the central North Pacific Ocean between 5˚N-45˚N and 120˚W-180˚W (Figure 1.3). Using these data, a similar analysis can be performed in order to add to the observations of the spatial and temporal distribution of the inversion layer over the Hawaiian region.

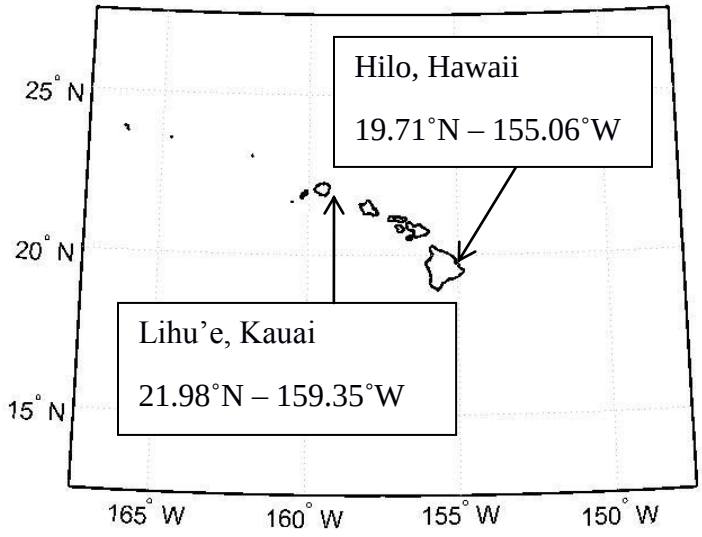

Figure 1.3. Analysis region (5˚N-45˚N, 120˚W-180˚W) and approximate locations of Hilo and Lihue sounding stations.

1.5 Objectives

First, do COSMIC RO data accurately depict the presence and height characteristics of the inversion base over the central North Pacific Ocean? Second, do the analyses performed provide additional detail to what is already known and accepted? Third, can data be utilized at a high enough grid resolution in order to examine the various interactions between BL circulations and the Hawaiian Islands?

Using only data from the COSMIC constellation, I will analyze the spatial variation of the inversion base over the central North Pacific Ocean, centered on the Hawaiian region. The goal is to utilize the information retrieved by the constellation from its inception in 2006 through the end of 2012 in order to gain a detailed representation of the horizontal distribution of the inversion base. This will be achieved by separating and analyzing retrieved data in multiple ways. First, an annual climatology for the years 2007 – 2012 will be performed. Data will be divided according to season (DJF, JJA) and the inversion base height will be identified using the refractivity gradient method (Ao et al. 2012; Xie et al 2012). Additionally, relative strength of the inversion will be determined by the relative minimum gradient (RMG) method which is described in Chapter 3. Similar

comparisons will be carried out for ENSO warm and cold events as well as diurnal variations during the summer (JJA) season. Comparisons to earlier studies by Bingaman (2005) will be made in an attempt to validate the accuracy of the GPS RO method. The remainder of this thesis will be focused on the detection of wake effects caused by the interaction between surface flow and the island chain.

Chapter 2. Climatology

The islands typically experience a warm season and cool season. During the warm season, May through September, there is little variation in the overall weather pattern. More specifically, the months of June, July, and August (JJA) experience northeasterly surface flow approximately 90% of the time (Schroeder 1993; Kodama and Businger 1998). The cool season, October through April, is not as uniform as its summer counterpart (Schroeder and Giambelluca 1993; Kodama and Businger 1998). The interaction between the islands and the prevailing weather patterns over the Pacific region add layers of complexity during the core winter months of December, January, and February (DJF). Based on previous works, the annual migration of the NPSTH and polar jet stream leaves the islands vulnerable to Kona low pressure systems, upper level troughs, and cold fronts (Schroeder 1993; Kodama and Businger 1998). As a result, surface trade wind flow is present less than 50% of the time during DJF (Schroeder 1993).

2.1 Sea Level Pressure

The maximum surface pressure associated with the NPSTH during JJA is approximately 1024 hPa and located near 37˚N, 150˚W (Figure 2.1). The location of the NPSTH center during September, October, and November (SON) is near 35˚N, 142.5˚W, and southeast of the JJA location while strength decreases to 1020 hPa (Figure 2.2). During the DJF season, the center of the NPSTH (1022 hPa) is located in the vicinity of 30˚N, 135˚W, south and east of the JJA and SON locations (Figure 2.3). Through the months of March, April and May (MAM) the center of the high (1024 hPa) is located around 35˚N, 140˚W, and moves northwestward as JJA approaches (Figure 2.4).

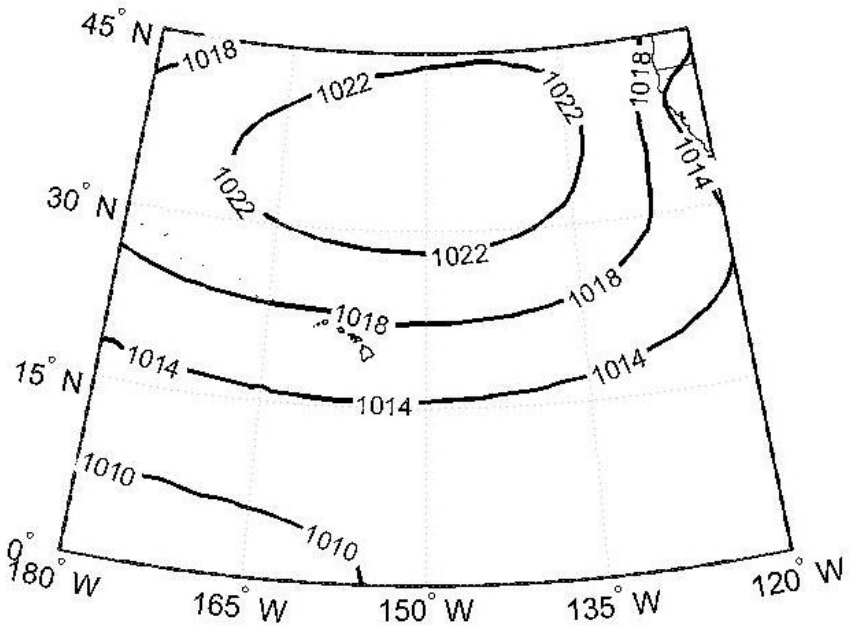

Figure 2.1. NCEP-FNL sea level pressure (hPa) climatology for JJA 2007-2012.

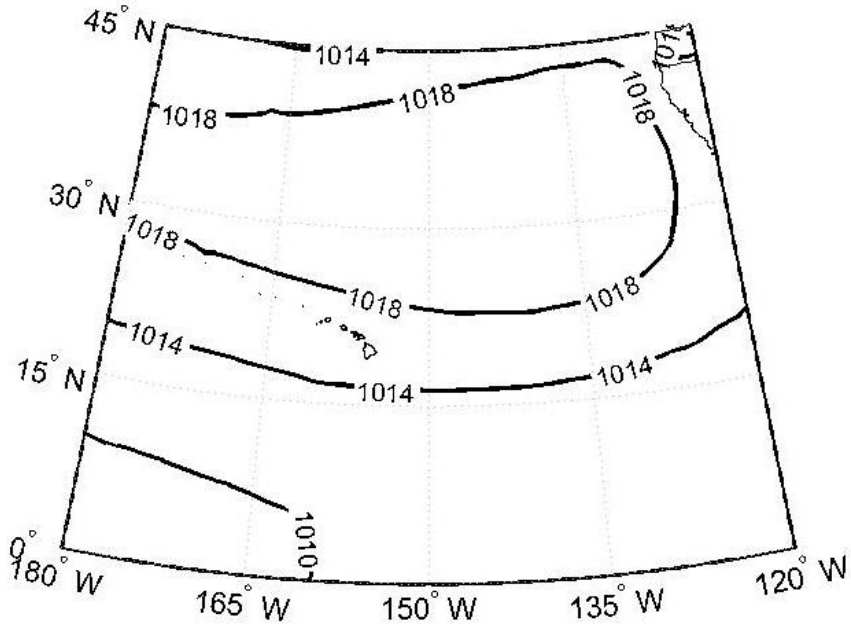

Figure 2.2. NCEP-FNL sea level pressure (hPa) climatology for SON 2007-2012.

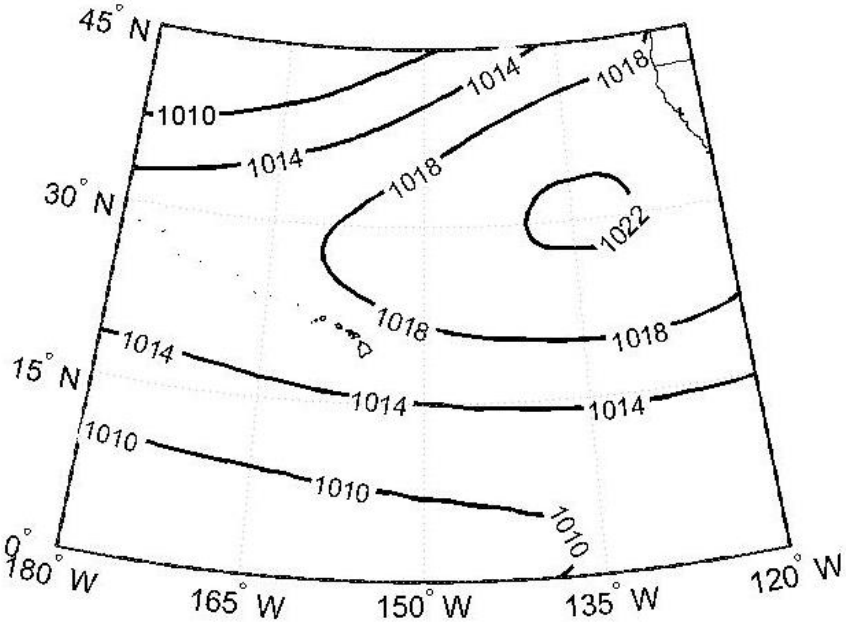

Figure 2.3. NCEP-FNL sea level pressure (hPa) climatology for DJF 2007-2012.

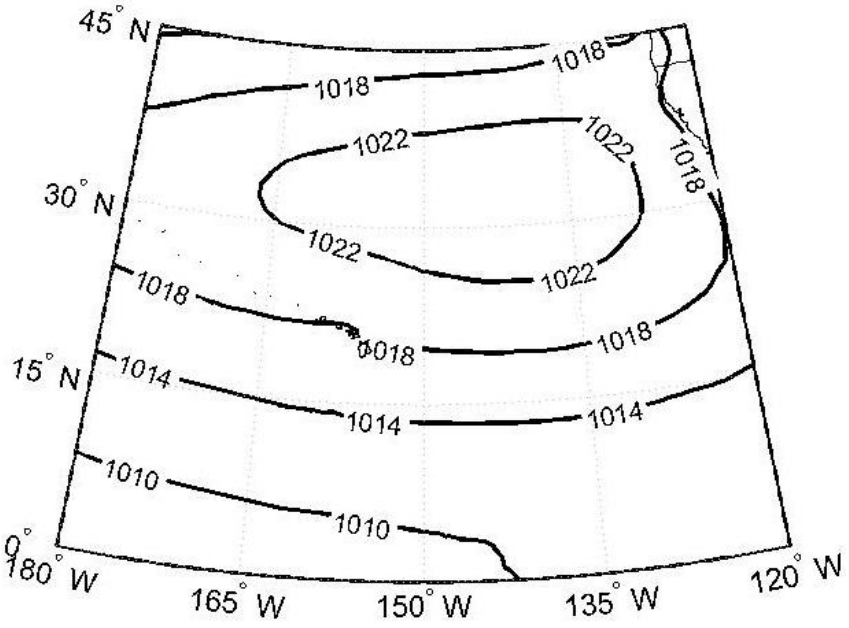

Figure 2.4. NCEP-FNL sea level pressure (hPa) climatology for MAM 2007-2012.

2.2 Surface Wind

Prevailing surface winds over the central North Pacific region are governed by the strength and location of the NPSTH; accordingly their origins and the effects of island interactions vary by season. Climatologically, the surface winds are predominantly from the northeast during JJA with a maximum mean velocity of approximately 8 m s^{-1} located to the south of the Big Island bisected by the 15˚N latitude line between 150˚W and 165˚W (Figure 2.5). Mean minimum surface wind vectors are seen in the lee of the islands that range from less than 2 m s^{-1} directly west of the Big Island and increasing to between 4-6 m s^{-1} south and west of Kauai.

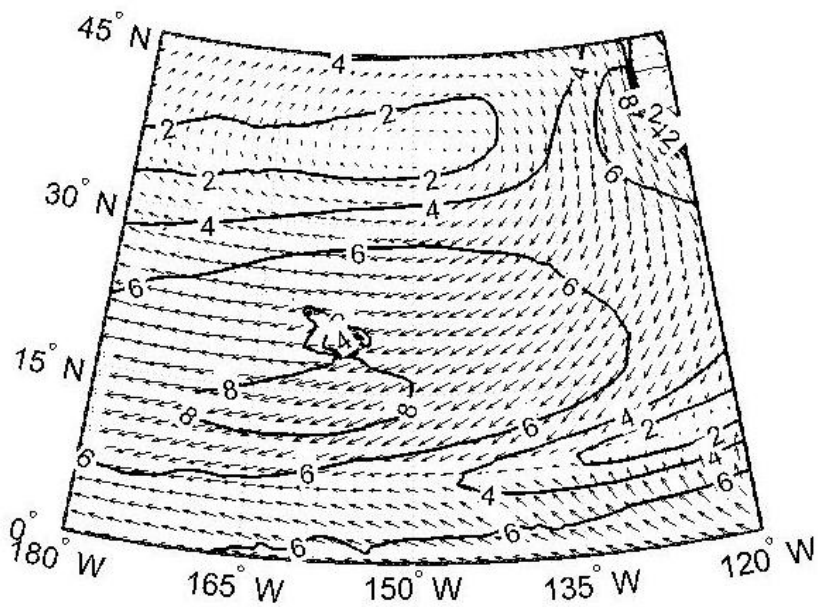

Figure 2.5. Mean surface wind vectors (m s^{-1}) and isotachs (2 m s^{-1}) for JJA 2007-2012 from NCEP-FNL.

As the NPSTH shifts southeastward, the surface flow has an increasing easterly component. As a result, the maximum mean wind speed during DJF of 8 m s^{-1}, south of the Big Island has increased in areal coverage south of 20˚N stretching across the entire analysis domain. Additionally, the area just south of 30˚N shows a mean surface minimum wind between 2 - 4 m s^{-1} (Figure 2.6). During the transition seasons of SON and MAM (not shown) surface winds resemble the DJF season which features the highest

mean zonal velocities over an elongated area of 8 m s^{-1} south and west of the Big Island and minimum mean (2 - 4 m s^{-1}) in the lee of the Big Island.

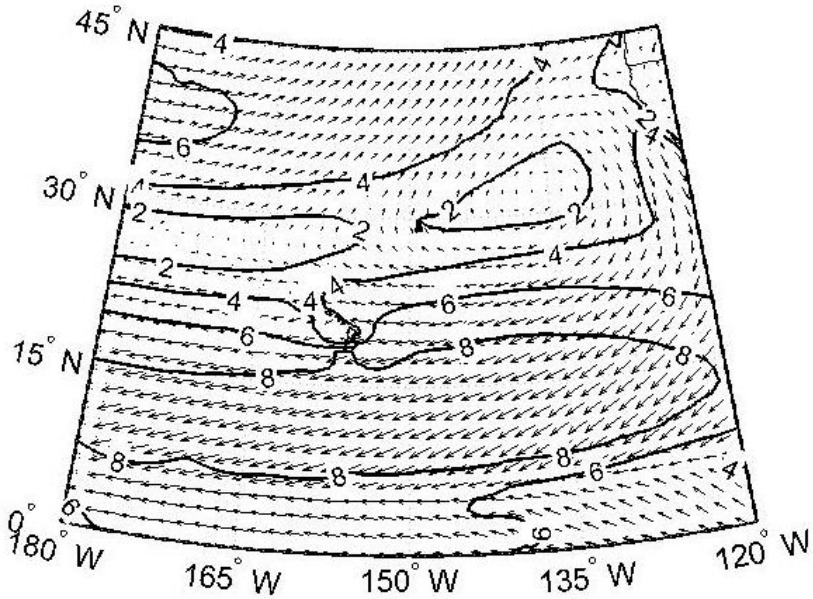

Figure 2.6. Mean surface wind vectors (m s^{-1}) and isotachs (2 m s^{-1}) for DJF 2007-2012 from NCEP-FNL.

2.3 250 hPa Wind

The location of the polar and sub-Tropical jet streams can influence rising and sinking motion through a large depth of the atmosphere. During JJA, the polar jet is north of 40˚N while the sub-Tropical jet is situated approximately west of 20˚N, 165˚W with a mean wind speed maximum of 10 m s^{-1} (Figure 2.7). As the season changes, both jets migrate south and the polar jet can be seen approaching the region from the north during SON (Figure 2.8). During DJF the polar jet is located at its southernmost position, north of 30˚N and west of 180˚W with a mean magnitude in excess of 50 m s^{-1} (Figure 2.9). During DJF, the location of the Hawaiian Islands is southeast of the right exit region. The event of a south or westward push of the polar jet could mean enhanced upper level subsidence over the islands. If the resultant descending motion is strong enough through a deep layer, it could affect the height of the inversion layer. Moving from DJF into MAM, the polar and sub-tropical jets both move back to the north, leaving the islands under the influence of the left entrance region of the sub-Tropical jet (Figure 2.10). This is also an area of enhanced upper level subsidence.

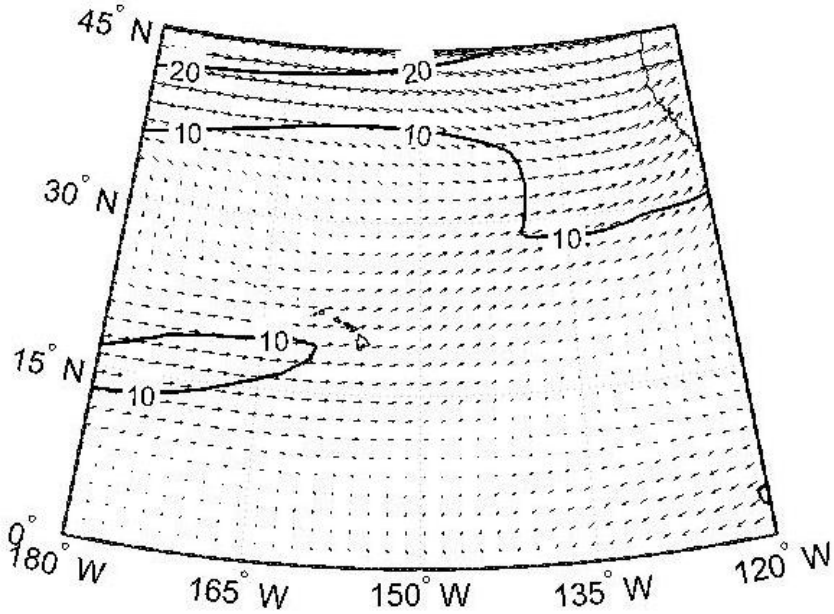

Figure 2.7. Mean 250 hPa wind vectors (m s^{-1}) and isotachs (10 m s^{-1}) for JJA 2007-2012 from NCEP-FNL.

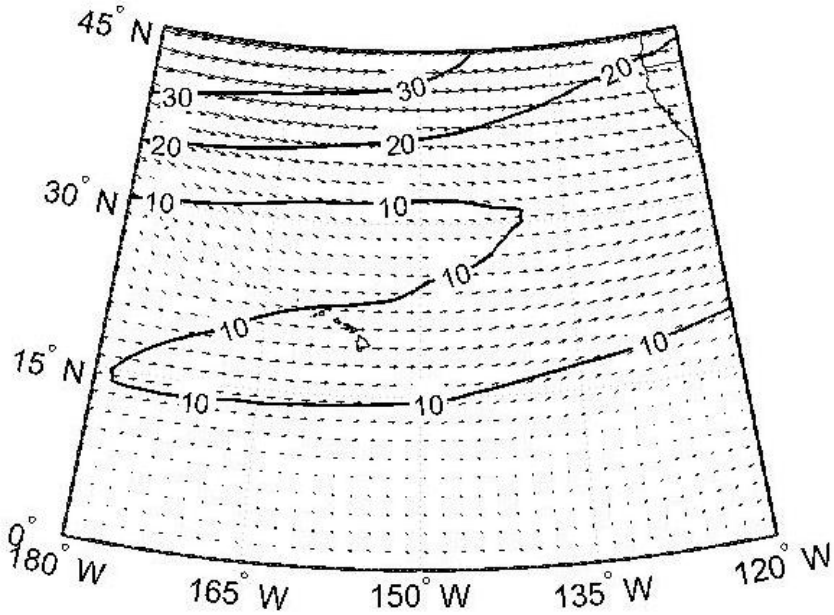

Figure 2.8. Mean 250 hPa wind vectors (m s^{-1}) and isotachs (10 m s^{-1}) for SON 2007-2012 from NCEP-FNL.

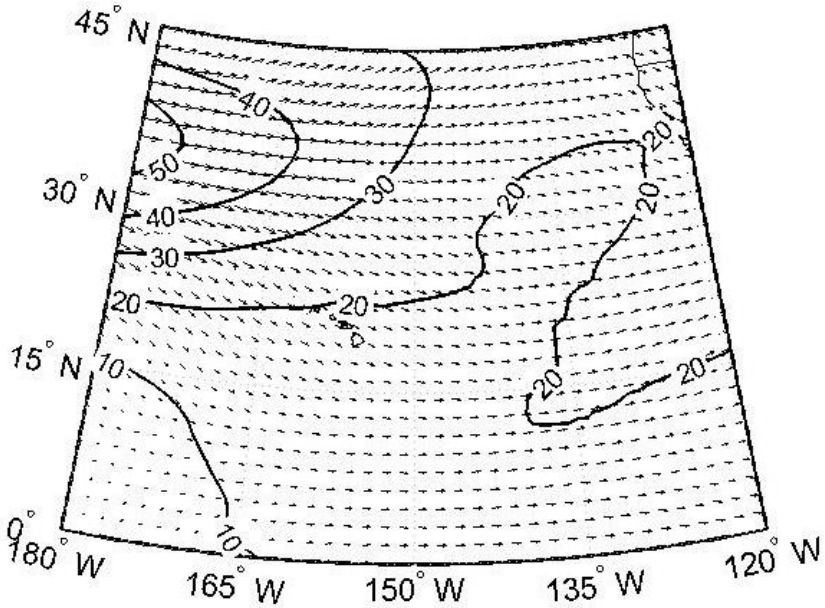

Figure 2.9. Mean 250 hPa wind vectors (m s^{-1}) and isotachs (10 m s^{-1}) for DJF 2007-2012 from NCEP-FNL.

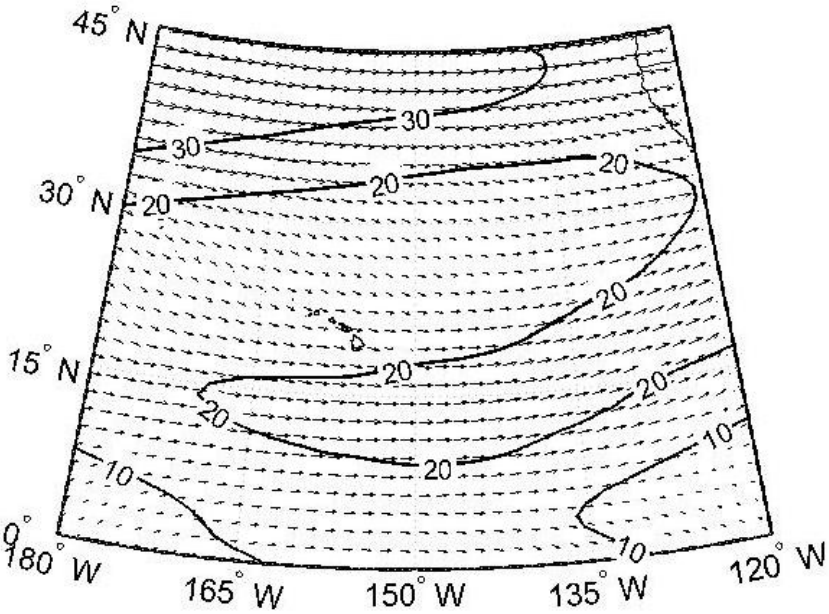

Figure 2.10. Mean 250 hPa wind vectors (m s^{-1}) and isotachs (10 m s^{-1}) for MAM 2007-2012 from NCEP-FNL.

2.4 Vertical Velocity

Vertical velocity at 500 hPa (ω_{500}) is used as an indicator for the large scale vertical motion. Over the analysis region, maximum values of ω_{500} occur adjacent to the California coast and decrease to the west and south. Over the Hawaiian region, mean negative values (subsidence) of ω_{500} are weaker during JJA (-0.01 to -0.05 Pa s^{-1}) and greater during DJF (-0.05 to -0.08 Pa s^{-1}) which can be seen in Figures 2.11 and 2.12 respectively.

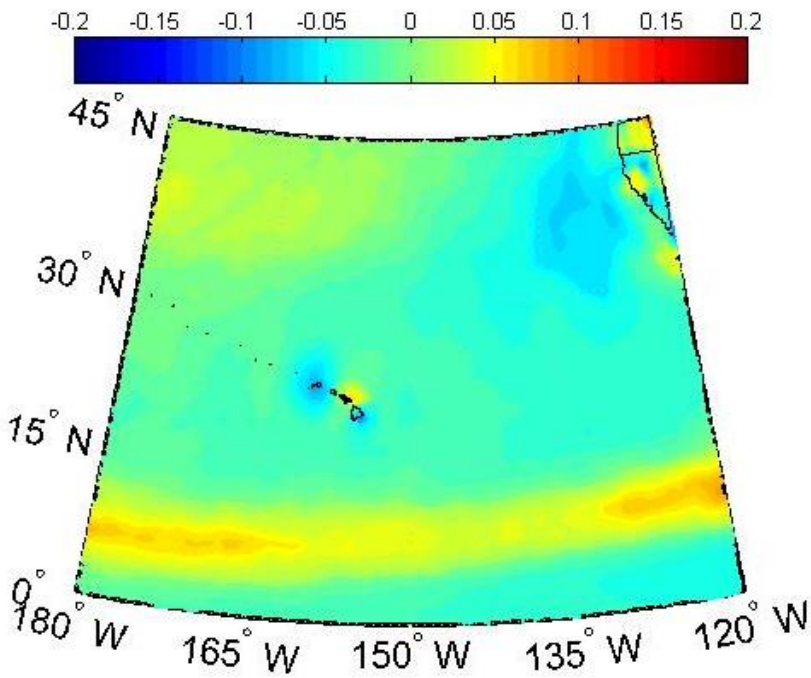

Figure 2.11. NCEP-FNL ω_{500} vertical velocities in Pa s^{-1} climatology for JJA 2007-2012. Positive values indicate rising motion and negative values indicate sinking motion.

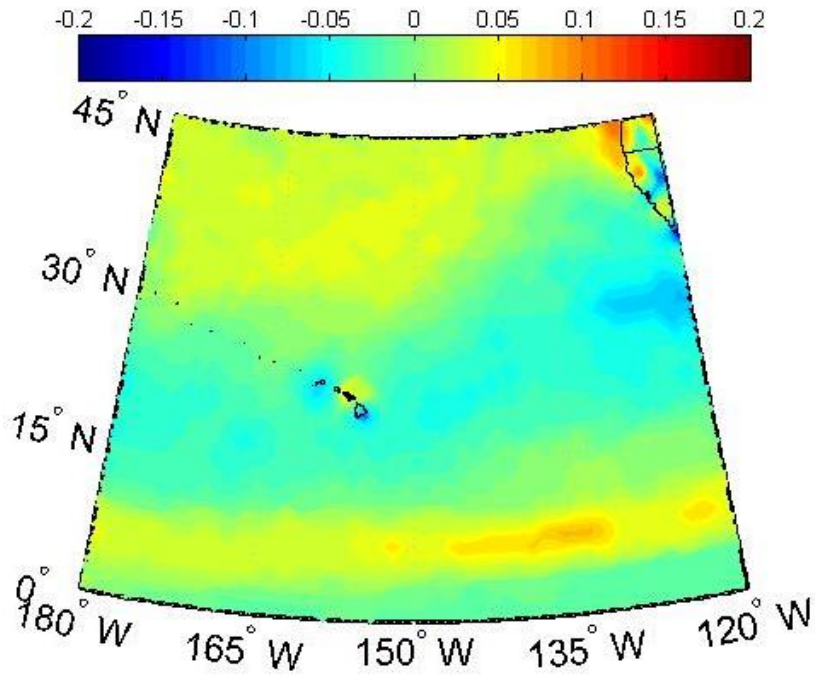

Figure 2.12. Same as Figure 2.11 for DJF 2007-2012.

2.5 ENSO Influence

2.5.1 El Niño

El Niño events typically bring about a lower inversion height as a result of stronger upper level subsidence over the Hawaiian region (Chu 1995). The maximum pressure area of the NPSTH (Figure 2.13) is weaker during warm event winters (1018 hPa) than during the overall climatology years; however, it is situated closer to the islands. Surface wind vectors show a mean maximum value of 8 m s^{-1} along and south of 15˚N and north of 30˚N while a minimum mean surface wind speed of 2 m s^{-1} exists over the entire island chain (Figure 2.14). Weaker surface winds lead to a decrease in surface interaction, and less rising motion. As a result, the upper level subsidence, which is present over a larger area (Figure 2.15), becomes dominant without the rising motion from the boundary layer. The polar jet stream maintains a similar longitudinal position as DJF climatology (~35˚N), however, the polar jet axis has moved eastward and increased in magnitude to

60 m s^{-1} (Figure 2.16). As a result, Hawaii is situated underneath the right exit region which can result in stronger, large scale sinking motion over the islands.

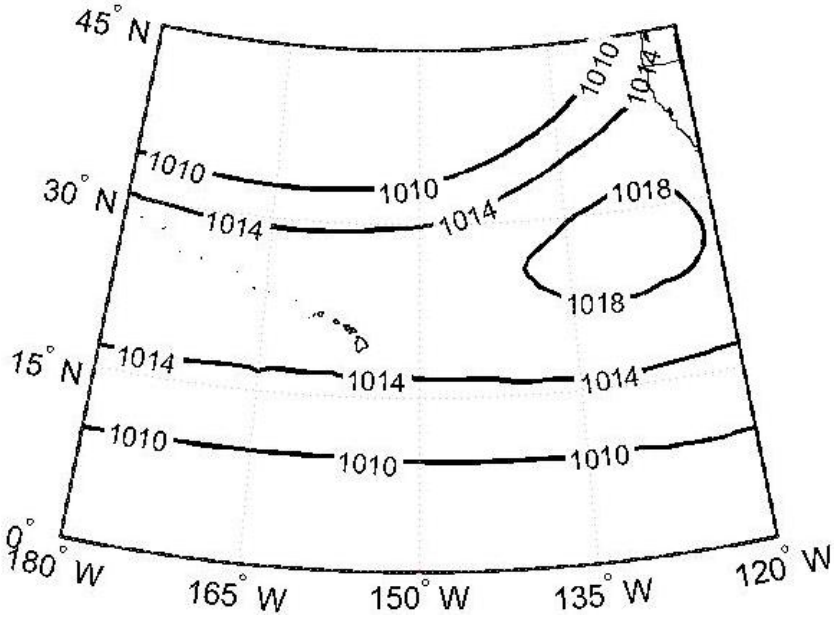

Figure 2.13. NCEP-FNL sea level pressure (hPa) climatology for DJF 2010 El Niño from NCEP-FNL.

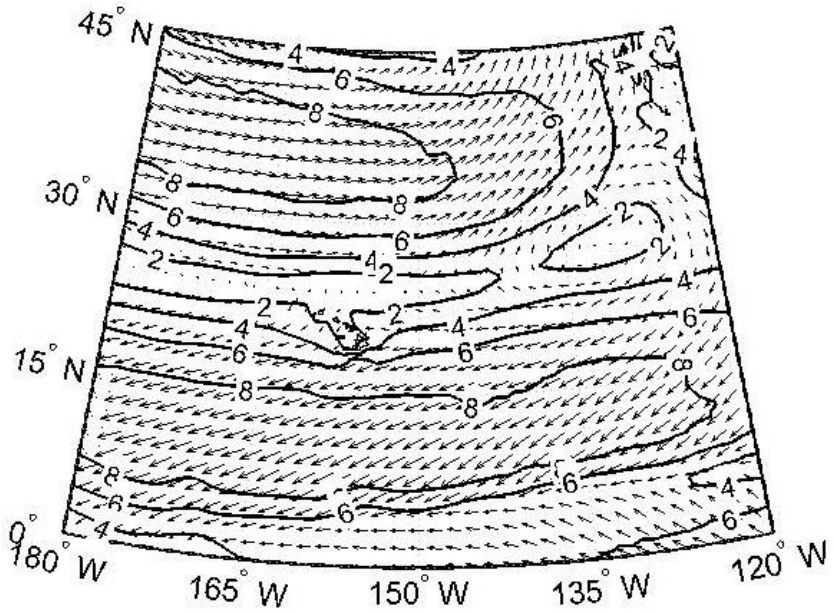

Figure 2.14. Mean surface wind vectors (m s^{-1}) and isotachs (2 m s^{-1}) for DJF 2010 El Niño from NCEP-FNL.

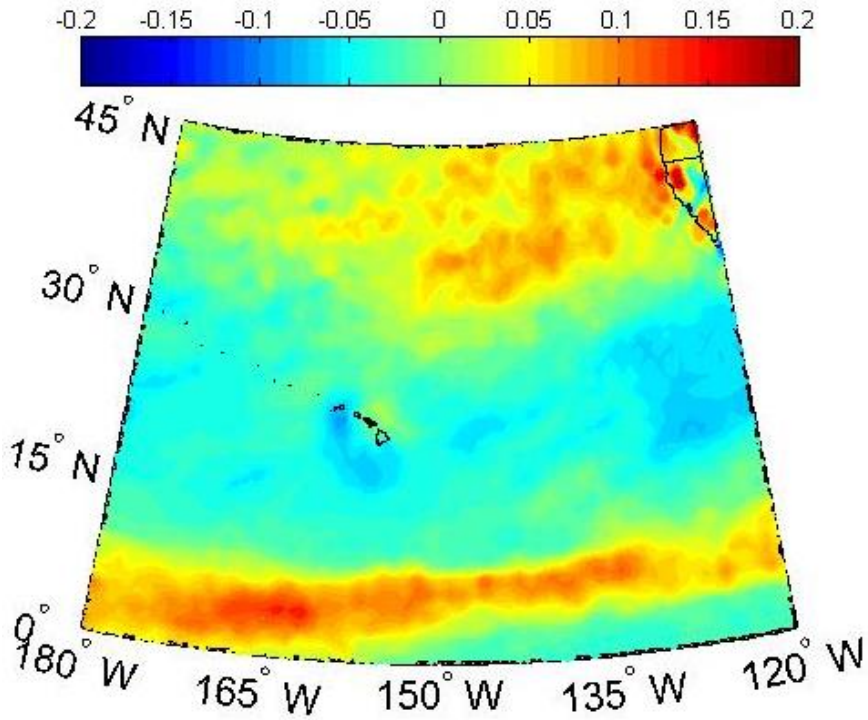

Figure 2.15. NCEP-FNL ω_{500} vertical velocities in Pa s^{-1} climatology for DJF 2010 El Niño. Positive values indicate rising motion and negative values indicate sinking motion.

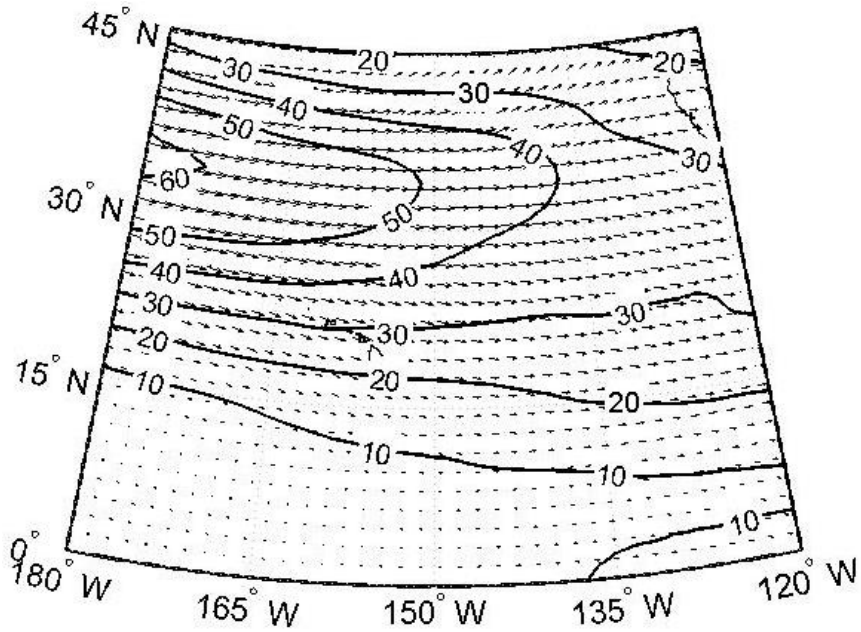

Figure 2.16. Mean 250 hPa wind vectors (m s^{-1}) and isotachs (10 m s^{-1}) for DJF 2010 El Niño from NCEP-FNL.

2.5.2 La Niña

The center of the NPSTH (1018 hPa) during the 2011 La Niña event covers a much larger area than both the DJF climatology and 2010 El Niño (Figure 2.17). Surface winds during cold episodes look much the same as they do during a climatological DJF. Maximum mean wind speed is located south of the island chain over latitude 15˚N across most of the domain. The minimum mean wind speeds (2 m s^{-1}) are approximately located along 30˚N with the islands contained in a region of 4 m s^{-1} mean surface wind speeds (Figure 2.18). Mean ω_{500} values show rising motion much closer to the north and south of the islands (2.19). Additionally, the polar jet is farther north of the islands near 35˚N (Figure 2.20). The position of the polar jet and NPSTH location lead to decreases the magnitude of subsidence above the BL which increases the islands' susceptibility to transient weather systems (Figure 2.20).

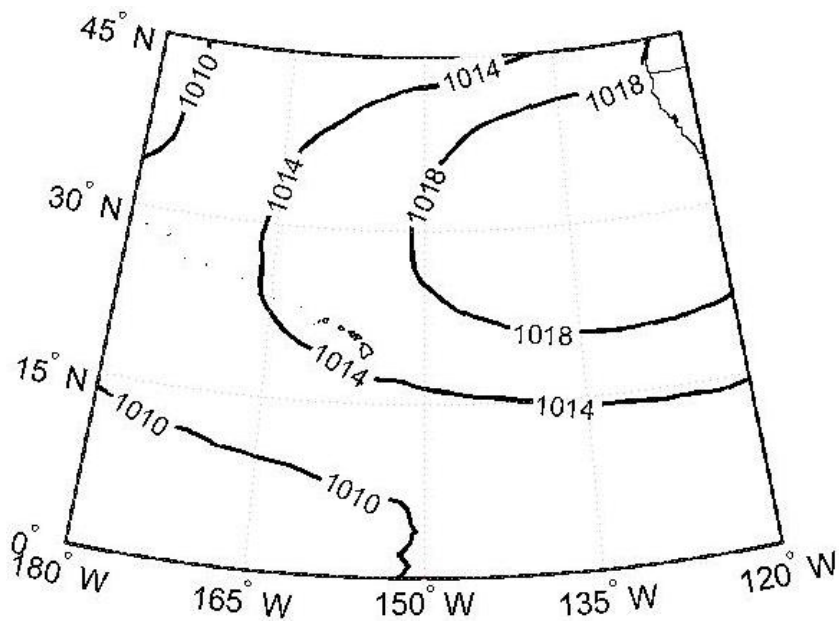

Figure 2.17. NCEP-FNL sea level pressure (hPa) climatology for DJF 2011 La Niña from NCEP-FNL.

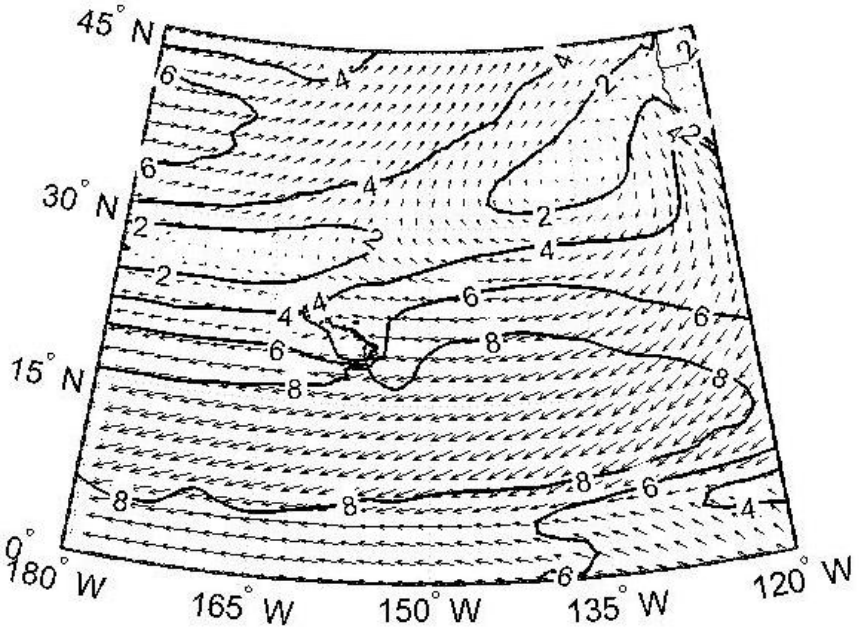

Figure 2.18. Mean surface wind vectors (m s^{-1}) and isotachs (2 m s^{-1}) for DJF 2011 La Niña from NCEP-FNL.

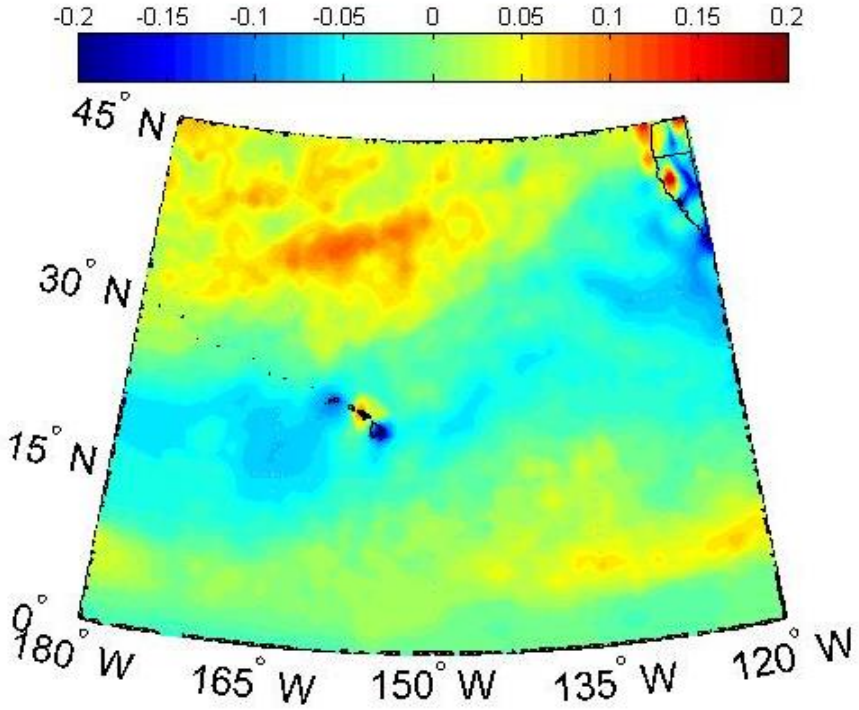

Figure 2.19. Same as figure 2.15 for DJF 2011 La Niña.

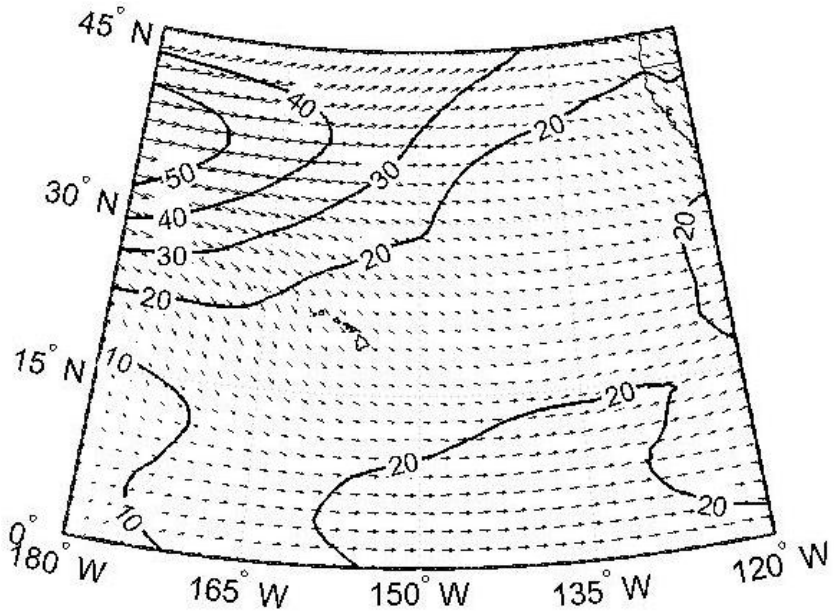

Figure 2.20. Mean 250 hPa wind vectors (m s^{-1}) and isotachs (10 m s^{-1}) for DJF 2011 La Niña from NCEP-FNL.

Chapter 3. Data and Procedures

3.1 Data

3.1.1 Constellation Observing System for Meteorology, Ionosphere, and Climate (COSMIC)

The primary data set used for this analysis consists of vertical refractivity profiles obtained through the Taiwan Analysis Center for COSMIC (http://tacc.cwb.gov.tw/cdaac/ 2014). At the time of this study, the data set is for the period June 2006 through December 2012. Omitted data includes JJA 2006 due to the uneven distribution of observations during the initial three months of operation; additionally data for DJF 2013 are not used due an incomplete season. As such, data for the seasonal z_i comparison consists of six total summer seasons (2007 - 2012) and six total winter seasons (2007 - 2012.) A summary of total observations used for the climatology of each season can be found in Table 3.1.

Table 3.1. Total global and domain observations for JJA 2007-2012 and DJF 2007-2012. Domain defined as 5˚N-45˚N and 120˚W-180˚W

Season (2007-2012)	Total Global Observations	Total Domain Observations	Domain percentage of Global
JJA	845495	34918	4.2%
DJF	827380	35409	4.3%

3.1.2 National Center for Environmental Prediction – Final (NCEP-FNL)

The NCEP-FNL Operational Global Analysis data are resolved on a 1˚ x 1˚ grid with 26 mandatory levels and initialized every six hours (http://rda.ucar.edu/datasets/ds083.2 2014). The data contained within this set are derived from the same model that produces the Global Forecast System (GFS) with the NCEP-FNL model initialized about an hour after the GFS in order to utilize the most recent available observations.

3.1.3 El Niño-Southern Oscillation (ENSO) Index

The Multivariate ENSO Index (MEI) available from the Earth System Research Laboratory Physical Science Division (ERSL-PSD) is used to identify ENSO warm and cold events (http://www.esrl.noaa.gov/psd/enso/mei/ 2014). The MEI is calculated monthly for the tropical Pacific using sea-level pressure, zonal and meridional surface wind components, sea surface temperature, surface air temperature, and total cloud fraction (ERSL 2014). El Niño events with an index value greater than 2 are considered strong while values between 1 and 2 are classified as weak to moderate (ERSL 2014). Conversely, La Niña events with an index value of -2 or less are categorized as strong with values between -1 and -2 as weak to moderate. An index value near 0 represents an ENSO neutral pattern (ERSL 2014).

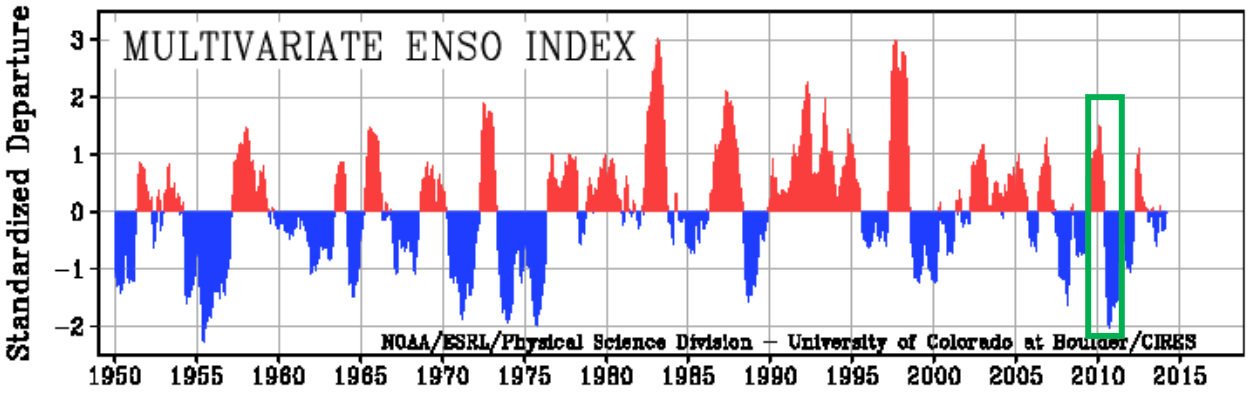

Figure 3.1. Multivariate ENSO index 1950-Present. Positive standard departures (red) represent El Niño events and negative standard departures (blue) represent La Niña events. El Niño (2010) and La Niña (2011) events used for this study are highlighted by green box. (http://www.esrl.noaa.gov/psd/enso/mei/ 2014).

Throughout the period 2006 – 2012, there were multiple occurrences of both El Niño (August 2006 – February 2007, June 2009 – May 2010) and La Niña (July 2007 – July 2008, June 2010 – May 2011, August 2011 – April 2012). Comparisons between ENSO and non-ENSO seasons will be investigated in order to identify variations of the inversion base when compared to climatology values.

3.1.4 CMORPH Precipitation Estimates

The Climate Prediction Center (CPC) MORPHing technique (CMORPH) produces global precipitation estimates at a spatial resolution of 0.25˚ x 0.25˚ every three hours. The CMORPH technique estimates precipitation using data from passive microwave and infrared satellite observations from overlapping 5 degree latitude/longitude regions at 2.5 degree intervals (Joyce et al. 2004). Algorithm inputs include GOES and METEOSAT data at 10.7 micrometers (μm) and 11.5 μm, as well as microwave satellites such as TRMM, AQUA, DMSP -13,-14,-15; NOAA -15, -16,-17; AMSU-B and SSMI (CPC 2014). The morphing technique is used to interpolate large scale precipitation patterns between each areal satellite scan. Data morphing operates under the assumption that the radial wind speeds of any system are constant, allowing between scan propagation of large scale precipitation patterns to be estimated (Joyce et al. 2004).

3.1.5 High Resolution WRF-ARW 6 km

The high-resolution Advanced Research Weather and Forecasting (WRF-ARW) model (Skamarock and Klemp 2008) provides 18 km, 6 km, and 2 km horizontal resolution simulations at 38 vertical levels over the Hawaiian region (Hitzl 2013; Hitzl et al. 2014). The initial boundary conditions for the WRF model are from the NCEP Climate Forecast System Reanalysis (CFSR) (Saha et al. 2010). The 6 km regional domain covers the eight major islands of Hawaii and will be used in this analysis to simulate surface flow (m s^{-1}), vertical motion (cm s^{-1}), and total precipitable water (TPW) (mm) for comparison to apparent island wake effects observed by GPS RO. Additionally, modeled pressure (hPa), temperature (K) and water vapor mixing ratio (g kg^{-1}) will be used in the refractivity equation (Chapter 1, Eq. 1.1) to test the ability of the WRF model to resolve the inversion base using the refractivity calculation.

3.2 Procedures

3.2.1 Grid Size Selection and Observation Distribution

The initial resolution for the analysis was 1° x 1° over the domain 5°N – 45°N and 120°W – 180°W. However, the average seasonal distribution was dependent upon the amount of usable data. To begin the analysis, multiple grid sizes were considered using the average number of observations over the analysis region (Table 3.2).

Table 3.2. Number of observations per grid box over the Hawaiian region 5°N – 45°N and 120°W – 180°W (Seasonal average).

Grid Size (40^0 x 60^0 Domain)	Number of Individual Grids	Number of Observations Over the Domain (all season average)	Average Number of Observations per Grid Box
1^0 x 1^0	2400	34713	14
2.5^0 x 2.5^0	384	34713	90
5^0 x 5^0	96	34713	361
5^0 x 10^0	48	34713	723

The use of a 2.5° x 2.5° grid divides the domain into 384 separate boxes increasing the average number of observations per grid to 90; average values were also calculated for grid sizes of 5° x 5° (361 observations) and 5° x 10° (723 observations). A grid size of 5° x 5° was chosen in order to maintain a balance between analysis grid size and the number of observations per grid. While the zonal distribution of observations is relatively constant over a season, the number of observations increases with increasing latitude. Figure 3.2 is an example of the JJA climatology distribution of observations over the domain. It should be noted that the number of observations is an average over the entire domain. The seasonal climatology shows the average number of observations per grid box; however this can be somewhat misleading because daily GPS RO observations are not distributed evenly over the entire domain. To illustrate this point, Appendix 1 shows the location of GPS RO observations for one day, one week, and one year for both JJA

and DJF. The result shows that while seasonal coverage of observations over the entire domain are uniform, daily observation values at a given grid box are subject to the distribution of the daily observations which should not be assumed to be even (Appendix 1).

These totals compare favorably to a previous study over the SE Pacific Ocean using a similar domain of 0°S – 50°S and 140°W – 70°W. Xie et al. (2012) used RO data in a 5° x 5° grid resulting in an average of approximately 160 profiles per grid box near 50°S and ~ 50 profiles per grid box from 10°S towards the equator.

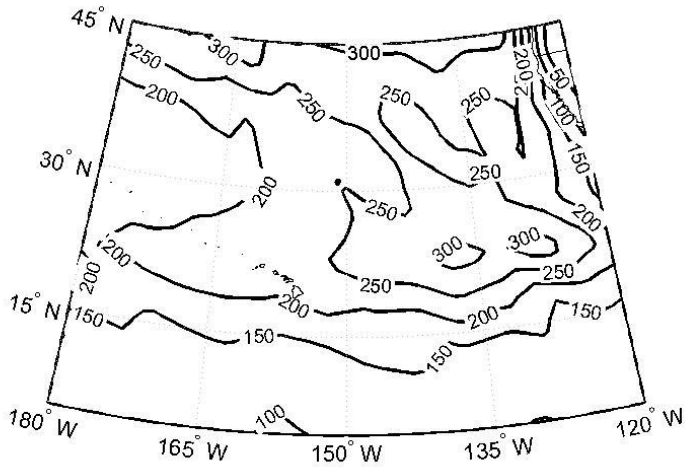

Figure 3.2. Average GPS RO observations (per 5˚x5˚ grid box) distribution for seasonal climatology JJA 2007-2012.

3.2.2 Refractivity to Identify Inversion Base Height

The dependence of refractivity on water vapor allows for identification of z_i (Guo et al. 2011; Ao et al. 2012; Xie et al. 2012). Refractivity can be measured directly or calculated as Smith and Weintraub (1953) demonstrated using the relation of N to P, T, and P_w (Chapter 1-Eq. 1.1). The relationship between T and P_w is such that, both cannot be calculated from refractivity. However if one value is known from ancillary data the other can be calculated (Ware et al. 1996 and Guo et al. 2011). In the case of the relationship between T and P_w, if reasonably accurate (±2 K) yet independent T values are available, values of P_w can be obtained within ±0.5 hPa (Anthes et al. 2000). Conversely, to obtain T estimates of ±1 K, P_w must have an estimate with accuracy of

±0.25 hPa (Anthes et al. 2000). Ao et al. (2012) and Xie et al. (2012) utilized the vertical refractivity value (Smith and Weintraub 1953) differentiated with respect to height (Chapter 1-Eq 1.2). Regions without the presence of a sharp transition at the BL top typically have a refractivity gradient of -40 N-units km^{-1} or greater. In instances of a sharp gradient, values of -80 N-units km^{-1} are common. However, a minimum threshold is not defined and the BL top is identified in any vertical profile as the most negative value of the profile's vertical refractivity gradient.

Earlier methods of detecting z_i utilized the quantities of potential temperature, virtual potential temperature, or water vapor measurements (Basha and Rantam 2009). These radiosonde measurements are compared to similar results of observed refractivity. Vertical profiles of water vapor and refractivity both show a sharp decrease with height, resulting in a steep, negative gradient (Figure 3.3). As such, it was found that the refractivity detected BL top (inversion base) compared very well with those of potential temperature, virtual potential temperature and mixing ratio (Basha and Rantam 2009).

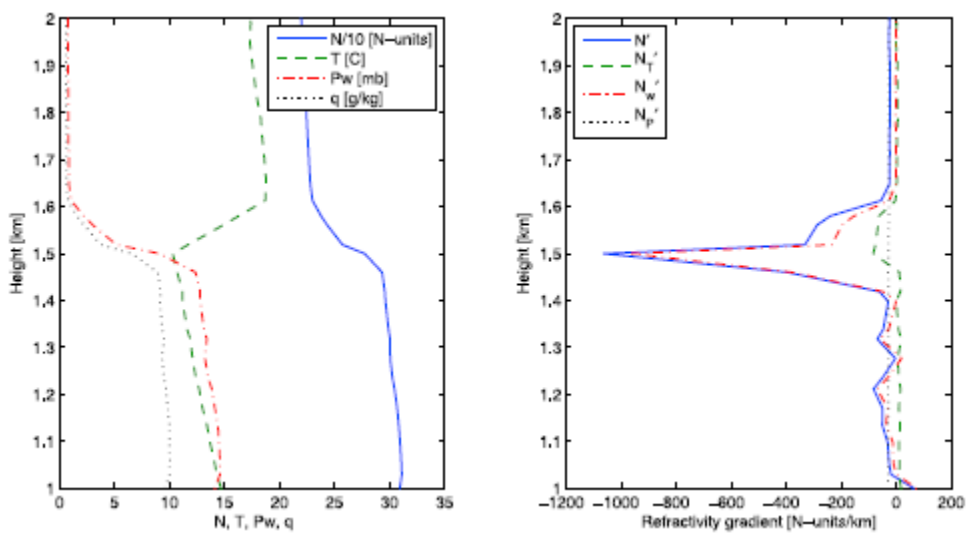

Figure 3.3. Left - Vertical profiles of refractivity in N-units (blue solid), temperature in ˚C (green dashed), water vapor partial pressure in hPa (red dashed), and mixing ratio in g kg^{-1} (purple dotted). Right – Vertical profiles of refractivity gradient equation components (N'-blue solid), temperature (N_T' – green dashed), water vapor pressure (N_W' – red dashed), and mixing ratio (N_P' – purple dotted). From Ao et al. 2012.

3.2.3 Relative Minimum Gradient (RMG)

The relative minimum gradient (RMG) is a unitless value used to quantify the inversion strength within a given profile. The RMG (N'_{rmg}) is calculated by dividing the minimum refractivity gradient (N'_{min}) by the root mean square of the refractivity gradient (N'_{rms}) over a specified layer of the profile. A sharp inversion layer is defined by a RMG value of 2 or greater (Ao et al. 2012).

$$N'_{rmg} = -\left(\frac{N'_{min}}{N'_{rms}}\right) \qquad \text{(Eq. 3.1)}$$

$$N'_{rms} = \sqrt{\frac{1}{n}(N_1'^2 + N_2'^2 + \cdots + N_n'^2} \qquad \text{(Eq. 3.2)}$$

3.2.4 Base and Height Constraints

The refractivity gradient method will be used to estimate the inversion base throughout this thesis. This method uses GPS RO to identify z_i by the point at which a sharp, negative gradient occurs in the vertical refractivity profile (Ao et al. 2012; Xie et al. 2012). Table 3.3 contains a summary of base, height, and refractivity value constraints for previous studies as well as for this thesis. A minimum penetration depth to within 500 m above mean sea level is required for a valid sounding profile, any sounding which does not penetrate to within 500 m of the surface will be discarded (Guo et al. 2011; Ao et al. 2012; Xie et al. 2012). Maximum height thresholds for z_i detection from previous studies vary from 6000 m (Ao et al. 2012) to 5000 m (Xie et al. 2012) to a low of 3500 m (Guo et al. 2011). Taking the previous studies into consideration 3500 m will be used as the maximum height at which the inversion must be detected for this analysis. With the implementation of the data constraints, the number of observations used in this analysis is roughly 50% of the total number of observations. The previous studies using GPS RO found a similar percentage of useable data according to their analysis criteria.

Table 3.3. Comparison of basic RO criteria (minimum and maximum height constraints and refractivity values) from previous research (Guo et al. 2011; Ao et al. 2012; Xie et al. 2012).

	Sample Grid Size	Minimum R.O. Depth (m)	Identification Method	Maximum RO Height (m)
Guo et al. (2011)	5° x 10°	500	- 50 N-units	3500
Ao et al. (2012)	5° x 5°	500	Minimum (N-units km^{-1})	6000
Xie et al. (2012)	5° x 5°	500	Minimum (N-units km^{-1})	5000
Winning et al. (2014)	5° x 5°	500	Minimum (N-units km^{-1})	3500

Monthly median z_i statistics (Bingaman 2005) showed the highest radiosonde detected heights for Hilo and Lihue were 2310 m and 2080 m respectively. Similar values were identified in the analysis by Guo et al. (2011) over the area 20˚N-28˚N, 115˚W-160˚W. Standard deviation values for the median height are approximately ± 0.5 - 0.7 km (Guo et al. 2011). Based on work from previous studies, the height of the lowest N gradient was selected to represent z_i.

3.2.5 Sounding Examples

Examples of sample skew-t/log p diagrams can be found in Figures 3.4-3.6 as well as Appendix 2. In each diagram, the vertical temperature and dewpoint temperature profiles are derived from the retrieved refractivity value observed by GPS RO. To illustrate the technique used to find the base of the inversion, samples of soundings are provided with the approximate pressure level of the maximum refractivity gradient and moisture profile highlighted by a red arrow. Figure 3.4 is a case which has a calculated z_i of 1.4 km at a pressure level of 868 hPa. Although this does not have the typical sharp dry layer expected with an inversion sounding, the algorithm which identifies the minimum gradient with a value of -86.22 N-units km^{-1}.

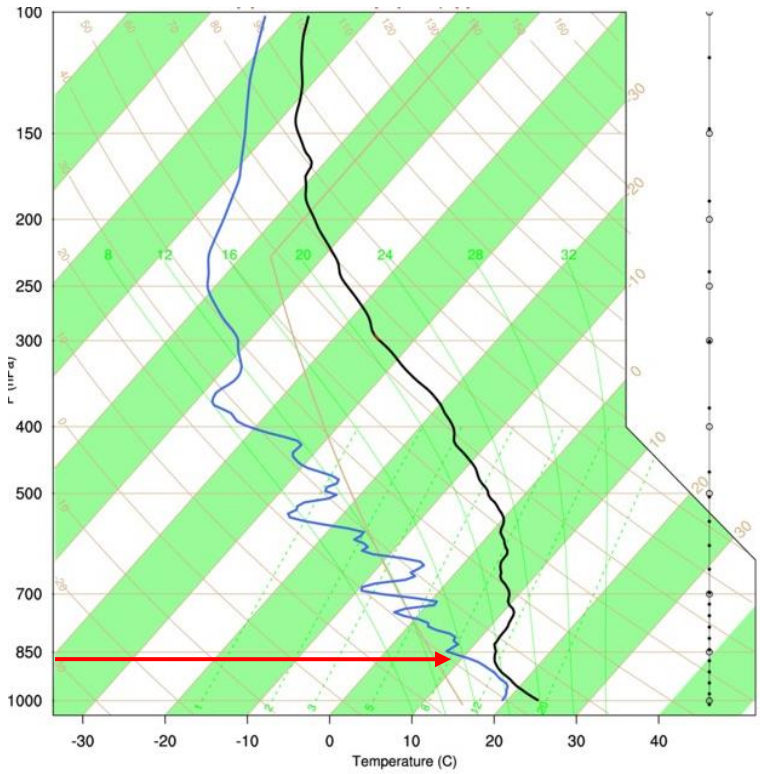

Figure 3.4. Example sounding from 2234 2 June 2007 2234 HST. The blue line (left) represents the dewpoint temperature profile. The black line (right) represents the temperature profile. Red arrow illustrates the reference pressure level of minimum refractivity gradient. Sounding data was obtained from the Taiwan Analysis Center for COSMIC (http://tacc.cwb.gov.tw/cdaac/ 2014).

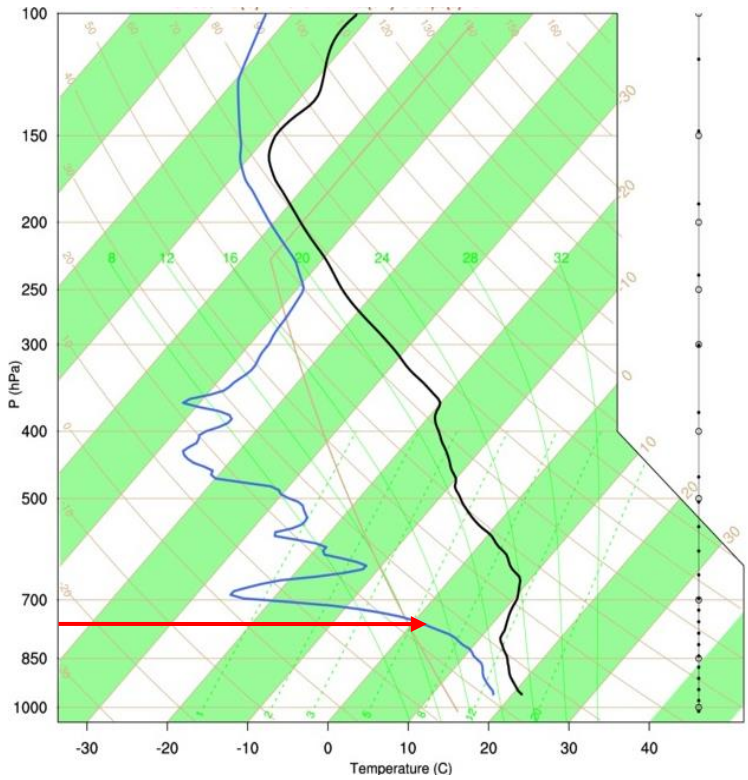

Figure 3.5. Example skew-t sounding from 0942 HST 18 July, 2011. The blue line (left) represents the dewpoint temperature profile. The black line (right) represents the temperature profile. Red arrow illustrates the reference pressure level of minimum refractivity gradient. Sounding data was obtained from the Taiwan Analysis Center for COSMIC (http://tacc.cwb.gov.tw/cdaac/ 2014).

Figure 3.5 shows a more typical sounding with a higher inversion base (z_i = 2.3 km) and a minimum refractivity gradient of -64.95 N-units km^{-1} at the 775 hPa pressure level. An example of a sounding with a high inversion can be seen in Figure 3.6. In this example, the inversion has a sharp moisture decrease resulting in an equally sharp refractivity gradient of -69.08 N-units km^{-1} with a corresponding inversion height of 3.1 km, which is rather high for this region. However, it is located below the height constraint of 3500 m and is therefore used in the analysis.

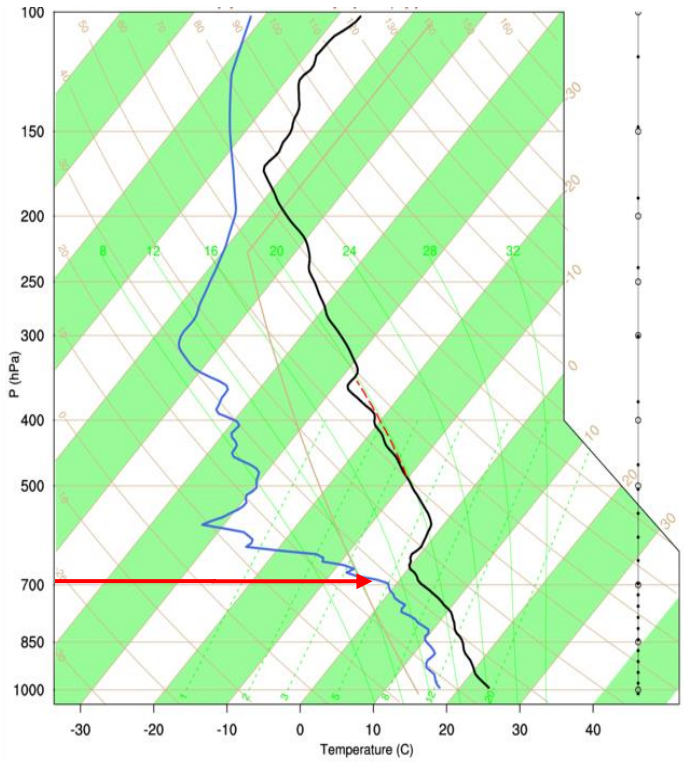

Figure 3.6. Example sounding from 1048 HST 29 July, 2007. The blue line (left) represents the dewpoint temperature profile. The black line (right) represents the temperature profile. Red arrow illustrates the reference pressure level of minimum refractivity gradient. Sounding data was obtained from the Taiwan Analysis Center for COSMIC (http://tacc.cwb.gov.tw/cdaac/ 2014).

3.2.6 Uncertainties in GPS RO Measurements

The initial uncertainty in regard to the RO method is the difficulty resolving the lowest ~2 km of the atmosphere (Ao et al. 2012). The presence of moisture in the lower atmosphere causes a super-refractivity condition which results in the inability of the GPS RO method to provide consistent measurements within the BL (Ao et al. 2012; Xie et al. 2012). However, even by decreasing the recorded refractivity gradient by the uncertainties introduced by the presence of moisture, the majority of gradient signals are still expected to be much stronger than the recorded gradients away from the point of super-refraction (Ao et al. 2012).

In regard to open ocean soundings, the areas with the lowest percentage of occultations reaching the specified minimum are located over the tropics. The cause is likely related to the ITCZ. In this region, strong convective mixing washes out the sharp moisture

gradient used to identify z_i (Ao et al. 2012). In the absence of a sharp moisture gradient, the refractivity gradient does not reach the minimum acceptable value (-50 N-untis km^{-1}) which accounts for a lower number of useable observations at low latitudes compared to middle latitudes. When deriving water vapor from observed refractivity values, uncertainty also lies in the method by which water vapor is calculated. Since it is necessary to use ancillary data of one to calculate the other, it was suggested by Kursinski et al. (2000) that ECMWF or NCEP models be used citing their global coverage and 6 hour run cycles allowing for the closest interpolation of time and location of a given sounding. That being said, it also introduces external sources of error into the calculation (Guo et al. 2011; Ao et al. 2012). To avoid allowing the uncertainty in temperature to impact the calculation of either variable, the water vapor based method should only be used in regions where a sharp moisture gradient is a common occurrence (Ao et al. 2012 and Xie et al. 2012).

Chapter 4. Results: GPS RO Observation of Inversion Base Height

This chapter will begin by presenting a horizontal distribution of z_i over the central North Pacific Ocean (Figure 4.1). The RMG will be used to show the strength of the inversion as determined from GPS RO refractivity gradient profiles. Standard deviation for both z_i and RMG (Appendix 3) will be used to show the areas of greatest median value variability over the analysis region. Observations will also be presented to illustrate the diurnal variation of z_i for JJA as well as during ENSO warm and cool events. Results from the six available years of the COSMIC data will then be compared to previous studies using radiosonde data (Bingaman 2005).

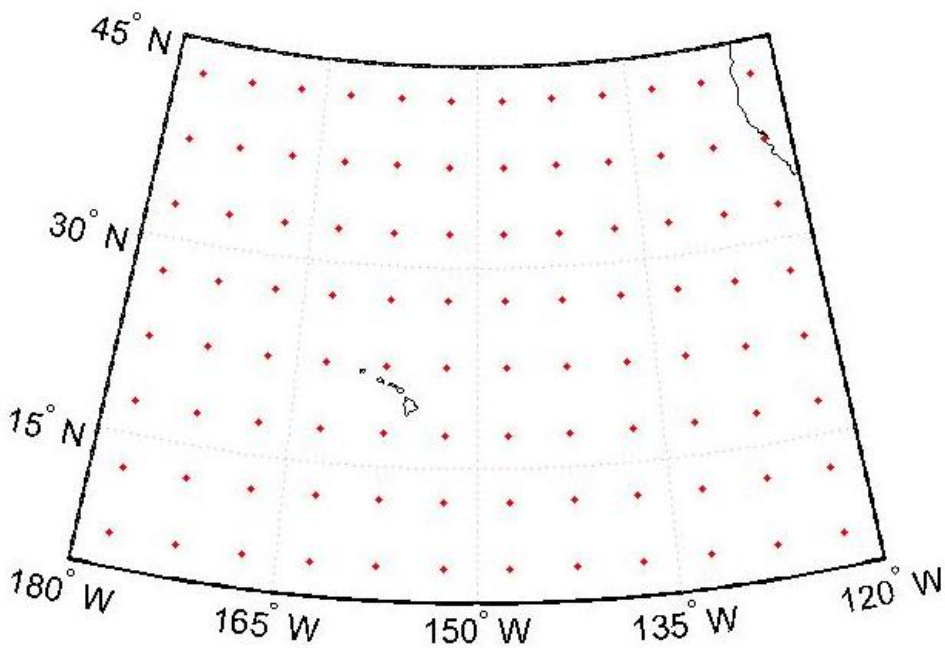

Figure 4.1. Central North Pacific analysis region (5˚N - 45˚N, 120˚W - 180˚W). Red dots show center of each 5˚x 5˚ analysis grid.

4.1 Annual Climatology

4.1.1 JJA 2007-2012

The spatial variation of z_i was examined over six seasons (2007 – 2012) for JJA and DJF. For JJA (Figure 4.2) the median z_i increases from a height of 900 m at approximately 30˚N, 120˚W to 2 km near 17˚N, 160˚W, in the lee of the islands. A standard deviation

for z_i of 0.5 km lies within the area 15˚N - 35˚N latitude between the islands and California; a standard deviation of 0.8 km is located west of 165˚W longitude (Figure 4.3). The median RMG for JJA 2007 – 2012 (Figure 4.4) shows the inversion in the analysis region is strongest along 120˚W latitude and weakens to the south and west with increasing distance from the NPSTH center. Additionally, increased convection when approaching the intertropical convergence zone (ITCZ) results in decreased RMG values due to the absence of a sharp inversion. Standard deviation of the RMG shows a value of 0.2 around the islands and 0.4 over a small area of the central California coast (Appendix 3, Figure A.3.1). The number of data observations for the JJA climatology increase with distance from the equator, from 100 per 5˚x5˚ for extreme southern grid points to 300 in the northern part of the analysis domain (Figure 4.5).

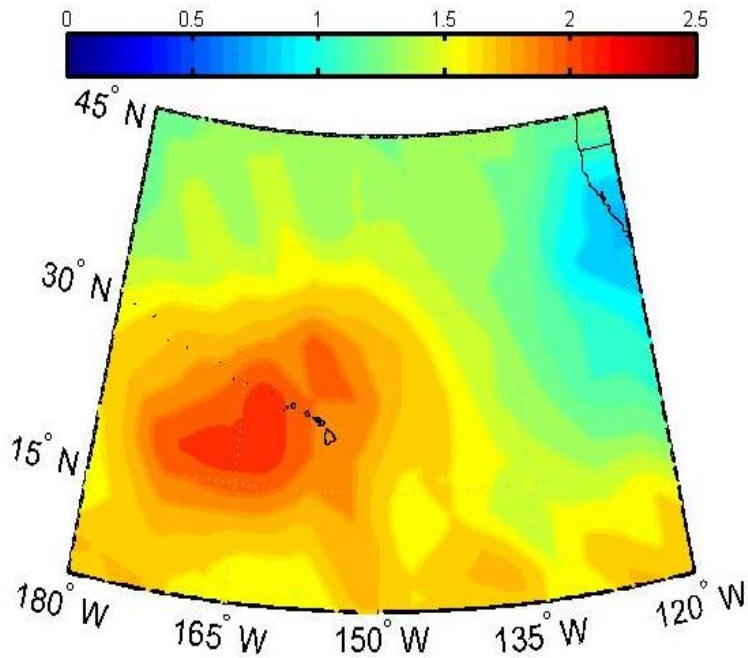

Figure 4.2. Median inversion base height (km) for JJA 2007-2012.

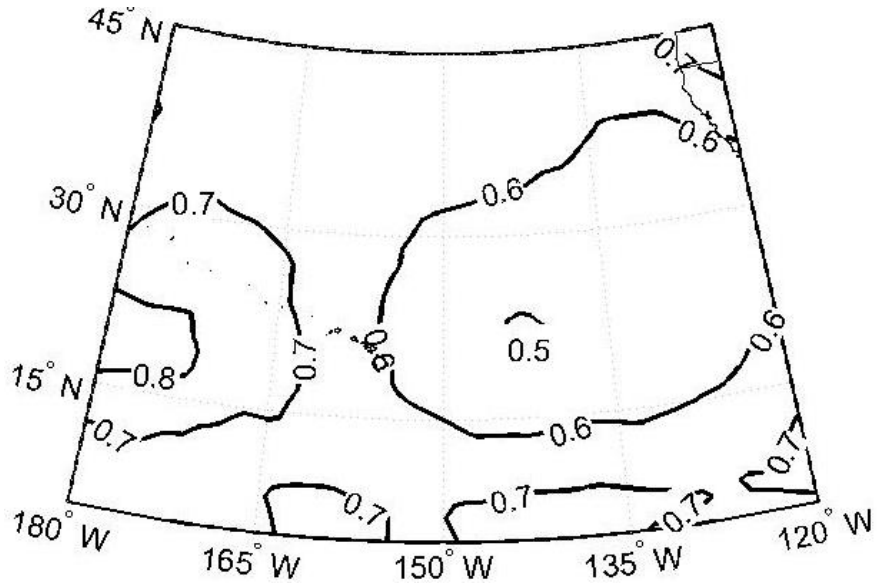

Figure 4.3. Standard deviation (km) of median inversion base height value for JJA 2007-2012.

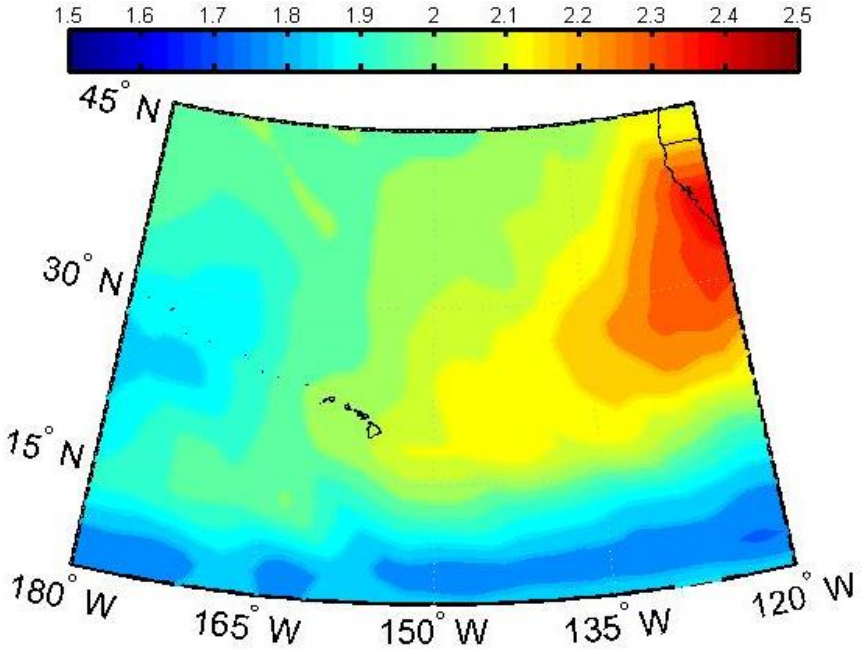

Figure 4.4. Median relative minimum gradient (unitless) for JJA 2007-2012.

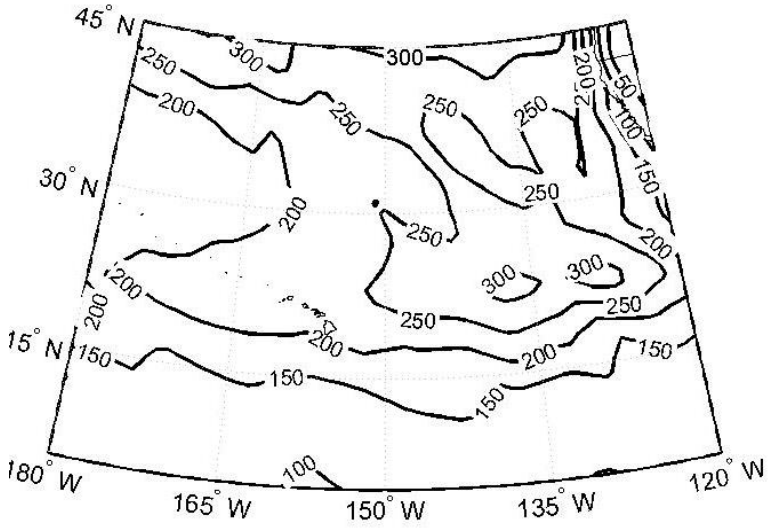

Figure 4.5. Horizontal distribution of total GPS RO observations per 5˚x5˚ grid point for JJA 2007 – 2012.

4.1.2 DJF 2007 – 2012

During the six year DJF climatology, the highest median z_i value (1.9 km) is located south of the Big Island at 15˚N, 155˚W while the low median value is located at the easternmost extent of the analysis domain and encompasses a much larger area, 25˚N-45˚N, along the 120˚W meridian (Figure 4.6). The standard deviation of median z_i values is 0.5 km at the same location during the DJF period, however the highest value has decreased to 0.7 km and is located between 10˚N and 15˚N latitude (Figure 4.7). The RMG shows a slightly stronger inversion centered at approximately 30˚N, 130˚W (Figure 4.8). The highest median RMG value of 2.25 for this region is greater in area and magnitude when compared to JJA climatology, however the standard deviation is higher during this time than summer with a value between 0.2 and 0.3 (Appendix 3, Figure A.3.2). The strength of the inversion is also greater over the Hawaiian Islands due to their proximity to the NPSTH. Observations for DJF over the domain increase on the order of 50 to 100 per grid box north of the 15˚N latitude line and stay relatively unchanged to the south with values of 150 per 5˚x5˚ grid box which decrease toward the equator (Figure 4.9).

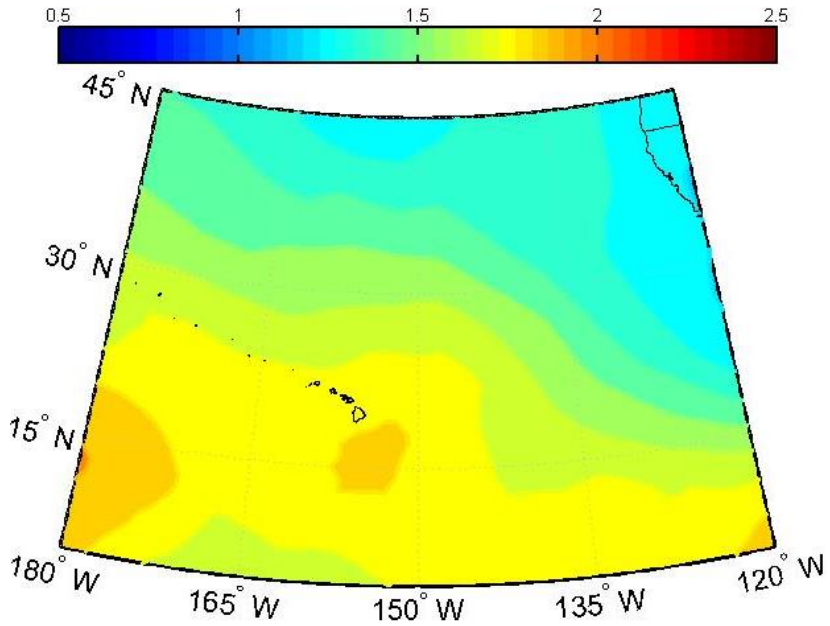

Figure 4.6. Median inversion base height (km) DJF 2007 – 2012.

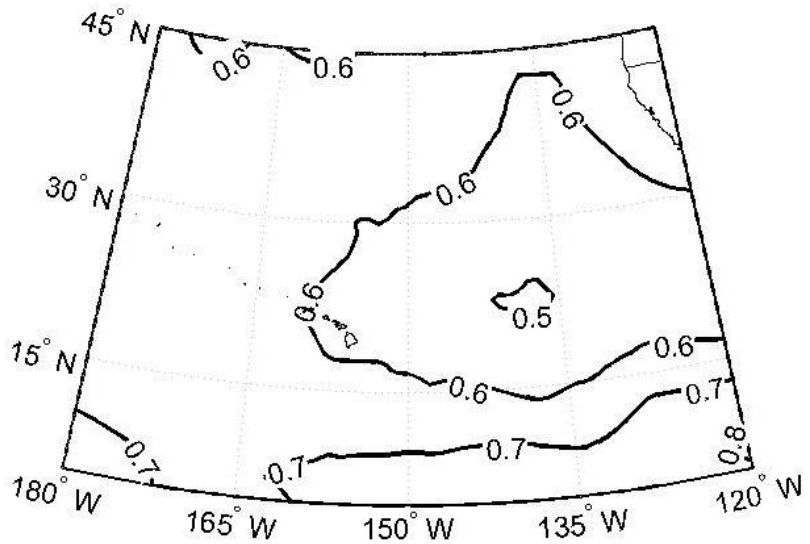

Figure 4.7. Standard deviation (km) of median inversion base height for DJF 2007 – 2012.

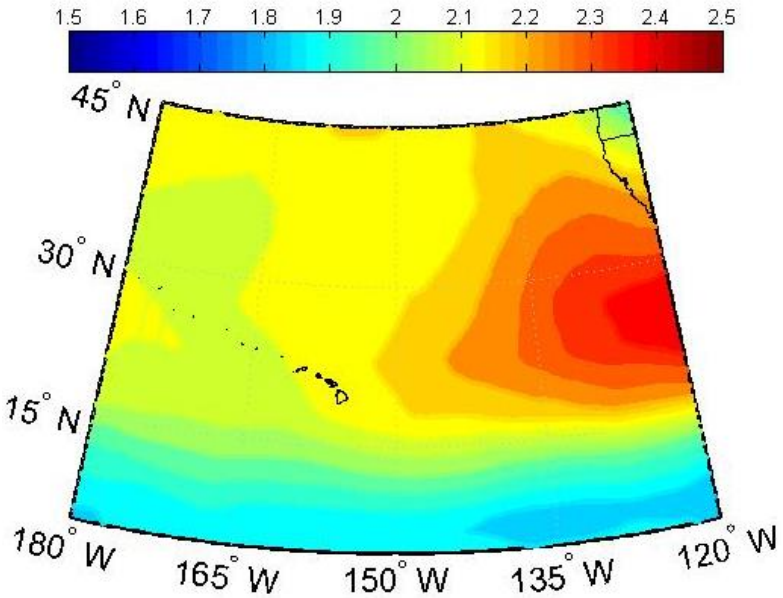

Figure 4.8. Median relative minimum gradient (unitless) for DJF 2007 – 2012.

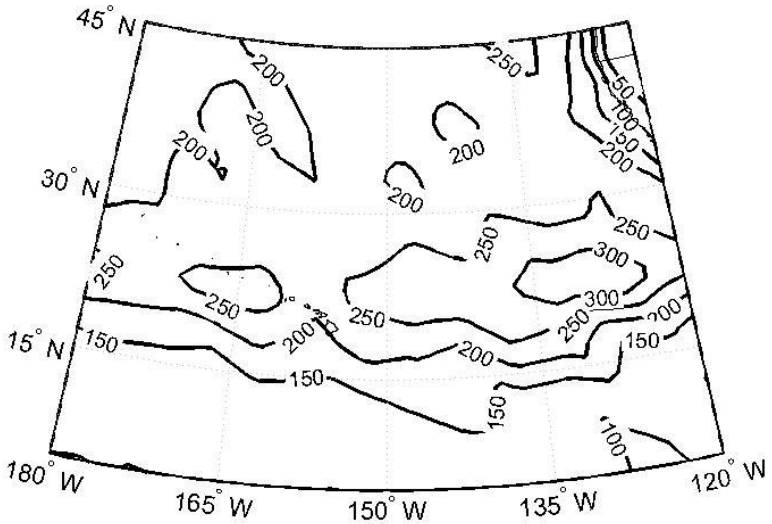

Figure 4.9. Horizontal distribution of total GPS RO observations per 5˚x5˚ grid point for DJF 2007 - 2012.

4.2 Trade Wind Flow Climatology

In order to specify the inversion over the Hawaiian region as the "trade wind" inversion, it is necessary to restrict any data not observed under the proper synoptic conditions. For this work, trade wind flow was defined by analyzing daily (00Z and 12Z) surface maps of mean sea level pressure (MSLP) from the NCEP-FNL initialization. The gradient flow from the NPSTH must not be influenced by Kona lows, tropical cyclones, cold fronts, or other disturbances (Figure 4.10). Any 12 hour period with a disturbance which interrupts or enhances the northeast flow, as seen in Figure 4.11, was not used in this part of the analysis. For the period 2007-2012, 87% of the total observation days qualified as trade-wind days during the JJA climatology period with a 47% occurrence during DJF. Approximately 58% of the 19,921 total observations were used for the JJA season while ~48% of the initial 17,357 were used for DJF. An entire list of trade wind dates for JJA and DJF can be found in Appendix 4.

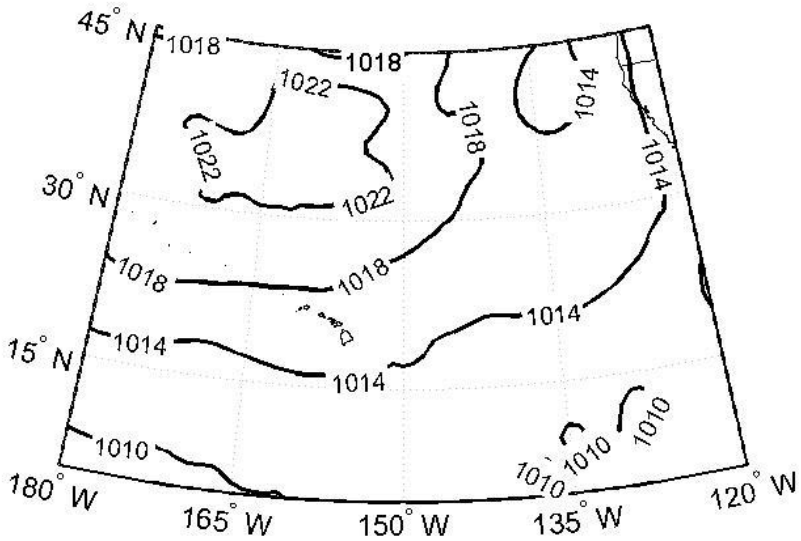

Figure 4.10. Example of undisturbed trade wind flow from NCEP-FNL MSLP (hPa) (00Z 18 July, 2012).

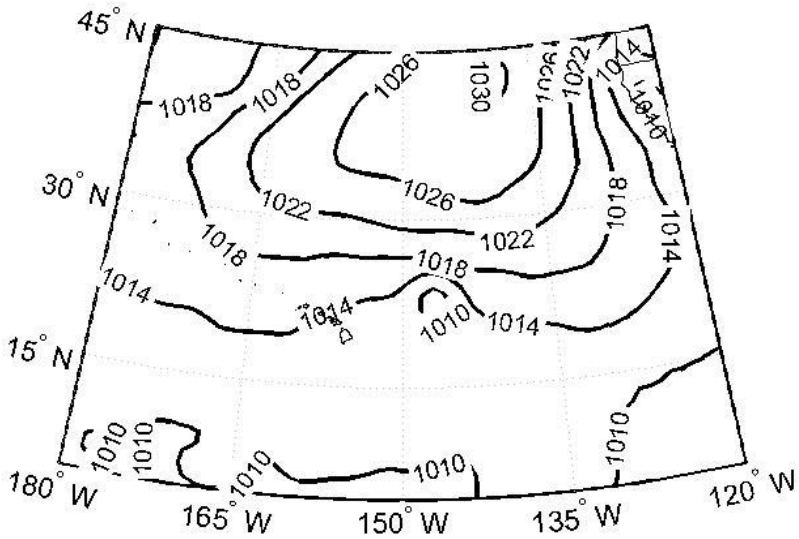

Figure 4.11. Example of disturbed trade wind flow from NCEP-FNL MSLP (hPa) (00Z 18 August, 2009).

4.2.1 JJA 2007-2012 Trade Wind Flow

For JJA 2007-2012, the surface flow was from the northeast 87% of the time. The interaction between the islands and the trade winds cause an increase in observed z_i. The high value for the median, still located on the leeward side of the islands, encompasses a much larger area and has a higher median z_i (Figure 4.12). Situated at 22.5˚N-162.5˚W, z_i is approximately 2.1 km and decreases from 2.0 km over Kauai to 1.9 km over the Big Island. When compared with the overall climatology during the same time period (Figure 4.1), z_i over the entire island chain is relatively unchanged; however the areal coverage of highest median z_i is larger. This suggests the presence of wake affects which the Hawaiian Islands have on the structure of the lower atmosphere. The standard deviation of the median z_i is similar, yet slightly lower for the region with a larger area of 0.5 km east of the islands, 0.6 km surrounding the island, and highest value (0.8 km) west 165˚W (Appendix 3, Figure A.3.3). The strength of the inversion is largely unchanged (Figure 4.13) when compared to that of the JJA climatology as is the standard deviation (Appendix 3, Figure A.3.4). The greatest median RMG value is still located adjacent to the California coast where the median z_i is at its lowest value. Overall, the number of total observations for JJA trade wind flow decreased, but minimum and maximum

observation areas did not. The maximum number of observations was located between the Islands and California coast with a secondary maximum within the 12.5˚N, 142.5˚W grid box (Figure 4.14).

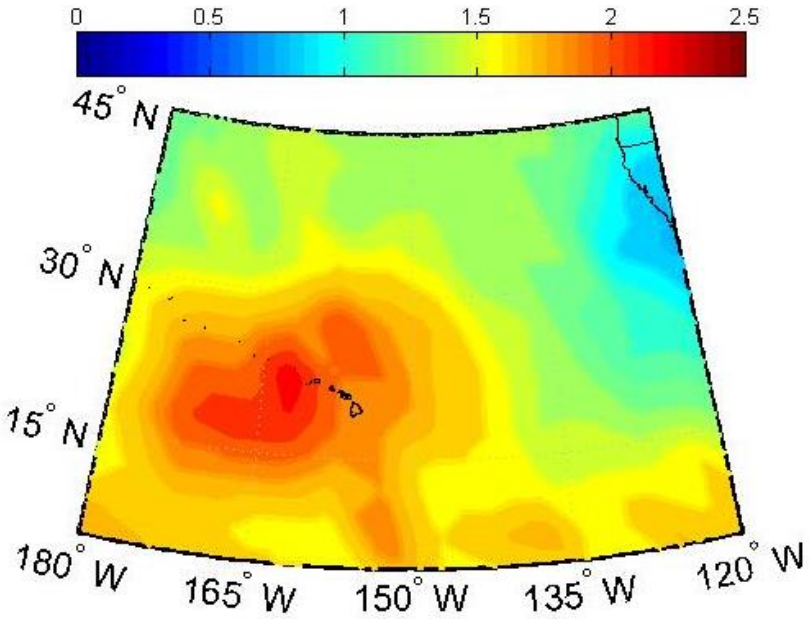

Figure 4.12. Median inversion base height (km) for JJA 2007-2012 trade wind flow.

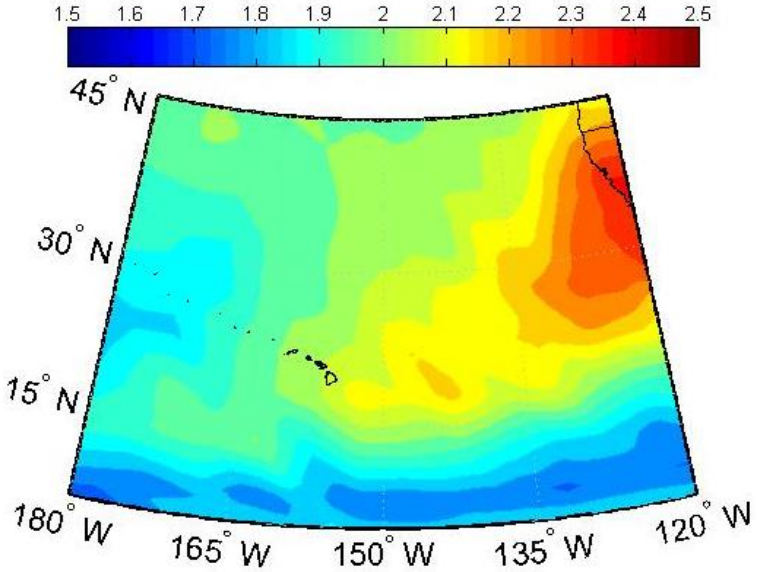

Figure 4.13. Median relative minimum gradient (unitless) for JJA 2007-2012 trade wind flow.

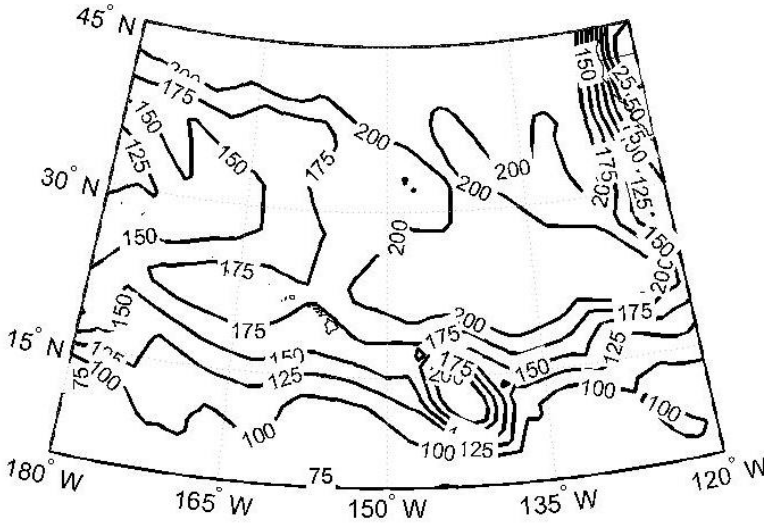

Figure 4.14. Horizontal distribution of GPSRO observations per 5˚x5˚ grid point (JJA 2007 – 2012) trade wind flow.

4.2.2 DJF 2007-2012 Trade Wind Flow

A similar increase of z_i occurs during the DJF season as well. Over the majority of the island chain, median z_i is between 1.7 and 1.8 km, with the inversion base over the Big Island estimated between 1.8 and 1.9 km. The highest median value (1.9 km) is centered near 15˚N, 150˚W and covers an area much larger than the highest climatological median height (Figure 4.15). The standard deviation of z_i during DJF decreases with a minimum value of 0.5 km over the entire island chain with values increasing southward toward the equatorial trough (Appendix 3, Figure A.3.5). The strength of the inversion also increases when compared to DJF climatology, however the locations are similar. The RMG factor of 2.4 adjacent to the California coast is also greater when compared to the climatological median. Additionally, the inversion strength over the islands is stronger with the 2.2 isopleth covering the Big Island while the rest of the island chain values are between 2.1 and 2.2 (Figure 4.16). The number of observations for DJF trade-wind flow is reduced by over 50% from climatology. The highest concentration of observations is located between the islands and the west coast of the U.S. and a secondary maximum within the 12.5˚N, 142.5˚W grid box which is the same location of the JJA-TW secondary maximum observation value (Figure 4.17).

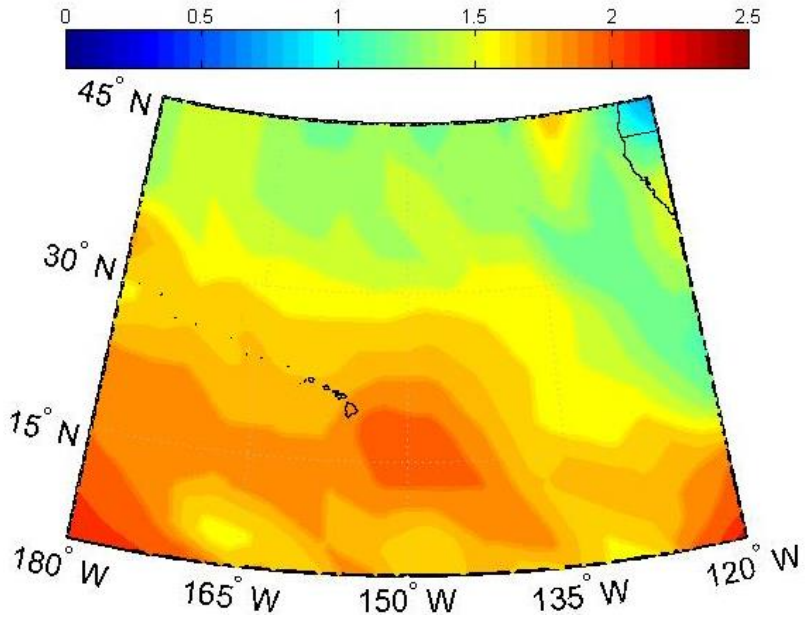

Figure 4.15. Median inversion base height (km) DJF 2007 – 2012 trade wind flow.

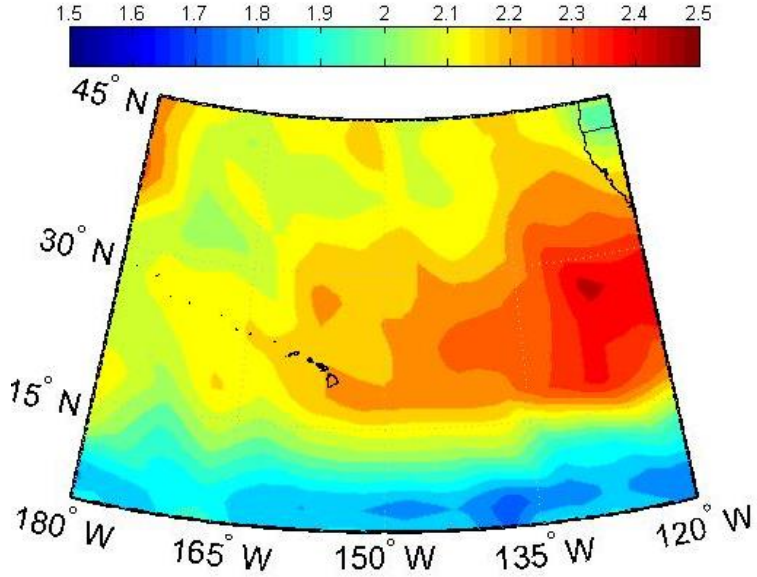

Figure 4.16. Median relative minimum gradient (unitless) for DJF 2007 – 2012 trade wind flow.

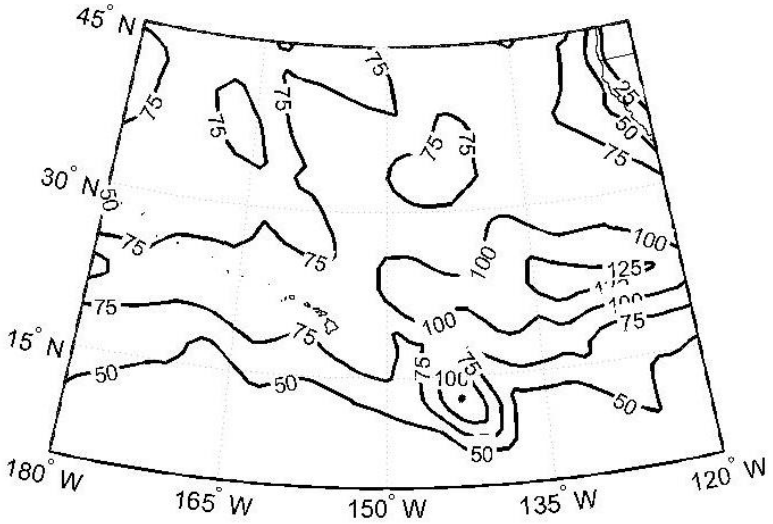

Figure 4.17. Horizontal distribution of GPSRO observations per 5˚x5˚ grid point (DJF 2007 - 2012) trade wind flow.

4.2.3 Annual climatology comparison

With a six year GPS RO observed climatology in place along with trade wind climatology for the same period, a comparison can be made to a similar study which utilized radiosonde data from Hilo and Lihu'e from 1999 through 2004 (Bingaman 2005).

For this comparison, the radiosonde data is limited to the vertical resolution of the GPS RO observations, which is to the nearest 100 meters. In terms of location, the comparison will be made from the isopleths between which the sounding site is located. With this being the case, comparison of z_i between the two methods return similar median height values (Table 4.1).

Table 4.1. Comparison between GPS RO and radiosonde observations of z_i (km) (Bingaman 2005).

	Hilo (Hawaii) - z_i (km)			Lihu'e (Kauai) - z_i (km)		
	Trade Wind (Radiosonde)	Climatology (GPS RO)	Trade Wind (GPS RO)	Trade Wind Radiosonde	Climatology (GPS RO)	Trade Wind (GPS RO)
JJA	2.1 - 2.2	1.9 - 2.0	1.8 - 1.9	1.9 - 2.0	1.9 - 2.0	2.0 - 2.1
DJF	2.0 - 2.1	1.7 - 1.8	1.8 - 1.9	1.7 - 1.8	1.7 - 1.8	1.7 - 1.8

The comparison for the Hilo sounding shows a higher median z_i of 200 to 300 m during JJA and DJF when compared to the total climatology (JJA-C and DJF-C) as well as during trade wind restricted JJA observations (JJA-TW). Values of z_i are slightly closer between measurements from radiosondes and trade wind restricted DJF satellite observations (DJF-TW). Overall, the most likely explanation for the difference between the radiosonde and satellite data observations is the spatial variability of the measurements. The Hilo sounding site is located on the windward side of the Big Island and upwind from Mauna Loa which has a summit above the inversion layer (4169 m). The observed z_i is affected by orographic lifting and blocking as a result of the high terrain of the Big Island. The upslope surface flow from the Pacific Ocean and downslope drainage flow from Mauna Loa oppose one another on the windward side and act to increase z_i (Garrett 1980; Grindinger 1992). This local effect is detected by radiosondes because of the sounding site location, but is on a scale too small to be detected by GPS RO.

Observations for Lihu'e on the island of Kauai are within approximately 100 m for JJA-C, DJF-C, and DJF-TW with all observations between 1.7 km and 1.8 km. During the JJA season, z_i for JJA-C and the radiosonde are both within the range of 1.9 – 2.0 km while the JJA-TW observation is between 2.0 km and 2.1 km. The differences between Hilo and Lihue are most likely due to the differences in terrain of the two islands. The highest point on Kauai is the peak of Kawaikini (1598 m) which is located below the lowest of z_i estimates (Schroeder 1993).

4.3 Diurnal Variation of Inversion Base Height

A comparison of the diurnal variation of z_i is restricted to a much smaller number of observations. Daytime (JJA-Day) is restricted to observations which take place between 1200 – 1800 HST while observations representative of nighttime (JJA-Night) conditions are restricted to 0000 – 0600 HST. The timeframes for diurnal observations were chosen to coincide with radiosonde observations (0200 HST and 1400 HST) and represent local daytime and nighttime conditions. For JJA, a total of 8274 observations fall within the daytime restrictions and 9023 observations for nighttime. Of the available observations

for JJA-Day and JJA-Night, approximately half are removed during the filtering process, leaving 4608 and 4564 observations respectively. This leaves the number of observations per 5˚x5˚ grid box ranging between 35 at the southern boundary of the domain to 65 at the northern boundary. With such a small number of observations over the analysis domain, there is the possibility for the measurement at any point to be influenced by outliers, even with the selective criteria. However, it is also an opportunity to test whether a smaller amount of observations used to calculate the median z_i is a detriment to the analysis.

Both time frames feature a low median z_i value of 800 m at approximately 30˚N, 120˚W, and high median of 2 km (JJA-Night) and 1.9 km (JJA-Day) at approximately 20˚N, 162˚W (Figures 4.18 and 4.19). The small difference between the maximum z_i of JJA-Night and JJA-Day agree with the earlier study by Bingaman (2005) and could be attributed to propagation of the thermal wake in the lee of Kauai and the associated circulations due to the absence of a surface obstruction as low level flow clears the island chain (Yang et al, 2008; Jia et al., 2011). As a result, stronger vertical motion within the boundary layer causes an increase in convective mixing at the inversion base, forcing it to a higher height (Garrett 1980). The standard deviation values for both JJA-Day and JJA-Night range from 0.6 km to 0.7 km over the entire domain. For JJA-Day, the RMG values over the entire island chain are between 2.0 and 2.05 (Figure 4.20) with standard deviations of RMG between 0.2 and 0.3. For JJA-Night, the RMG values over the island chain are between 1.9 west of Kauai and 2.0 on the eastern side of the Big Island (Figure 4.21).

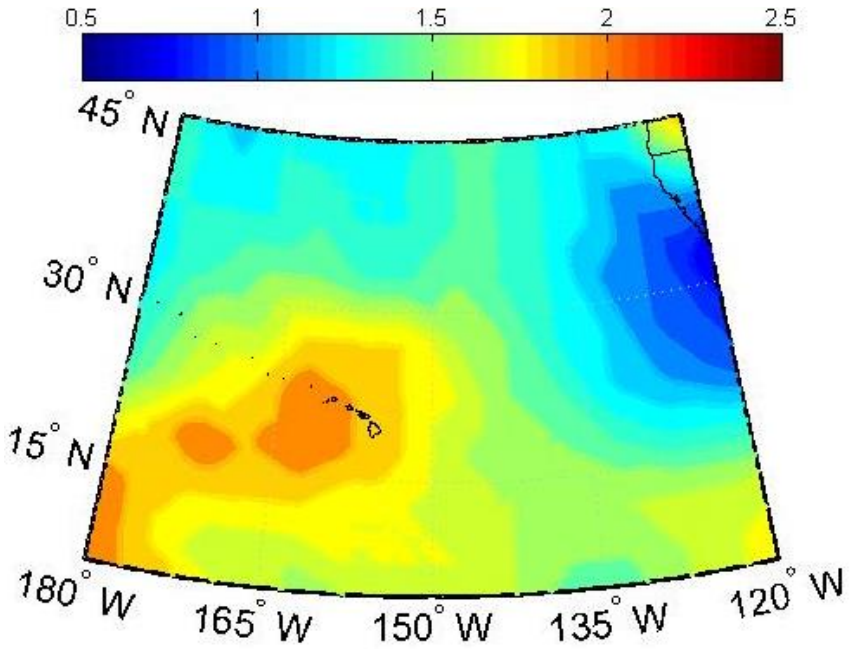

Figure 4.18. Median inversion base height (km) for JJA-Day (1200-1800 HST).

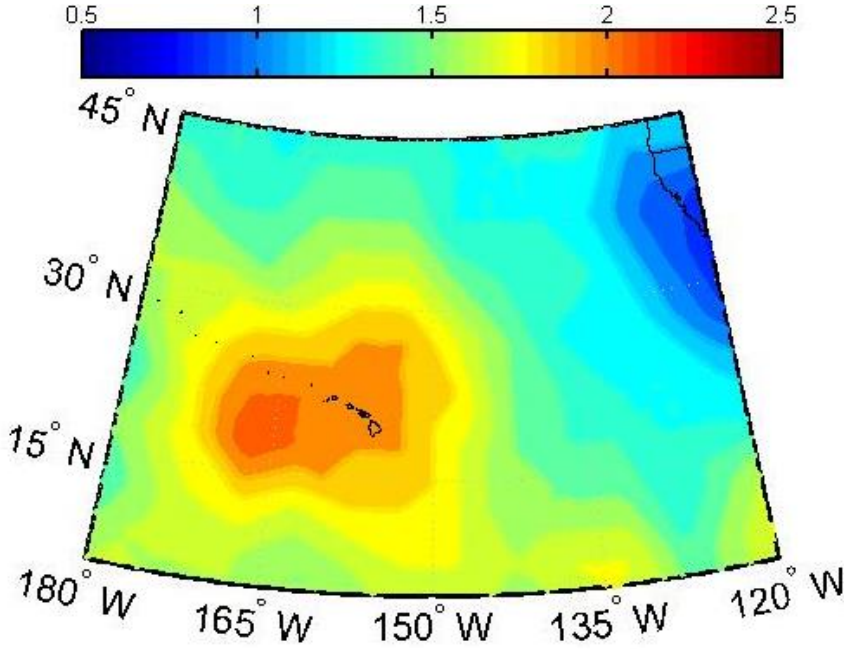

Figure 4.19. Median inversion base height (km) for JJA-Night (0000-0600 HST).

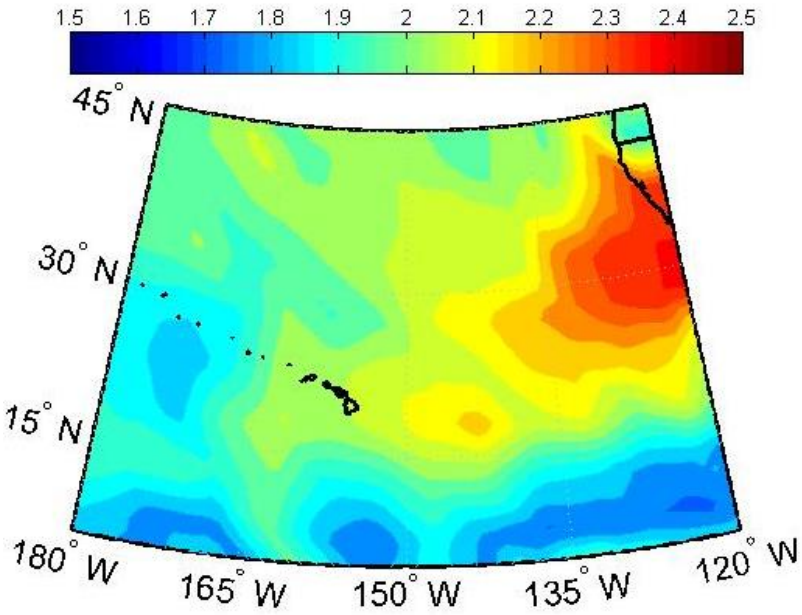

Figure 4.20. Median relative minimum gradient (unitless) for JJA-Day.

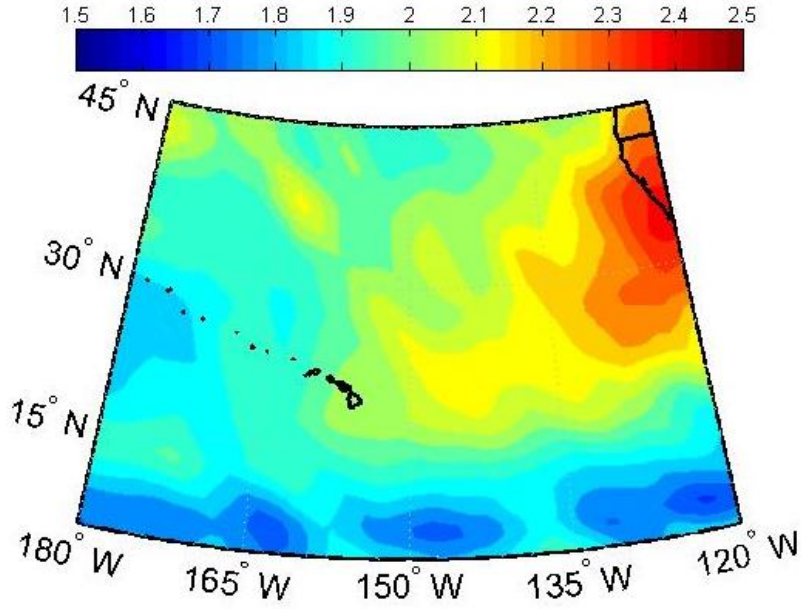

Figure 4.21. Median relative minimum gradient (unitless) for JJA-Night.

4.3.1 Diurnal Climatology Comparison

Despite the decrease in number of GPS RO observations, median height values compare favorably with the radiosonde study performed by Bingaman (2005). Similar to the seasonal climatology, observations of z_i at Hilo differ by approximately 200 - 300 m during both JJA-Day and JJA-Night (Table 4.2). The reason for the difference, as previously stated, is most likely due to the local circulation that takes place on the windward coast of the Big Island between onshore surface flow and downslope drainage flow from Mauna Loa (Garrett, 1980). For the island of Kauai, the Lihu'e observations also compare well with median z_i values from GPS RO observations differing by 100 – 200 m during JJA-Day and values for both within the 1.9 km – 2.0 km range for JJA-Night observations.

Table 4.2. Comparison between GPS RO (Satellite) and radiosonde (Radiosonde) observations of z_i (km) (Bingaman 2005).

	JJA-Day Hilo z_i (km)	JJA-Night Hilo z_i (km)	JJA-Day Lihu'e z_i (km)	JJA-Night Lihu'e z_i (km)
Radiosonde	2.1-2.2	2.1-2.2	1.8-1.9	1.9-2.0
Satellite	1.8-1.9	1.9-2.0	1.9-2.0	1.9-2.0

4.4 Observations of Inversion Base Height during ENSO

El Niño and La Niña events were identified using the MEI. A graphical representation of the MEI can be seen in Figure 3.1. An El Niño event (red) represents a positive standard departure of the composite MEI variables while a La Niña event (blue) represents a negative standard departure. A moderate El Niño occurred in 2009-2010 followed by a moderate to strong La Niña event in 2010-2011. As such, these events will be used for observation of z_i variation during DJF of each event. Similar to the diurnal climatology analysis, a caveat to observing only one season is the amount of available observations. In this case, the 2010 El Niño event utilizes 4876 observations for the months DJF 2010 while the 2011 La Niña event uses 2674 for DJF 2011. The year to year discrepancy in observations stems from the inactivity/malfunction of at least one of the satellites within the COSMIC constellation (COSMIC 2013).

4.4.1 El Niño – 2010

The 2010 El Niño was classified as a moderate event with a standard departure of 1.5. Using 4556 observations for DJF 2010, the GPS RO measured z_i shows a minimum median value of 1.2 km adjacent to the California coast, slightly north of 30˚N latitude along 120˚W longitude. The maximum median z_i value is a small area of 1.9 km centered near 15˚N, 165˚W, in the southwest of the islands, with a much broader area of 1.8 km encompassing the entire island chain (Figure 4.22). Comparison of El Niño vs. non-El Niño z_i agrees with previous conclusions (Bingaman 2005; Cao 2007) which observe no appreciable difference between the two data sets. The standard deviation values are largest to the north and south of the islands with values of 0.8 km along latitudes of 10˚N and 30˚N, while and area of 0.6 km covers the area above the islands (Appendix 3, Figure A.3.7). There is an axis of median RMG high values along 20˚N of 2.3 with nodes of 2.4 and 2.5 appearing near the California coast (Figure 4.23). Over the Hawaiian Islands, the median inversion strength is stronger during El Niño (2.3) than DJF climatology (2.1-2.2). Additionally, median z_i during El Niño is between 1.7 km and 1.8 km, similar to climatology values. Chu (1995) attributed the stronger inversion during an El Niño winter to increased upper level subsidence caused by the location of the Hawaiian Islands under the right exit region of the polar jet. The location of the islands under the exit region of the polar jet can also be seen in Figure 2.20 in Chapter 2.

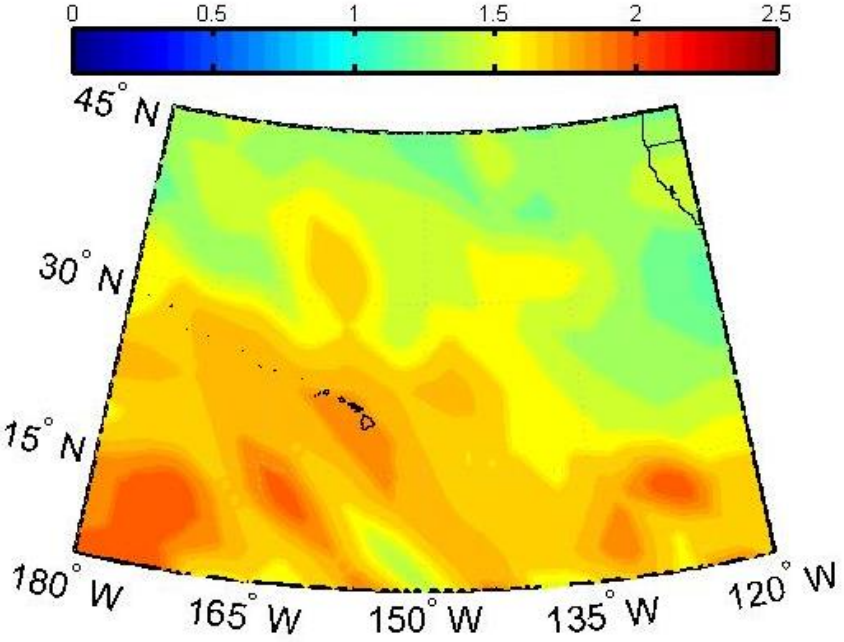

Figure 4.22. Median inversion base height (km) for El Niño (DJF 2010).

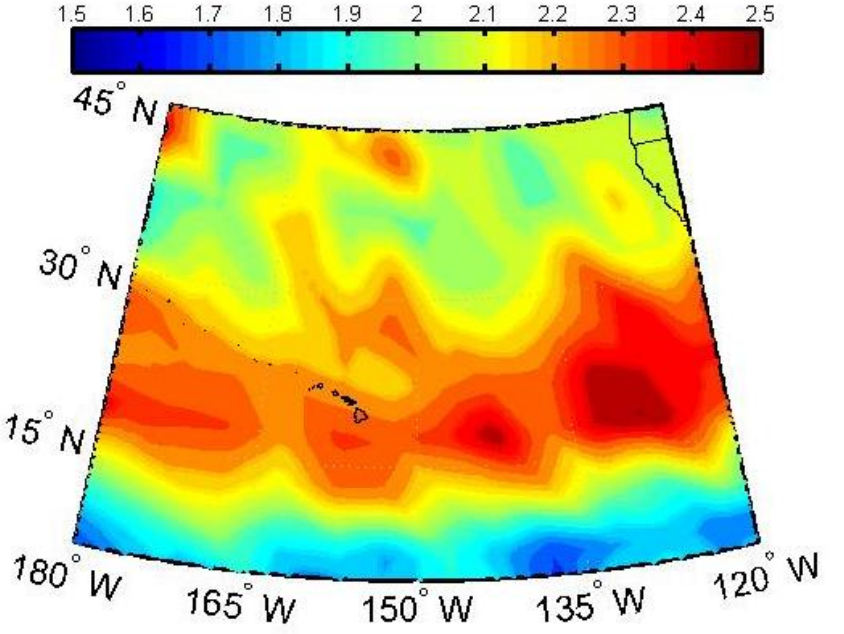

Figure 4.23. Median relative minimum gradient (unitless) for El Niño (DJF 2010).

4.4.2 La Niña – 2011

The Multivariate ENSO Index (MEI) classified the 2011 La Niña event as moderate to strong, with a standard departure value of -2 (Figure 3.1). During DJF 2011, the median z_i over Hawaii is between 1.7 km and 1.8 km, with highest median z_i values (2.2 km - 2.4 km) dispersed south of 15˚N (Figure 4.22). The small number of observations during DJF 2011 (n = 2508) is due to one or more inoperative satellites during the observation period. Standard deviation distributions for DJF 2011 show values of 0.6 km throughout the region with a high value (0.8 km) south of 15˚N (Appendix 3, Figure A.3.9). The resulting RMG shows the inversion strength decreases during this particular event (Figure 4.23). When compared to climatology, RMG during this La Niña event is 2.0 – 2.1 over Hawaii versus an RMG value of 2.1 – 2.2 over the same geographic region. The increase in median z_i and decrease in strength during this event were expected because a sharp inversion is less common with transient weather systems from both the north and south affecting the islands on a more frequent basis (Schroeder 1993).

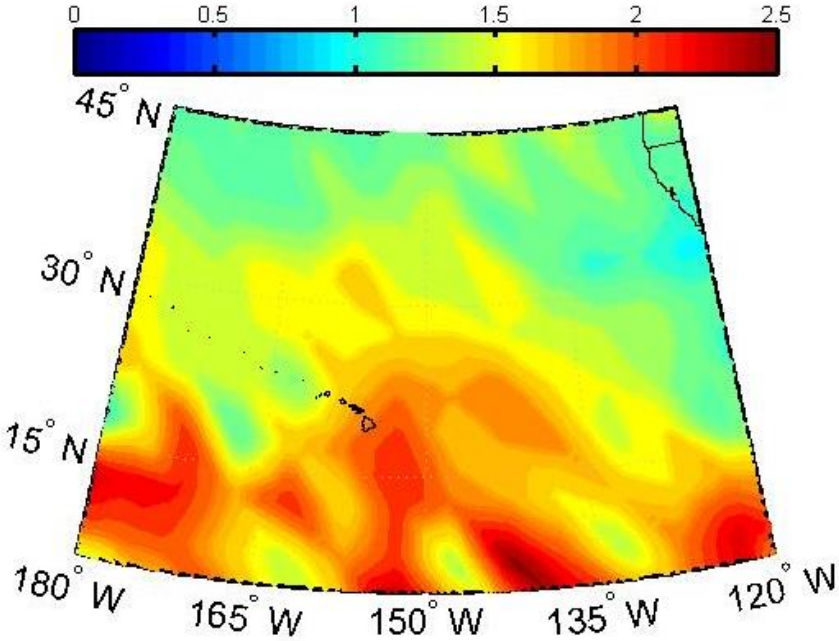

Figure 4.24. Median inversion base height (km) for La Niña (DJF 2011).

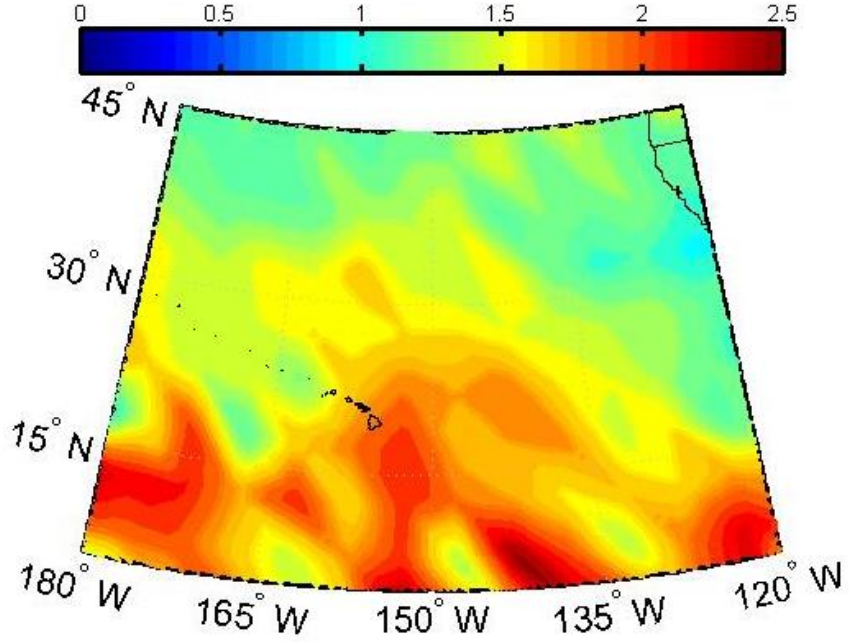

Figure 4.25. Median relative minimum gradient (unitless) for La Niña (DJF 2011).

Chapter 5. Statistical Analysis and Model Comparison

For the remainder of this analysis, GPS RO data will be partitioned in a 2.5 degree grid in order to focus the analysis over the Hawaiian region (Figure 5.1). Climatological summer (JJA-C, Figure 5.2) and winter (DJF-C, Figure 5.3) seasons as well as trade wind summer (JJA-TW, Figure 5.4) and winter (DJF-TW, Figure 5.5) z_i differences will be tested for statistical significance. Following the statistical comparison, the high resolution WRF 6 km model as well as CMORPH rainfall data will be utilized in order to determine if the observed GPS RO z_i increases in the island wake are detected by satellite estimated precipitation or high resolution model output. Finally, temperature, pressure, and mixing ratio data will be used within the WRF model to test the ability of the model to resolve the inversion base using the refractivity equation.

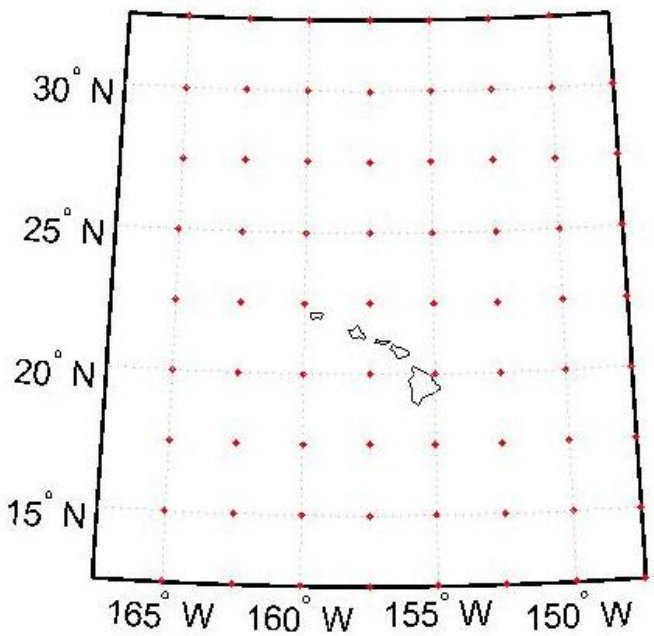

Figure 5.1. Representation of 2.5 degree analysis region (12.5˚N-37.5˚N, 147.5˚W-170˚W). Red dots mark the center of each 2.5 ˚ x 2.5˚ degree grid point.

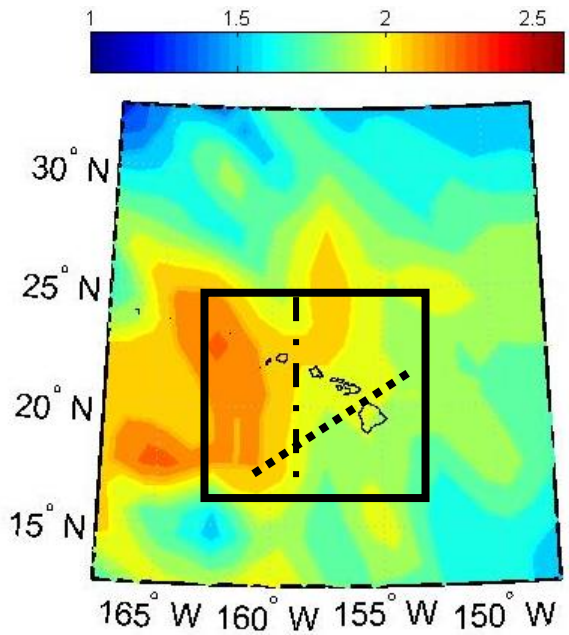

Figure 5.2. Median inversion base height (km) for JJA-C 2007-2012 for 12.5˚N-37.5˚N, 147.5˚W-170˚W (2.5˚x2.5˚ grid). Area within black box is the approximate domain of the JJA precipitable water climatology for 2007-2012 from the WRF-ARW in Figure 5.8 and precipitation climatology from CMORPH Figure 5.10. Black dash-dot line is the approximate location of 159˚W longitude used for Figures 5.11, 5.13, and 5.15 transect and black dotted line is the approximate location of 153˚W-160˚W diagonal transect to be used for Figures 5.17, 5.18, and 5.21.

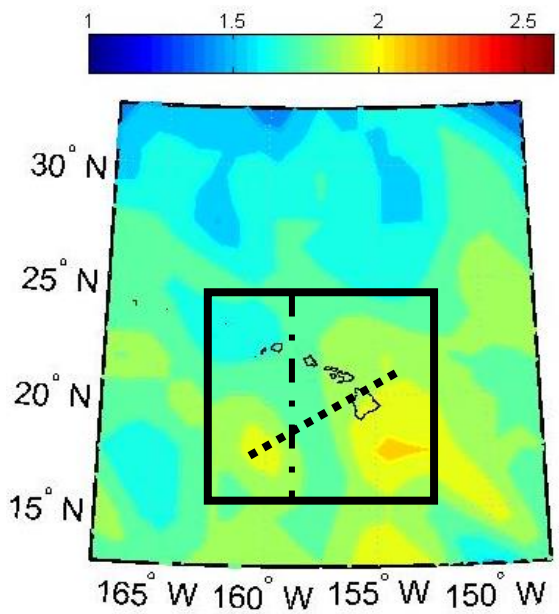

Figure 5.3. Same as in Figure 5.2 but for DJF-C 2007-2012. Area within black box is the approximate domain of the DJF precipitable water climatology for 2007-2012 from the WRF-ARW in Figure 5.9. Black dash-dot line is the approximate location of 159˚W longitude transect used for Figures 5.12, 5.14, and 5.16 and black dotted line is the approximate location of 153˚W-160˚W diagonal transect to be used for Figures 5.19, 5.20, and 5.22.

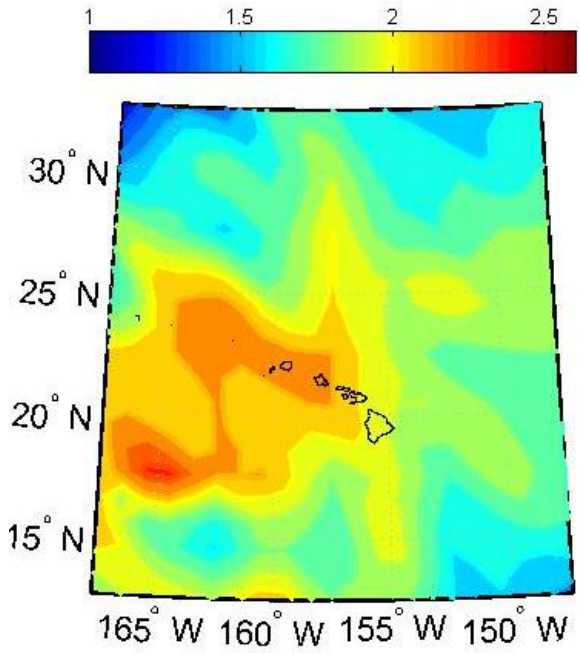

Figure 5.4. Median inversion base height (km) for JJA-TW 2007-2012 for 12.5˚N-37.5˚N, 147.5˚W-170˚W (2.5˚x2.5˚ grid).

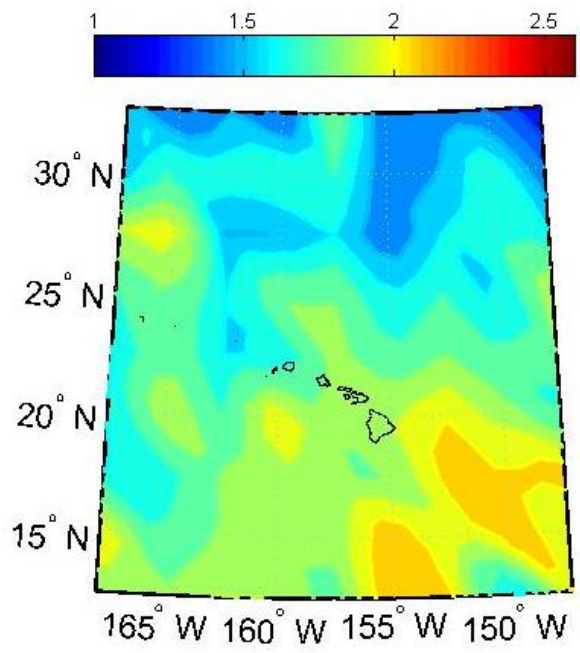

Figure 5.5. Same as Figure 5.4 but for DJF-TW 2007-2012.

5.1 GPS RO Difference Comparison

The differences in z_i will be shown by subtracting DJF z_i from JJA z_i for total climatology (Figure 5.6) and trade wind climatology (Figure 5.7). The statistical analysis will focus on the grid points which show the greatest change from JJA to DJF. In each season, these values are located at 17.5˚N, 165˚W (blue square) and 22.5˚N, 162.5˚W (red square). Additionally, grid location 20˚N, 157.5˚W (green square) will be analyzed as the focus shifts to observations in the wake of the islands. In order to determine the type of method to test for statistical significance, observations were compared with values for a normal distribution using a quantile-quantile (QQ) plot (Appendix 4). In each event, GPS RO observations were dispersed linearly along the line representing a normal distribution. With the distribution of observations classified as normal, a two tailed t-test was performed to determine the statistical significance of the seasonal difference in z_i at the same coordinate location. Histograms and corresponding QQ-Plots for all twelve observation periods can be found in Appendix 5.

5.1.1 Climatology Difference

The grid box centered on 17.5˚N, 165˚W has 32 observations for JJA-C and 42 for DJF-C. The difference between the median values of the two populations is 0.6 km. Comparison between the two yields a t value of 5.60 which is greater than the critical value of 2.00. The result verifies the z_i difference between the two seasons is statistically significant at a 95% confidence level. The same conclusion is reached for the grid box centered on 22.5˚N, 162.5˚W. With 121 total observations, a t value of 8.95 was calculated which is greater than the critical t value of 1.98. A climatological z_i difference of 0.1 km exists at location 20˚N, 157.5˚W (75 observations). The calculated t value of 1.42 is less than the critical value of 2.00 for this point. In the case of the wake grid point, the null hypothesis is accepted confirming there is no statistical difference between the seasonal height observations.

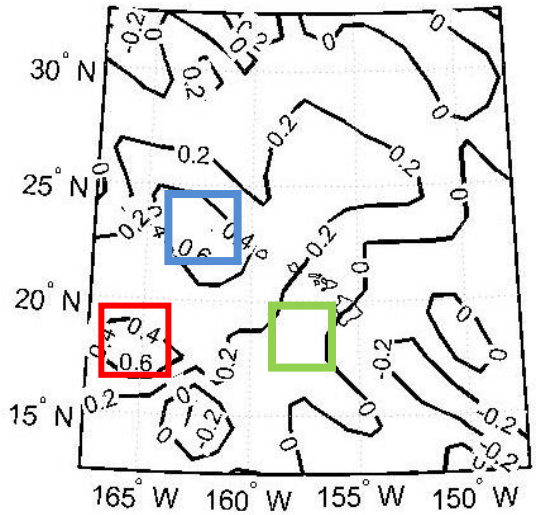

Figure 5.6. Climatology difference (JJA-C minus DJF-C) of GPS RO observed median inversion base height (km). Locations of the analyzed seasonal difference are marked by a red square (17.5˚N, 165˚W), blue square (22.5˚N, 162.5˚W), and green square (20˚N, 157.5˚W).

5.1.2 Trade Wind Climatology Difference

When the low level flow is restricted to northeasterly (trade wind), results for the western two analysis points are similar; however significance test results for the point in the lee of the Big Island are different. Grid box 17.5˚N, 165˚W has 41 total observations between the two seasons yielding a calculated t value (4.13) which is greater than the critical value (2.02) qualifying the difference as significant at a 95% confidence level. Grid point 22.5˚N, 162.5˚W has 74 total observations and a calculated t value of 5.53. The t value is greater than the critical value of 2.00 which again signifies a significant difference in z_i at a 95% confidence level. The 47 total observations in the wake grid point (20˚N, 157.5˚W) had a z_i difference of 0.3 km. The calculated results from the significance test return a t value of 2.99 which is greater than the critical value of 2.00, verifying the difference as statistically significant at a 95% confidence interval.

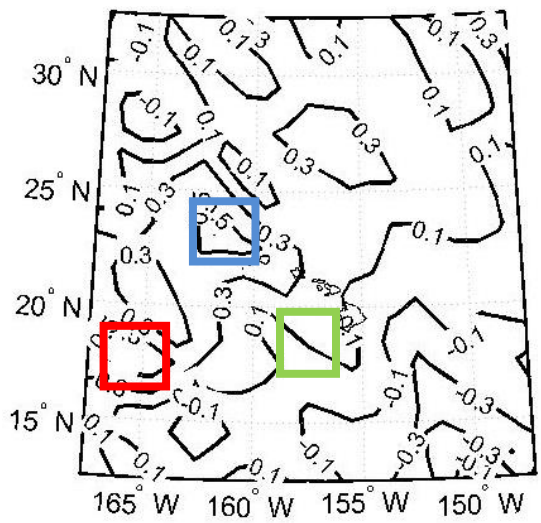

Figure 5.7. Trade wind climatology difference (JJA-TW minus DJF-TW) of GPS RO observed median inversion base height (km). Locations of the analyzed seasonal difference are marked by a red square (17.5˚N, 165˚W), blue square (22.5˚N, 162.5˚W), and green square (20˚N, 157.5˚W).

5.2 JJA Inversion Base Height (z_i) in the Wake

GPS RO observations of the high median z_i value in the wake of the islands will now be compared to CMORPH JJA rainfall climatology (2004-2012) as well as 2007-2012 climatology data from the WRF-ARW 6 km high resolution model. If actual differences exist, then verification from other measured or estimated variables should show the difference as well. Initially, JJA climatology of the horizontal distribution of precipitable water (PW) from the WRF model will be used. The expectation is that a higher inversion base would allow for higher amounts of precipitable water within the boundary layer. If this is the case, then it could be suggested that an increase in JJA precipitation may be the result of the higher inversion base. Finally, vertical transects will be presented over the analysis region (Figures 5.2 and 5.3) in order to determine the high resolution model's ability to reflect values of relative humidity and vertical motion in the areas of high median z_i values observed by GPS RO.

5.2.1 Precipitable Water

Climatology of z_i during JJA 2007-2012 shows a slight increase of inversion height from 1.8 km to 1.9 km in the lee of the island chain (Figure 5.2). Over the same temporal scale, measurements of precipitable water from the WRF-ARW high resolution model

also reflect a modest increase of 1 mm downwind of the islands (Figure 5.8).

In a study of heavy rain events over the south facing slopes of Hawaii, Kodama and Barnes (1997) used the following equation to calculate precipitable water (*PW*):

$$PW \cong \frac{1}{\rho_w g} \int w(p)dp \qquad \text{(Eq. 5.1)}$$

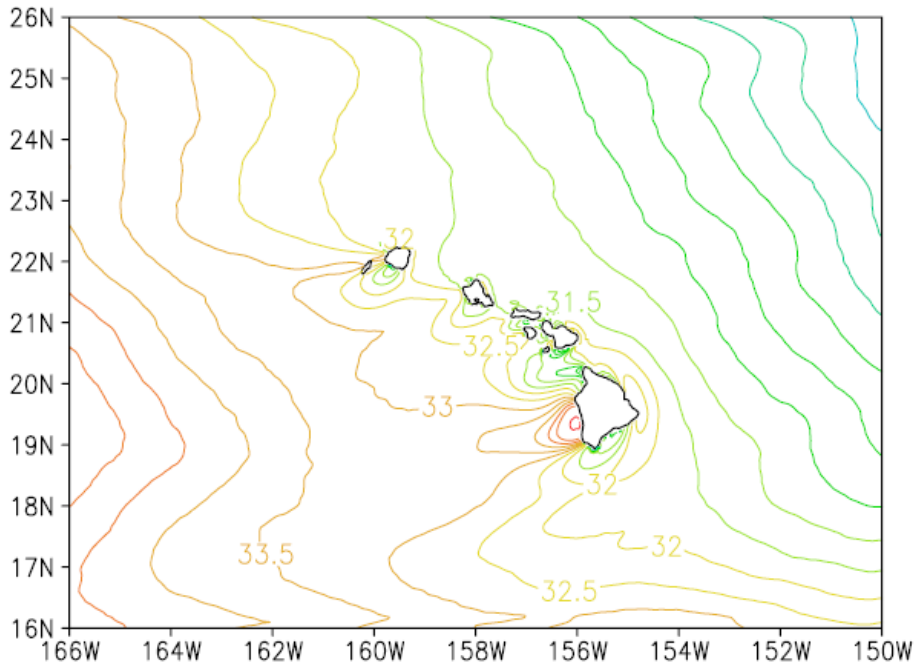

Figure 5.8. Total precipitable water (mm) for JJA 2007-2012 from WRF-ARW 6 km. *Courtesy of David Hitzl.

where ρ_w is the density of liquid water (1,000 kg m^{-3}), g is acceleration due to gravity (9.8 m s^{2}), *w(p)* represents mixing ratio (g kg^{-1}), and p is pressure (Pa). Along with the hydrostatic equation:

$$\frac{dp}{dz} = -\rho g \qquad \text{(Eq. 5.2)}$$

an estimation relating an increase in z_i to an increase in *PW* can be performed. Solving the hydrostatic equation to relate a change in pressure to a change in height, where p is pressure in (Pa), height (z = 100 m), density (ρ = 1 kg m^{-3}), gravity (g = 9.8 m s^{-2}); a 100 m change in height corresponds to a change in pressure of approximately 10 hPa (10^{2} Pa). Using the calculated change in pressure and assuming a mixing ratio of ~10 (g kg^{-1}), scale analysis reveals that an approximate change of 100 m in height within the moist

lower troposphere could yield an increase of 1 mm of precipitable water, which is the approximate increase in *PW* values increase from 32 mm on the leeward coast of the islands to the large area encompassed by the 33 mm isopleth in Figure 5.8.

Figure 5.9 shows the DJF precipitable water gradient increasing from northeast to southwest in a manner more uniform than that represented during JJA. Unlike summer, the relative maximum in the wake of the islands is less pronounced, however the 29.5 mm isopleth is displaced northward between the islands of Kauai and Oahu.

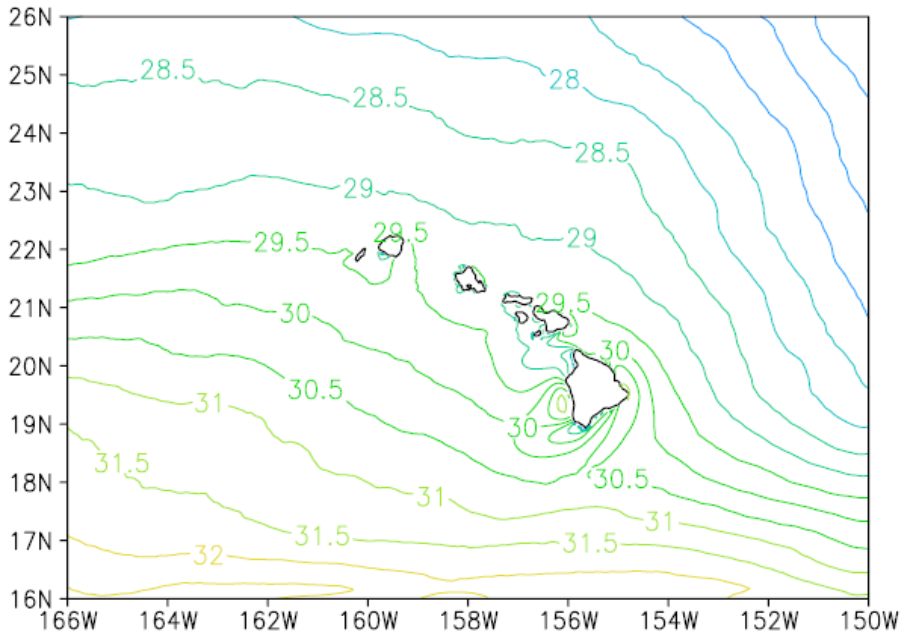

Figure 5.9. Total precipitable water (mm) for DJF 2007-2012 from WRF-ARW 6 km. *Courtesy of David Hitzl.

5.2.2 CMORPH

A higher z_i can also contribute to an increase in precipitation (Chen et al. 1995). However, measurements of precipitation over the open ocean are subject to the same limitations as vertical profile measurements. In this case, a precipitation climatology is available using the CMORPH technique, which provides satellite estimated average rainfall over the region 18˚N-23˚N, 153˚W-162˚W for JJA 2004-2012 (Figure 5.10). Precipitation estimates from CMORPH are primarily used over the open ocean where upwelling radiation from a homogeneous ocean surface can be accounted for (Joyce et al. 2004). The CMORPH climatology (2004-2012) shows a large area of a modest increase (10 - 20 mm) in average JJA precipitation west of 157˚W. The area of increased precipitation is similar to the leeward increase in inversion base height. The higher resolution of the CMORPH data (0.25˚x0.25˚) compared to that of the GPSRO data (2.5˚x2.5˚) could be a factor which contribute to the difference in the horizontal distribution of rainfall versus inversion base height.

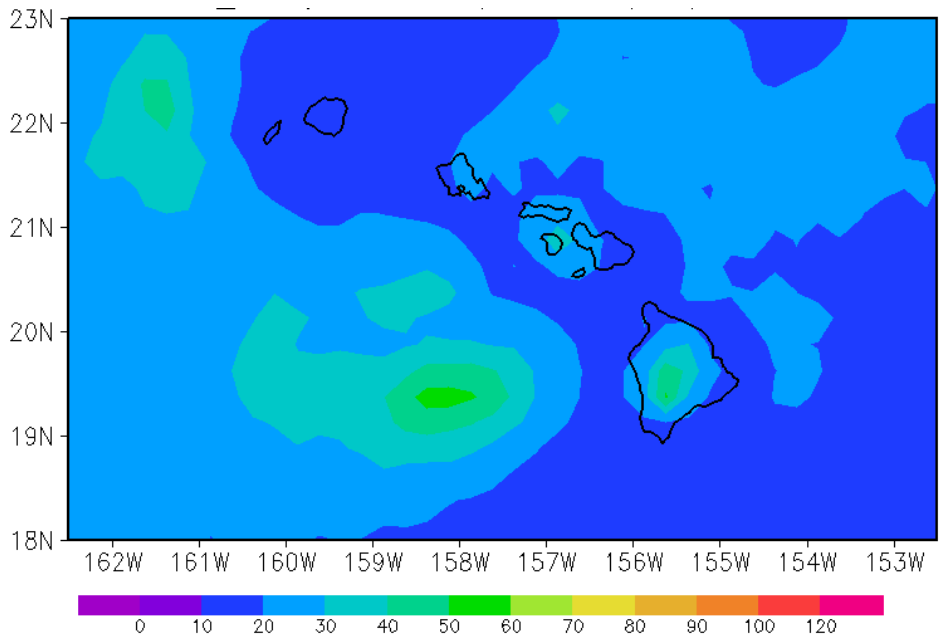

Figure 5.10. CMORPH rainfall climatology (mm) for JJA 2004-2012 (0.25˚). *Courtesy of Yu-Feng Huang.

5.2.3 WRF-ARW – 6 km

Vertical cross sections along the 159˚W longitude transect provide a different view of z_i. The 6 km WRF model from the University of Hawaii show the vertical distribution between latitudes 17˚N - 25˚N. The vertical transects utilizing WRF data for JJA and DJF 2007-2012 show values of relative humidity (%), vertical velocity (cm s^{-1}) and wind speed (m s^{-1}). For the case of JJA climatology, the highest observed median z_i is 2.0 km and located in the area 19˚N-22˚N along the 159˚W meridian denoted by the dot-dashed line in Figure 5.2. An increase can be seen in the vicinity of the highest median z_i values. The vertical plot of relative humidity (Figure 5.11) shows an increase in RH values from 18˚N through 21.5˚N. The 70% isohume increases in height from the 875 hPa pressure level to the 825 hPa level between 19˚N and 21˚N, it then spikes close to 825 hPa at 21.5˚N and finally descends to a level of 850 hPa at 22˚N. The 75% isohume behaves in a similar fashion.

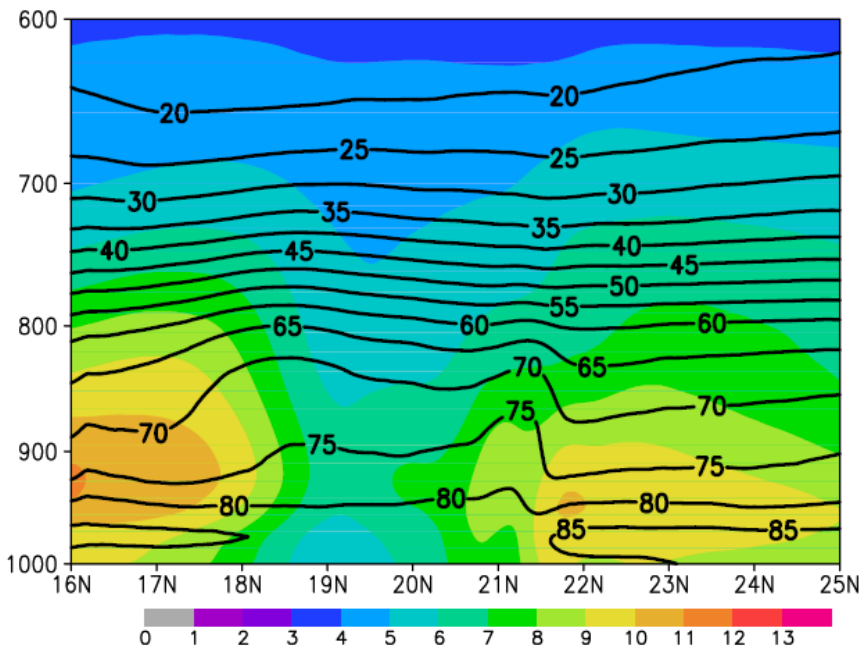

Figure 5.11. JJA-C 2007-2012 6 km WRF-ARW vertical transect along 159˚W (black dash-dot line in Figure 5.2) of relative humidity (black contour in %) and wind speed (filled background contours m s^{-1}). *Courtesy of David Hitzl.

A vertical transect of relative humidity along the same line of longitude is seen in Figure 5.12 for DJF. Unlike the summer months, the isohumes are relatively uniform across the 159 degree transect with the only noticeable increase occurring between 18˚N to 20˚N. In this area, isohumes increase in height by approximately 10-25 hPa, however this is only apparent in the isohume closest to the surface. The rest of the field decreases uniformly with height. This area of increase corresponds to the area of high median z_i seen in Figure 5.3.

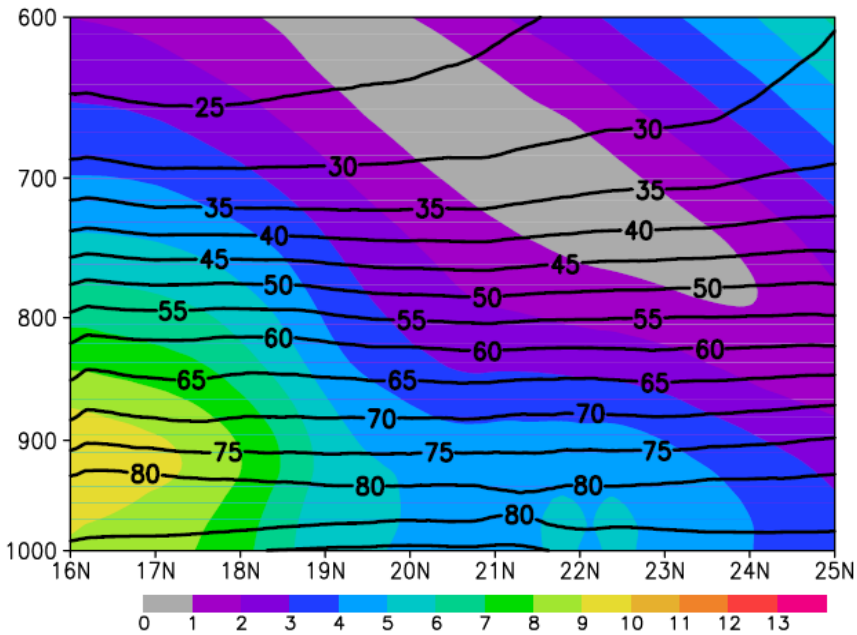

Figure 5.12. Same as Figure 5.11 but for DJF-C 2007-2012 (black dash-dot line in Figure 5.3). *Courtesy of David Hitzl.

Model data of vertical motion along the 159˚ transect (Figure 5.13), show areas of negative (sinking) vertical motion along 18˚N-21˚N. The sinking motion surrounds an area of positive (rising) vertical motion between 20.5˚N -22.5˚N which coincides with the area of low level increase in relative humidity. The increased vertical motion in this area suggests greater convective mixing which could be the driver for a higher inversion base due to the energy exchange between the moist layer and the free atmosphere (Riehl and Malkus 1951; Malkus 1958; Riehl and Simpson 1979). During DJF (Figure 5.14), the 159 degree transect is dominated by sinking motion with the only areas of positive motion located at 21˚N to 23˚N which coincides with the slight increase of relative humidity values near the surface in the same area.

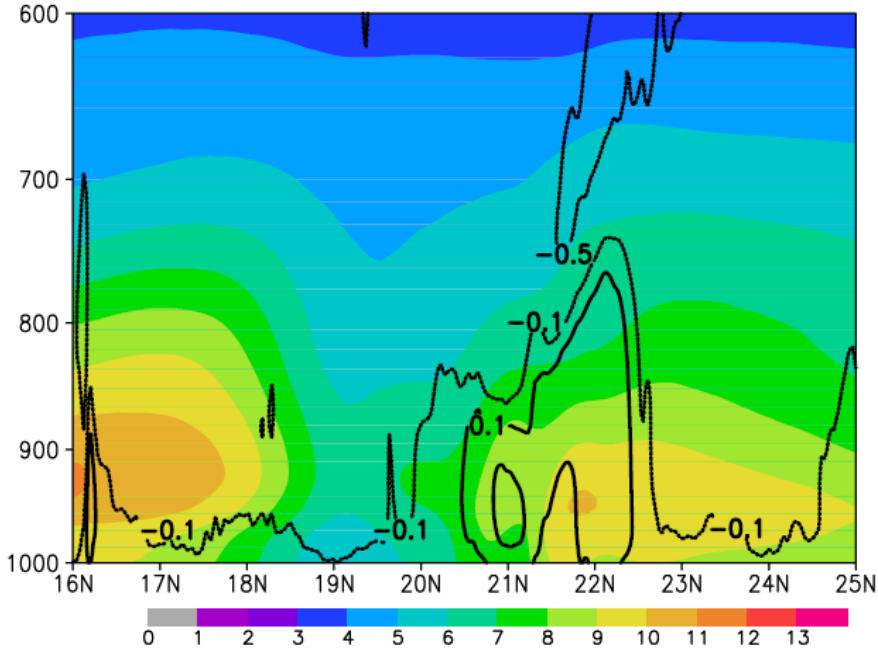

Figure 5.13. JJA-C 2007-2012, 6 km WRF-ARW vertical transect along 159˚W (black dash-dot line in Figure 5.2) of vertical motion (black contour in cm s^{-1}) with rising motion > 0 and sinking motion < 0, and wind speed (filled background contours m s^{-1}). *Courtesy of David Hitzl.

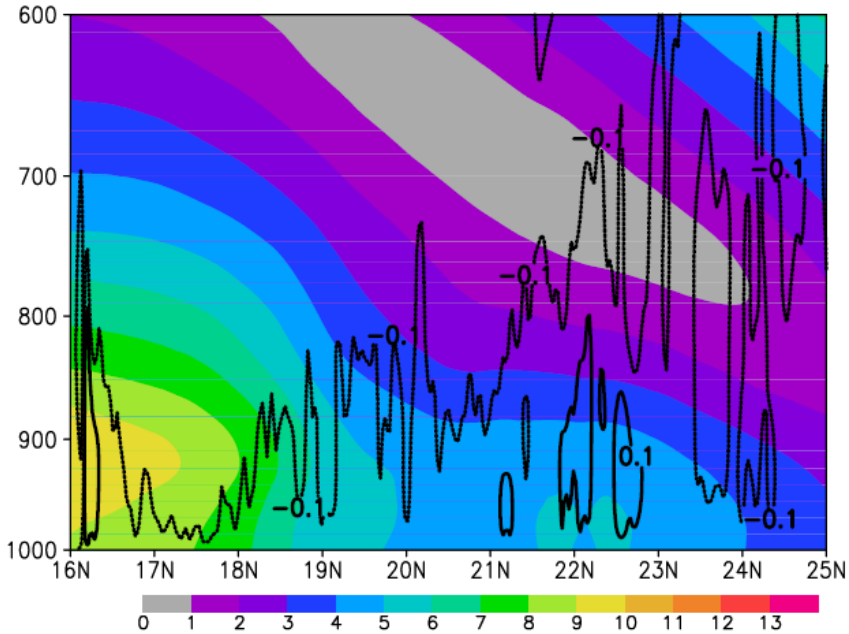

Figure 5.14. Same as Figure 5.13 but for DJF-C 2007-2012 (black dash-dot line in Figure 5.3). *Courtesy of David Hitzl.

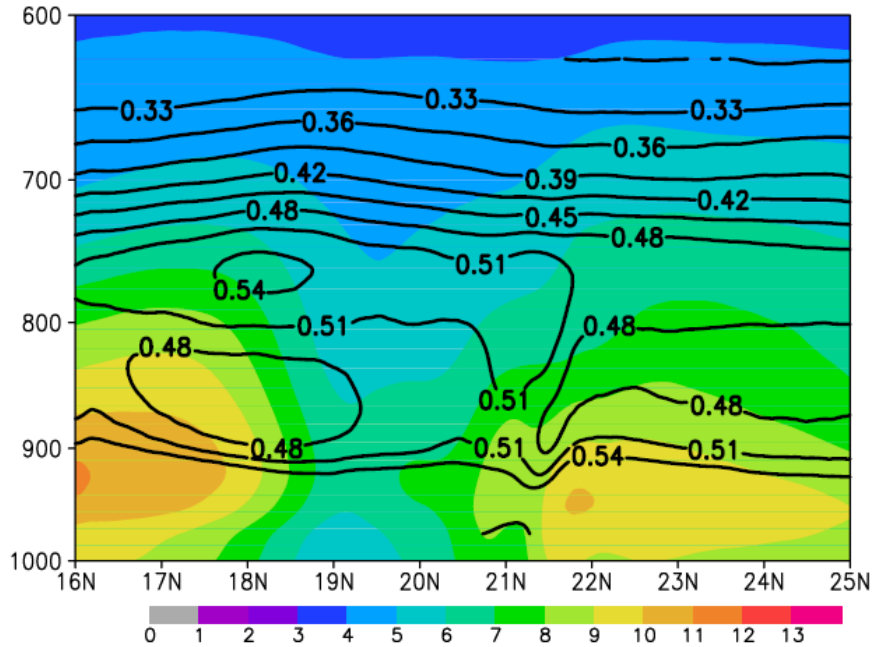

Figure 5.15. JJA-C 2007-2012, 6 km WRF-ARW vertical transect along 159˚W (black dash-dot line in Figure 5.2) of dN/dp (black contour in N-units hPa^{-1}) and wind speed (filled background contours m s^{-1}). *Courtesy of David Hitzl.

The vertical gradient of refractivity with respect to pressure is used to identify the inversion base along the 159˚W transect using the WRF model. The vertical gradient is calculated in this manner due to the nature of the WRF generated data. Units are N-units hPa^{-1} and the maximum value should identify the inversion base. For JJA-C (Figure 5.15), the maximum value is 0.54 N-units hPa^{-1} which appears along the 900 hPa level and in a small area near the 750 hPa level, at 18˚N. While the small pocket of maximum value is too high to represent climatology of the inversion base height, the max value at 900 hPa is too low. However, the maximum value isopleth along the 900 hPa pressure level behaves in a similar fashion as the inversion base would. Beginning at 25˚N and moving south, the height of the isopleth increases as it approaches the islands. In this case, the point between Oahu and Kauai (21˚N-22˚N) is an area of localized maximum low level flow. The isopleth decreases in altitude until it reaches the other side of the Ka'ie'ie Waho Channel (Juvik 1998) causing a local area of convergence due to the rapidly decreasing speed of the low level flow. The height of the isopleth gradually decreases, descending to a minimum at the 910 hPa pressure level at 19˚N and then begins increasing in height to approximately 890 hPa at 16˚N which corresponds to the area of high median z_i observed by the GPS RO technique.

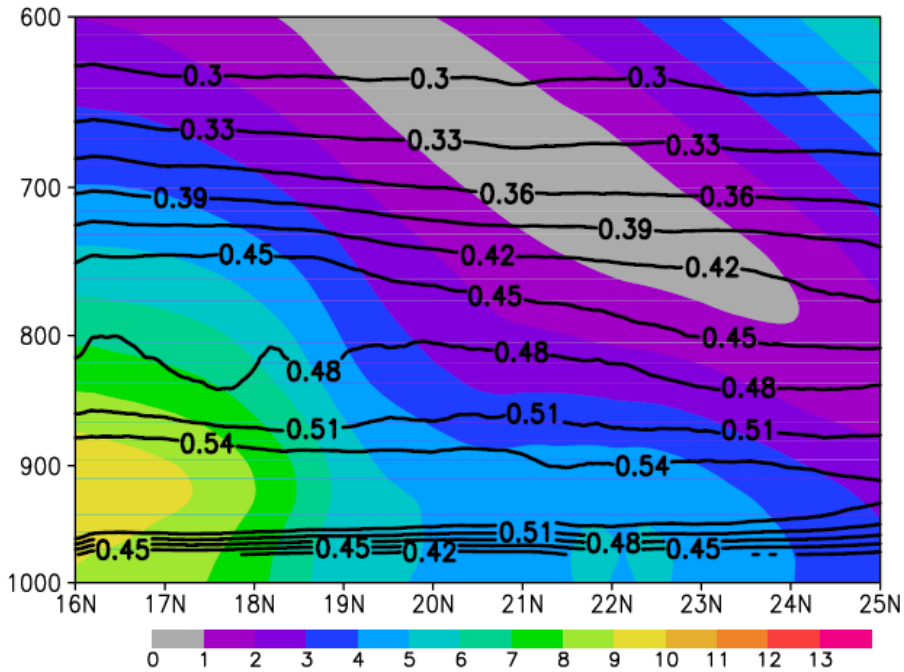

Figure 5.16. Same as Figure 5.15, but for DJF-C 2007-2012 (black dash-dot line in Figure 5.3). *Courtesy of David Hitzl.

For DJF climatology (Figure 5.16), the 0.54 isopleth again represents the maximum value of the gradient, which appears twice. In this instance, the upper line is that which mimics the inversion base. There is little to no apparent interaction as the low level flow passes through the Ka'ie'ie Waho Channel which is due to the easterly direction from which the surface flow originates during the DJF season. Then, moving south from 21˚N, the maximum value isopleth begins increase in height to a pressure level of approximately 875 hPa at 16˚N.

A diagonal transect from the windward to leeward side of the islands, through the Alenuihāhā Channel (black dotted line in Figures 5.2 and 5.3) shows the rapid decrease of relative humidity with height representing the base of the inversion and beginning of the dry layer near the 825 hPa pressure level (Figure 5.17). The inversion base increases as a result of forced ascent as low-level wind speed rapidly decreases upon exiting the channel. The resulting rising motion (0.5-1 cm s^{-1}) can be seen east of 156˚W and west of 157˚W which represent rising motion induced by the island blocking effect (156˚W) and surface convergence as wind speed decreases when exiting the Alenuihāhā Channel (157˚W) (Figure 5.18). It should also be noted that, in addition to the low level

convergence due to the rapidly decreasing wind speed in the exit region of the channel, a thermal effect takes place as well. From the late morning through early afternoon, the sun heats the island surface and low level flow carries the warm air from the islands downstream. As this happens, convergence increases, and cloud lines form during the afternoon in the lee of the islands (Yang et al. 2008a; Yang et al. 2008b). These cloud lines, however, disappear at night which implies that they are not created by the low level winds alone.

During DJF, the height increase of the isohumes occurs gradually when compared to the increase during JJA (Figure 5.19). This stems from the absence of vertical motion in the channel exit region which is affected by the decrease in speed and more easterly direction of the surface winds during the winter months. The annual difference in these two components results in the noticeable absence of appreciable upward vertical motion in the channel exit region (Figure 5.20).

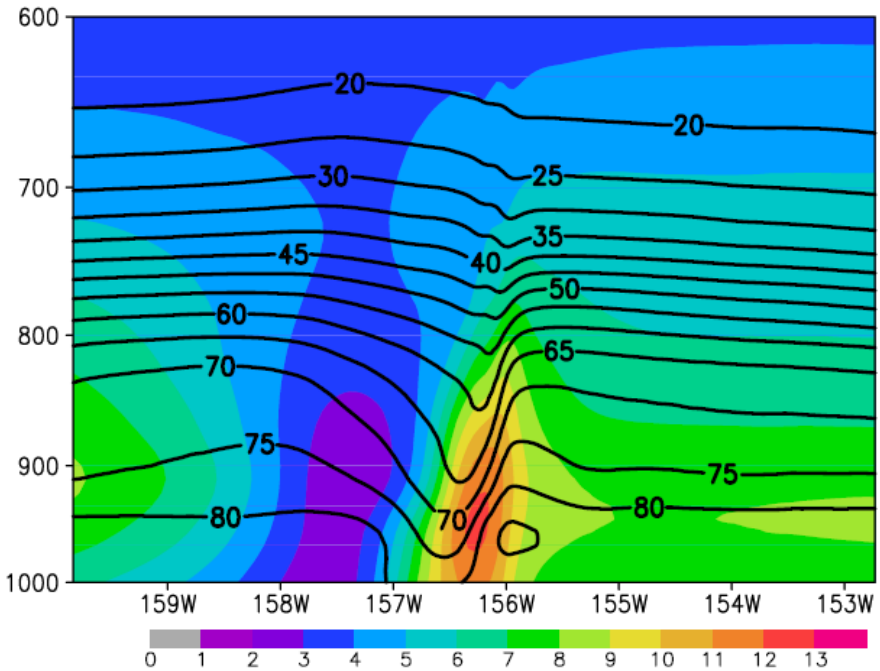

Figure 5.17. JJA-C 2007-2012, vertical cross section along the diagonal 153˚W-159˚W (black dotted line in Figure 5.2) of relative humidity (black contour in %) and wind speed (filled background contours m s^{-1}). *Courtesy of David Hitzl.

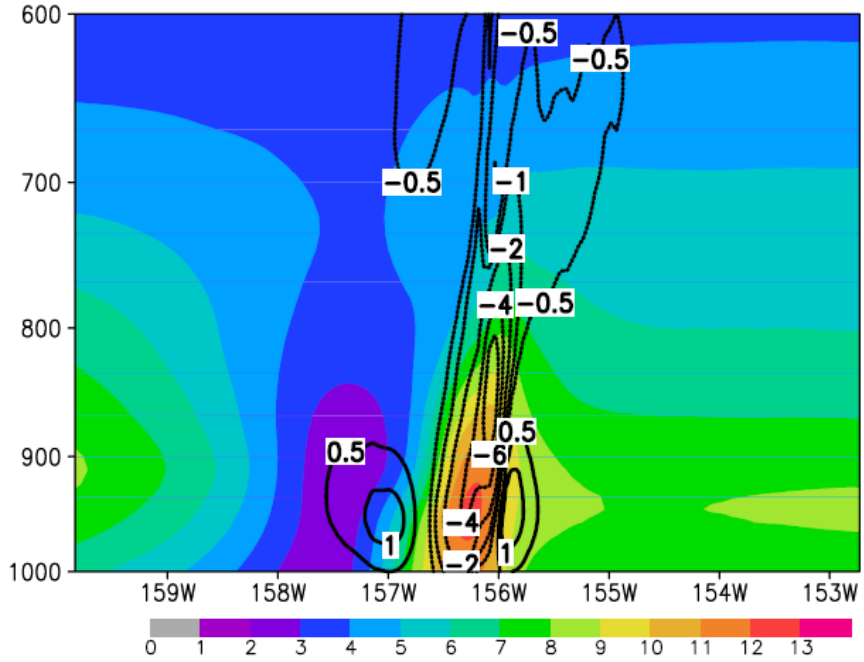

Figure 5.18. JJA-C 2007-2012, vertical cross section along the diagonal 153˚W-159˚W (black dotted line in Figure 5.2) of vertical motion (black contour in cm s^{-1}) with rising motion > 0 and sinking motion < 0, and wind speed (filled background contours m s^{-1}). *Courtesy of David Hitzl.

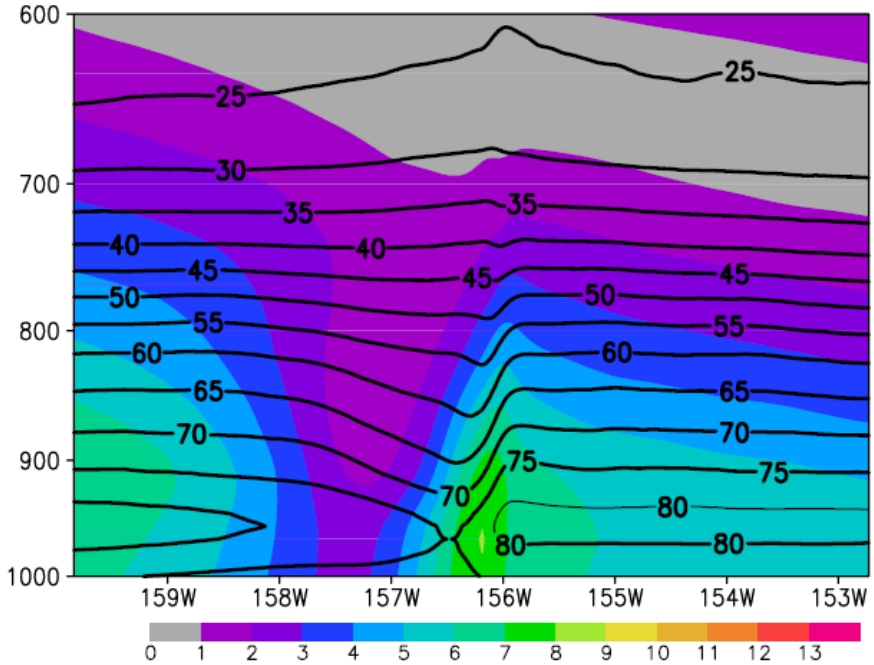

Figure 5.19. Same as Figure 5.17 but for DJF-C 2007-2012 (black dotted line in Figure 5.3). *Courtesy of David Hitzl.

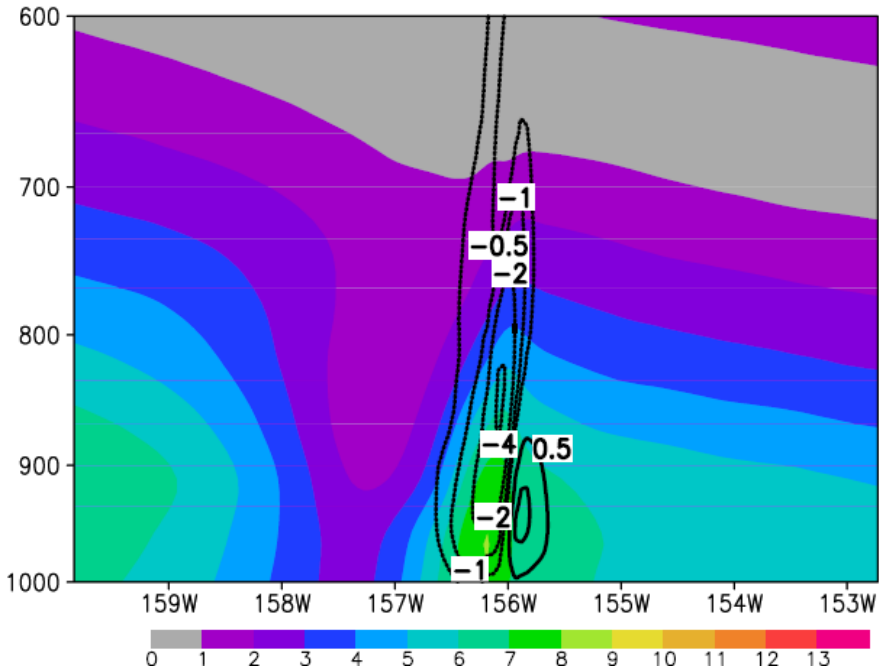

Figure 5.20. Same as Figure 5.18 but for DJF-C 2007-2012 (black dotted line in Figure 5.3). *Courtesy of David Hitzl.

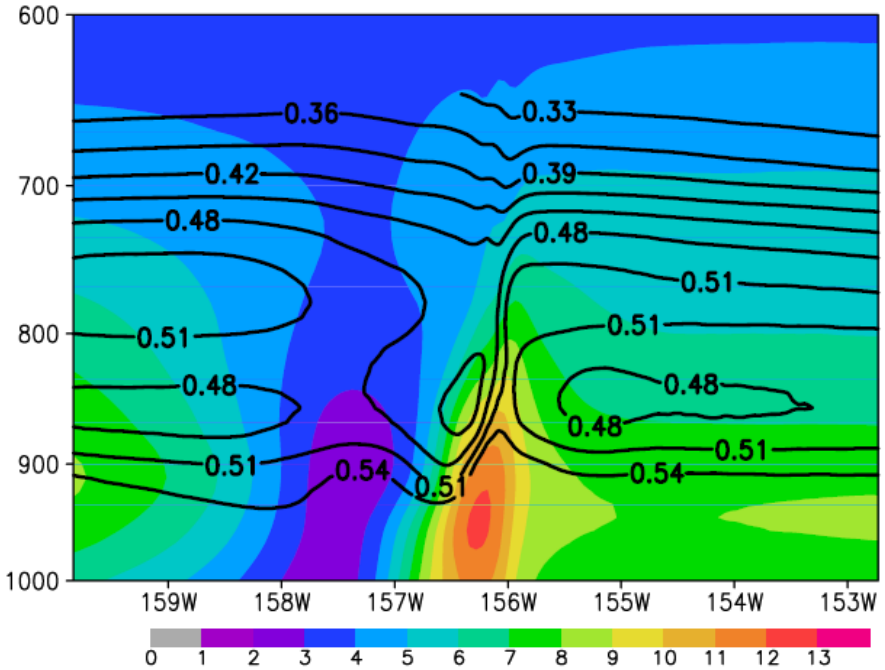

Figure 5.21. JJA-C 2007-2012, vertical cross section along the diagonal 153˚W-159˚W (black dotted line in Figure 5.2) of dN/dp (black contour in N-units hPa^{-1}) and wind speed (filled background contours m s^{-1}). *Courtesy of David Hitzl.

A similar profile of the maximum gradient is seen along the diagonal transect from the windward to the leeward side of the islands (Figure 5.21). Beginning at 153˚W, the 0.54 isopleth is approximately at the 900 hPa level and increases in height to ~ 875 hPa as it encounters the windward side of the island. While passing through the Alenuihāhā Channel, between 156˚W and 157˚W, the height of the maximum isopleth decreases to the 925 hPa level and then increases upon exiting the channel to a level between 900 and 850 hPa between 157˚W and 158˚W. The height of the isopleth decreases to the 925 hPa level at 159˚W and then begins to increase in altitude to the end of the domain at a value of ~900 hPa at 159˚W.

The maximum gradient isopleth during DJF (0.54 N-units hPa^{-1}) is located along the 900 hPa pressure level on the windward side of the islands and decreases slightly as the low level flow exits the channel at 157˚W (Figure 5.22). It becomes apparent that the upper boundary of the 0.54 isopleth layer increases to the west, much like the inversion does.

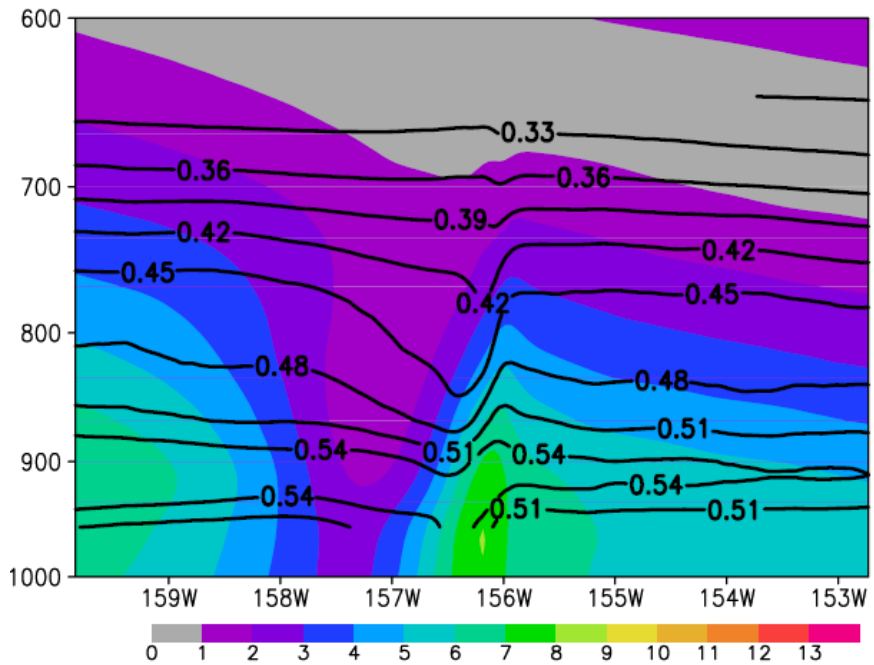

Figure 5.22. Same as Figure 5.21 but for DJF-C 2007-2012 (black dotted line in Figure 5.2). *Courtesy of David Hitzl.

A horizontal view of climatology values for surface wind speed, direction, and surface pressure for JJA (Figure 5.23) and DJF (Figure 5.24) from the WRF model show the differences between the two seasons. Notable in the comparison between the two images is the direction of the surface wind from JJA to DJF which can be attributed to the mean location of the NPSTH. During the summer season, the central area of high pressure is located to the north of the islands as discussed in Chapter 2 (Figure 2.1). The position of the high pressure center leads to surface flow which is more northeasterly during JJA. In contrast, during DJF, the central area of high pressure is centered to the northeast of the islands (Figure 2.3). The difference in location compared to JJA results in surface flow which has more of an easterly component. The direction from which the surface flow approaches the islands as well as the wind speed are both factors of the extent to which the surface winds interact with the island chain. Take, for example, the wind speed difference in the exit region of the Alenuihāhā Channel. The decrease in wind speed and the easterly approach during DJF are both reasons the vertical motion is much less in the exit region. During both seasons, the island blocking effect will lead to increased ascent on the windward side of the islands. However, the increased wind speed in the channel is much greater during JJA than DJF due to the southwest to northeast orientation of the channel and its alignment with the low level flow. The rapid decrease in wind speed upon exiting the channel leads to surface convergence and rising motion in the exit region which occurs at a much greater magnitude during JJA as opposed to DJF. However, the increase in vertical motion and its effect on the height of the inversion base is on too small a scale to be resolved by GPS RO data. Regardless of the magnitude of rising motion, surface convergence in the exit region exists during both seasons. The relative location of the highest median z_i values suggest the reason for the island wake effect in terms of the inversion base height may be related to the prevailing direction of the low level winds and their interaction with the islands.

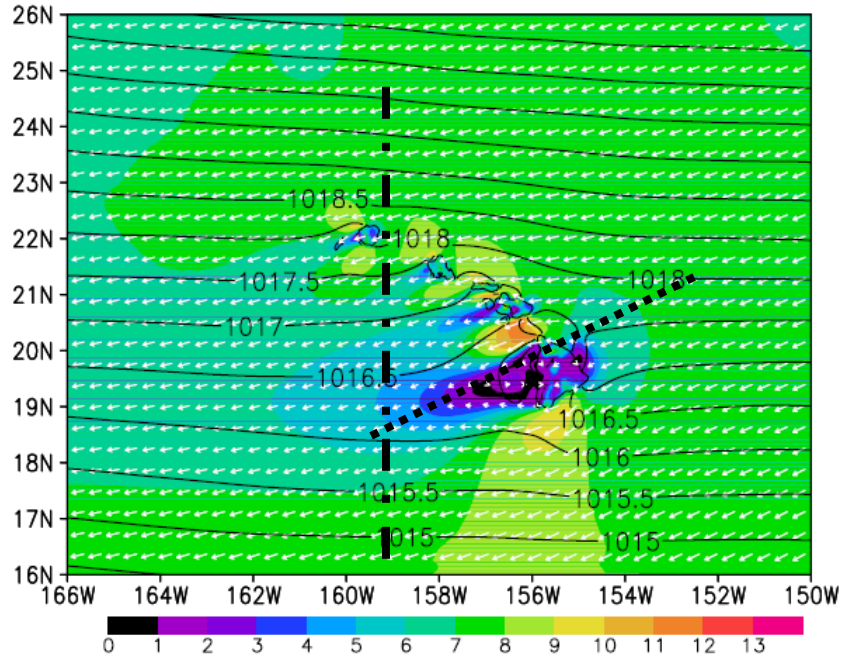

Figure 5.23. Horizontal view of 6km WRF showing wind vectors, wind speed (color fill in m s^{-1}), vertical motion (cm s^{-1}) for JJA-C 2007-2012. . Black dash-dot line is the approximate location of 159˚W longitude transect used for Figures 5.11, 5.13, and 5.15; and black dotted line is the approximate location of 153˚W-159˚W diagonal transect used for Figures 5.17, 5.18, and 5.21. *Courtesy of David Hitzl.

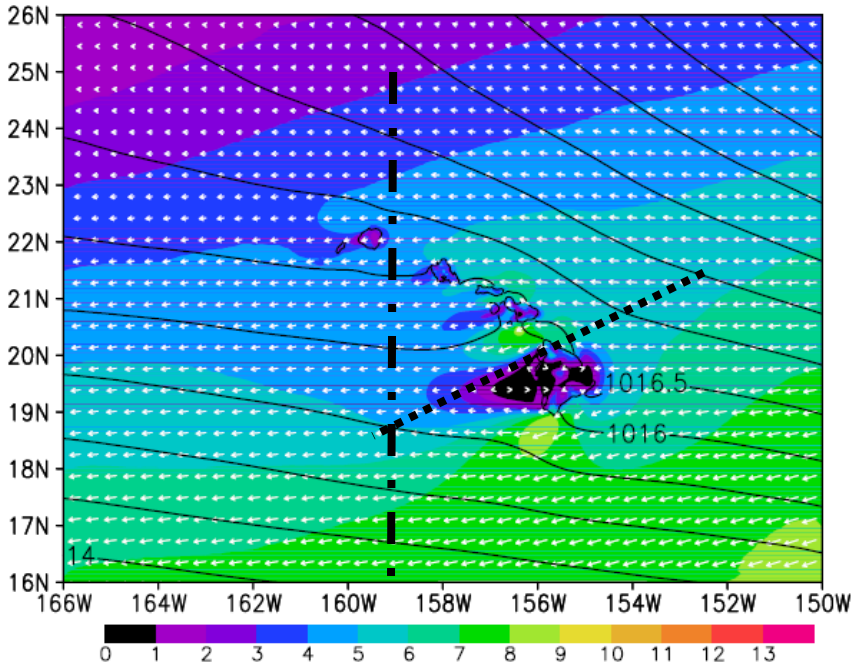

Figure 5.24. Same as Figure 5.23 but for DJF-C 2007-2012. Black dash-dot line is the approximate location of 159˚W longitude transect used for Figures 5.12, 5.14, and 5.16; and black dotted line is the approximate location of 153˚W-159˚W diagonal transect used for Figures 5.19, 5.20, and 5.22. *Courtesy of David Hitzl.

Chapter 6: Summary and Conclusion

6.1. Summary

Atmospheric vertical profiles over land based stations have been commonplace since the 1930's. Over the open ocean, this technique has been limited to ship borne field projects in specific areas which left a vast part of Earth's lower atmosphere unsampled. The evolution of GPS RO has brought a new opportunity to observe vertical atmospheric refractivity over remote locations. Beginning with the Mariner IV and V missions to measure the atmosphere of Mars and Venus respectively, to the present day COSMIC Constellation which measures Earth's atmosphere, radio occultation provides an avenue to remotely obtain vertical atmospheric profiles over sparsely populated regions.

Six years (2007-2012) of GPS RO observations were analyzed in order to determine median values for inversion base height, as well as provide a proxy for strength, over the central North Pacific Ocean. Observations of z_i measured via GPS RO were compared to previous analyses that were based on five years (1999-2004) of radiosondes launched at 0000 and 1200 UTC from Hilo and Lihu'e (Bingaman 2005). The results of this comparison carry along with them the caveat of horizontal resolution differences. While radiosonde and GPS RO z_i observations compare favorably, the comparison is between a point (radiosonde) and an area (GPS RO). While GPS RO features a high vertical resolution (~100 m), the observation can vary by approximately 100 km on a horizontal scale from the top of the atmosphere to the surface (Anthes et al. 2000). The intent of this analysis was to demonstrate the ability of GPS RO to accurately detect and observe the horizontal distribution and variability of the inversion base over the Hawaiian Islands. The information gained could help illustrate island-atmosphere interactions, aide in rainfall prediction, increase the accuracy of NWP by including an observed z_i versus a parameterization, and add additional insight to island wake circulations.

Climatology of the inversion base reveals a high median value of ~2.0 km during JJA in the lee of the islands. If the low level flow is restricted to trade-winds only, the maximum median value increases to 2.1 km over the same area. During DJF, a high

median z_i value of 1.8 km is located to the southeast of the Big Island. This DJF median increases to 1.9 km when the low level flow is restricted to trade-wind flow. The inversion, when present, is strongest during DJF, due to the closer proximity of the NPSTH to the islands. The result is a lower z_i during the winter months. The comparison between radiosonde and GPS RO observed inversion base revealed a difference of 200 – 300 m during JJA and DJF over Hilo. This is attributed to the local circulation effects of the Big Island. Over Lihu'e, observations for JJA and DJF were within 100 meters of radiosonde observations.

A diurnal comparison of the horizontal distribution during the summer months was also performed in order to identify the diurnal variation of z_i. Observations for JJA-Day were classified as those which occurred between 1200-1800 HST while observations for JJA-Night were restricted to 0000-0600 HST. The observed z_i median was higher during JJA-Night (~2.0 km) than observed during JJA-Day (~1.9 km). When compared to Grindinger (1992), the difference between radiosonde and GPS RO was 200 – 300 m over Hilo, while the difference over Lihu'e was 100-200 m.

The analysis period involved a moderate El Niño (2010) event as well as a moderate to strong La Niña event (2011). During the 2010 El Niño, a median value of 1.8 km which encompassed a large area over the entire island chain was observed. The 1.8 km isopleth existed over the same area during the following year's La Niña event, however a maximum of 1.9 was observed in a smaller area in the lee of the islands. The RMG measured inversion strength was between 2.1 and 2.2 for both events. The relatively small number of observations hinders a higher resolution analysis for El Niño (n = 4876) and La Niña (n = 2674).

The most intriguing aspect of this analysis was the maximum median value that appears in the lee of the islands during JJA. The WRF-ARW model was used in order to determine whether a high resolution model would resolve this wake feature. A scale analysis was used to compare increases of z_i to PW. Vertical motion and relative humidity were shown in vertical transects along 159˚W longitude and a southwest to northeast diagonal (153˚W – 159˚W). Evidence of upward vertical motion is seen in both

variables within a similar location (18˚N-21˚N), corresponding to part of the area of GPS RO observed high median z_i values.

The refractivity equation was implemented using WRF model data (P, T, and q) to test whether the calculated refractivity gradient could be used to detect z_i. Detection of the inversion base in this fashion was utilized via the ECMWF model by Ao et al. (2012) and Xie et al. (2012). The high resolution WRF shows attributes of the inversion through relative humidity and vertical motion values and to a lesser extent, through differentiation of N with respect to pressure (dN/dp). The maximum gradient value in both the meridional and windward to leeward vertical transects behave in the same fashion one would expect the inversion base to behave. An increase in height of the maximum gradient occurs in the exit regions of the Ka'ie'ie' Waho Channel (meridional transect) and Alenuihāhā Channel (windward to leeward transect) where rapidly decreasing wind speed causes upward vertical motion due to surface convergence. Additionally, the height of the maximum gradient increases to the south and southwest in the wake of the islands which is the expected reaction approaching the ITCZ. The caveat to the proposed detection of the inversion in this manner however, is the height of the maximum gradient appears too low. During JJA, the height difference is on the order of 500 m lower than that detected by the GPS RO method. The height difference during DJF is less (200-300 m), but the estimation remains too low in comparison. The reason behind this could be attributed to the method of calculation of the gradient and the difference in vertical resolution between the WRF model and GPS RO. The vertical refractivity gradient was calculated using the finite difference between two points (N_{i+1}- N_{i-1}/z_{i+i}-z_{i-1}). Using this technique, WRF model has a total of 38 vertical levels, 12 of which can be found below 3500 m (Hitzl 2013). GPS RO features a vertical resolution of 100 m which results in 35 vertical levels decreasing to 17 levels when considering the nature of the calculation of the vertical gradient. The additional vertical resolution of GPS RO most likely plays a role in the difference of heights between the two. In a similar approximation, Ao et al. (2012) found an average difference between GPS RO refractivity observations and those calculated using data from the ECMWF which has 91 vertical levels, 26 of which are below 3500 m. The total number of levels is reduced to 12 in terms of the method of

calculation of the refractivity gradient. Additionally, the refractivity gradient method only takes sharp inversions, $\frac{dN}{dz}$ < -50 N-units·km^{-1} into consideration which occurs in approximately 50% of all observations. The WRF represents the mean of the entire climatology and does not distinguish between the gradient value collected from a profile with a "sharp" inversion and one that was not.

6.2. Conclusion

The initial objective of this project involved the determination of the usefulness of GPS RO observations in order to detect the base of the inversion layer. Observations of the inversion base from GPS RO data accurately depict the structure of the inversion over the analysis region. Refractivity values and calculated RMG values both show the inversion is lowest and strongest adjacent to the California coast. Moving south and west, the inversion base height increases and strength decreases as previously noted (Malkus 1958). Additionally, refractivity values reveal a lower and stronger inversion during the winter months in conjunction with the proximity of the NPSTH to the island chain. The inversion is also lower with a stronger RMG during a moderate El Niño event (2010). Diurnal differences during JJA also show the inversion to be slightly higher at night than during the day.

Over the analysis region, the additional detail provided was the presence of local high median values. During JJA, the highest median z_i value is located in the lee of the islands and appears to be the result of interaction between the islands and low-level flow. A difference between JJA and DJF of 500 m raised the initial question of the statistical significance of the difference. However, comparing both climatology and trade wind climatology, it was shown that the data was normally distributed and z_i differences were significant at a 95% confidence interval. A third point was examined in the lee of the Big Island which had a seasonal difference of 300 m during trade wind flow, which was also verified as significant at the 95% confidence interval.

Can GPS RO data be utilized at a high enough grid resolution in order to examine the various interactions between BL circulations and the Hawaiian Islands? While the initial

idea of grid resolution was not an issue, the fact remains that even when starting with over 30,000 observations for each season, the analysis still has limitations. Once the data observations are pared down from a climatological group to smaller groups such as a single season or smaller grid size, data distribution becomes an issue. The average number of observations per grid box was reduced by approximately two-thirds when the analysis grid was reduced from 5˚x5˚ to 2.5˚x2.5˚. Analyses of ENSO events and diurnal variations left southern points of the analysis region with less than 5 observations per grid box. A positive effect of this is the decrease in areal coverage of the high median values. As the grid size decreases, the high values become more defined. This leads to the next question of, "If these values decrease as the grid resolution increases, then is it possible they would disappear completely at a high enough resolution?" While this is certainly possible, there is no way to test this theory without more data. This is compounded with the fact that, for any given grid box, the observed data could be affected by any number of natural phenomena which would cause the affected grid box to skew values in surrounding grid boxes in a manner not representative of the actual conditions. Another issue with data accuracy is the presence of moisture as the southern part of the region is affected by the convection from the ITCZ. The refractivity technique implemented in this thesis only works when a sharp decrease in moisture exists within the inversion layer. In the case of convection, the "sharp" gradient is washed out and the inversion, even if weak, is not identified in a consistent manner. In this case, the inversion appears to decrease in height south of 15˚N, which is not the case.

6.3. Future Work

In terms of this research, the ideal course of future work would be to sample the area of the inversion maximum with radiosondes. If a cross section over the area of maximum inversion base height could be resolved with radiosonde observations, it would reinforce what is observed from the GPS RO measurements and provide another data set from the same region that could be used in a statistical comparison. If the presence of the high median values were observed, then a more detailed analysis of the subtle changes of the inversion layer could be undertaken. However, at this time, there are only models to make a comparison.

A more practical approach for a similar analysis would be with the use of the WRF model. If it could be determined that the model could consistently represent comparative inversion heights with calculated refractivity values, it would be interesting to perform a comparative analysis of the inversion structure with and without the presence of the Hawaiian Islands to determine the degree to which their interaction with the lower tropospheric flow is a factor in the structure of the inversion layer.

The anticipation of Formosat-7/COSMIC-2, due to launch six more satellites in 2015 and 2018 respectively, could provide over 12,000 occultations per day. With new (and more) data, comes the chance for more detailed analyses. The abundance of observations could allow for a higher spatial resolution analysis, which may allow small scale factors to be resolved. Additional observations, both spatially and temporally, would allow for better sampling of ENSO events and their corresponding effects on the inversion height.

Both avenues of work would help, in part, to make GPS RO a viable option for locating the top of the atmospheric boundary layer. With this in mind, NWP model output could be enhanced by an accurate interpretation of the top of the MBL which could be used for verification, initialization, and improved output (Zhou and Chen 2014).

Appendix 1. GPS RO Observation Case Study

The purpose of this exercise is to provide a better picture of the number of GPS RO observations collected over the region over a given day. For this case study, one day, one week, and one month were chosen from each season (JJA and DJF). Once the time period was chosen, the data were analyzed in the same manner as all other data in this thesis. Initially, all observations that fit the time frame were selected. After, the data was then filtered to include only "sharp" inversions. The qualifying observations were then plotted over the analysis region to show where each occultation occurred; the inversion height was then estimated from the available data.

A.1.1 One Day Observation Period

For the JJA season, 21 July, 2010 was randomly selected as the day used. The initial selection process yielded 83 total observations over the analysis region, of which, 40 observations contained a sharp inversion. In this case, the vast majority of observations exist to the right of a line that bisects the Hawaiian Island chain from northwest to southeast (Figure A.1.1).

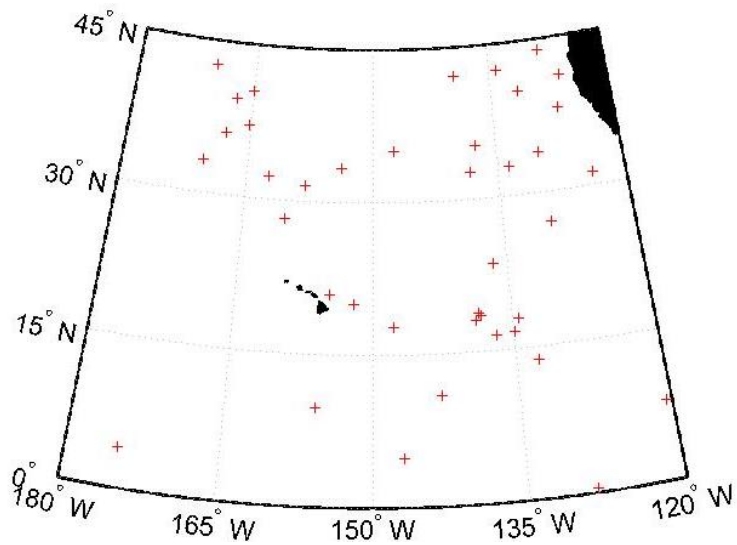

Figure A.1.1. Map of GPS RO analysis region (5˚N-45˚N,120˚W-180˚W). Red crosses show the location (surface coordinates) of each observation occurred during the 24 hour period of 21 July, 2010.

Observations for 21 January, 2010 show a distribution which favors the southwest portion of the analysis region (Figure A.1.2). During this particular day, a total of 77 observations were made while only 28 returned a "sharp" inversion layer. For each occasion, an estimation of inversion base height was not possible because gradient method requires at least two observations per grid box in order to compute $\frac{dN}{dz}$.

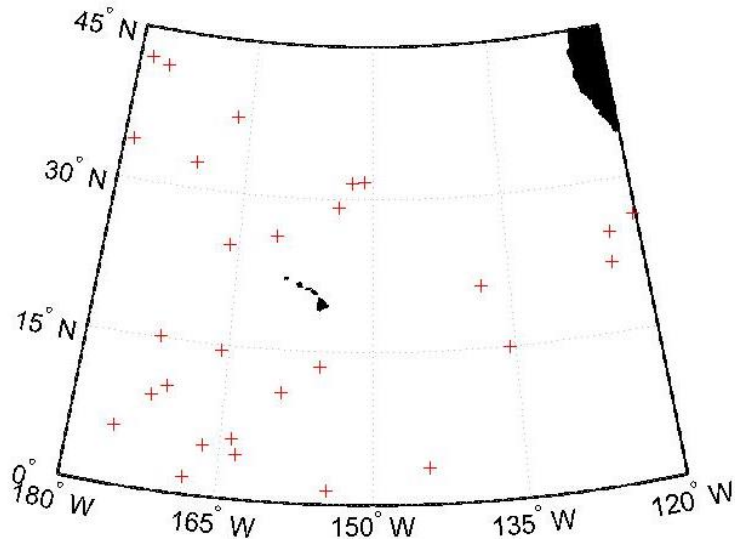

Figure A.1.2. Map of GPS RO analysis region (5˚N-45˚N,120˚W-180˚W). Red crosses show the location (surface coordinates) of each observation which occurred during the 24 hour period of 21 January, 2010.

A.1.2 One Week Observation Period

The week of 4 July, 2010 – 11 July, 2010, 532 observations were recorded, 270 in which a "sharp" inversion was detected (Figure A.1.3). The high median z_i was located at the western edge of the region (2.5 km) with totals over the islands of 2.3 km and an area of 2.4 km to the immediate southwest of Kauai (Figure A.1.4).

During winter, 4 January, 2010 – 11 January, 2010 had a total of 800 observations, 357 of which had a "sharp" inversion (Figure A.1.5). High median z_i values were sporadically located over the islands with median values ranging from 1.7 over the Big Island to 1.5 over Kauai (Figure A.1.6).

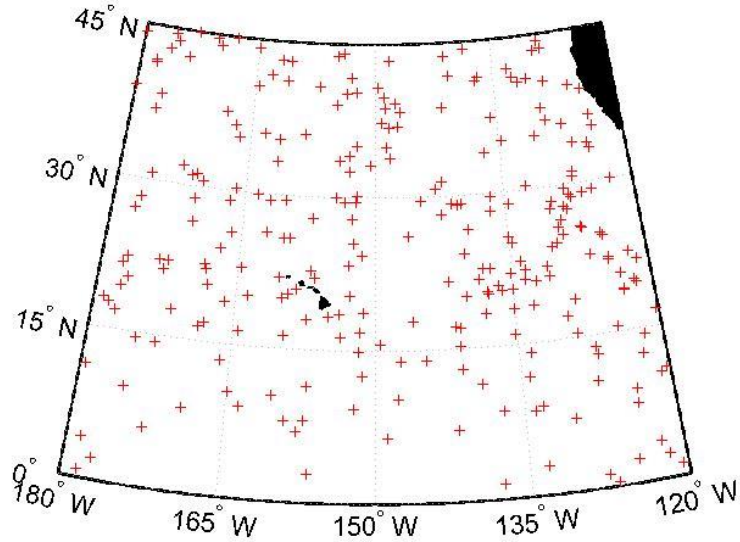

Figure A.1.3. Map of GPS RO analysis region (5˚N-45˚N, 120˚W-180˚W). Red crosses show the location (surface coordinates) of each observation which occurred during the week of 4 July, 2010 – 11 July, 2010.

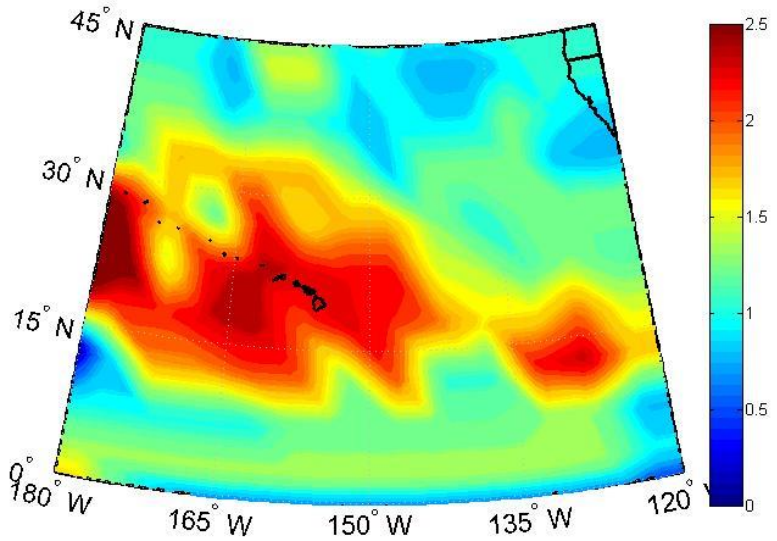

Figure A.1.4. Median z_i over the analysis (5˚N-45˚N, 120˚W-180˚W) during the week of 4 July, 2010 – 11 July, 2010.

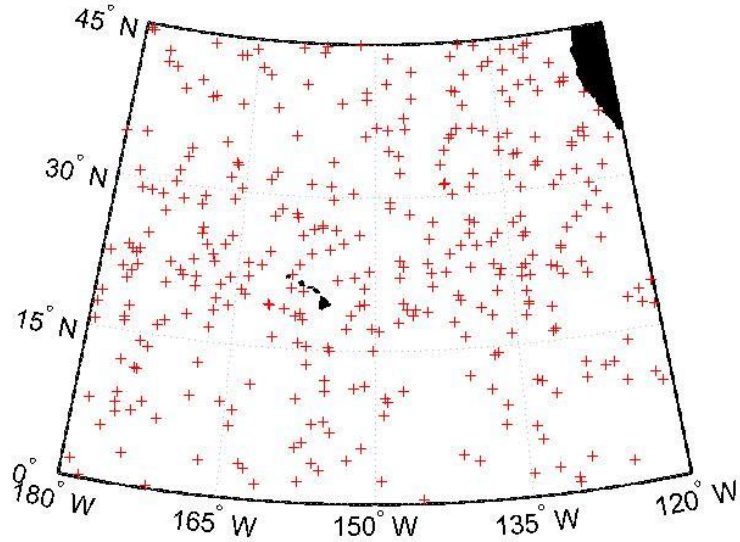

Figure A.1.5. Map of GPS RO analysis region (5˚N-45˚N, 120˚W-180˚W). Red crosses show the location (surface coordinates) of each observation which occurred during the week of 4 January, 2010 – 11 January, 2010.

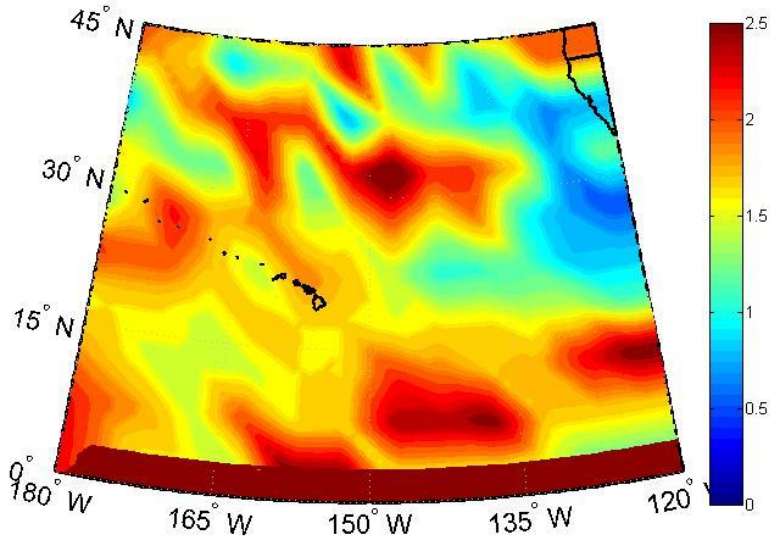

Figure A.1.6. Median z_i over the analysis (5˚N-45˚N, 120˚W-180˚W) during the week of 4 January, 2010 – 11 January, 2010.

A.1.3 One Month Observation Period

The month of July had a total of 2068 observations with 1068 classified as showing a "sharp" inversion (Figure A.1.7). The estimated z_i in during this week can be seen in Figure A.1.8 which shows the lowest inversion base adjacent to the California coast with z_i increasing to the south and west. The highest median value (2.5 km) occurs west of the islands within the grid box 27.5˚N, 177.5˚W. Over the islands, the median z_i ranges from 2.1 km over the Big Island to 2.4 km west of Kauai. Additional high median values occur along the southern extent of the domain within the 2.5˚N set of grid boxes.

The month of January had a total of 2632 observations with 1307 occurrences of a "sharp" inversion (Figure A.1.9). Estimated z_i for the month shows generally lower median values throughout the entire domain. Over the islands, z_i ranges from 1.7 over the Big Island to 1.8 over Kauai (Figure A.1.10).

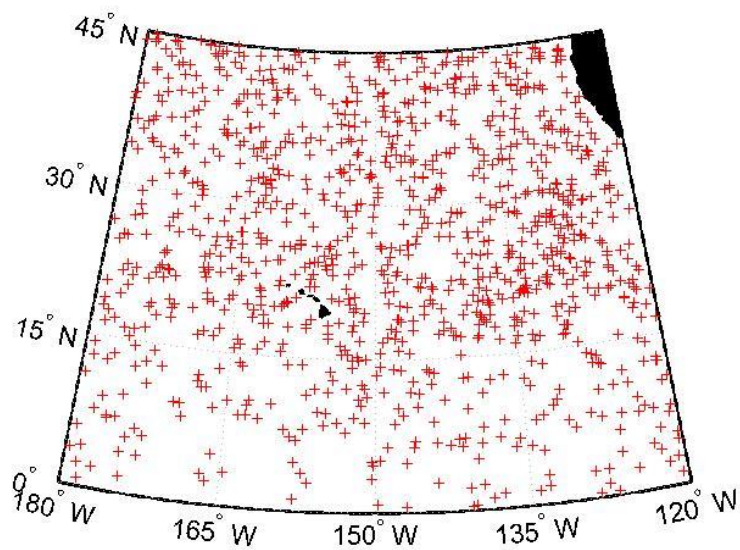

Figure A.1.7. Map of GPS RO analysis region (5˚N-45˚N, 120˚W-180˚W) during the month of July 2010. Red crosses show the location (surface coordinates) of each observation.

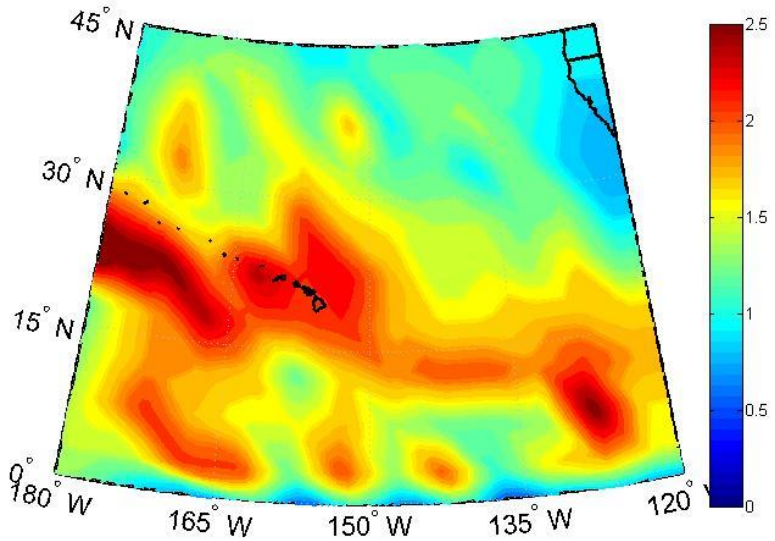

Figure A.1.8. Median z_i over the analysis (5˚N-45˚N, 120˚W-180˚W) during the month of July 2010.

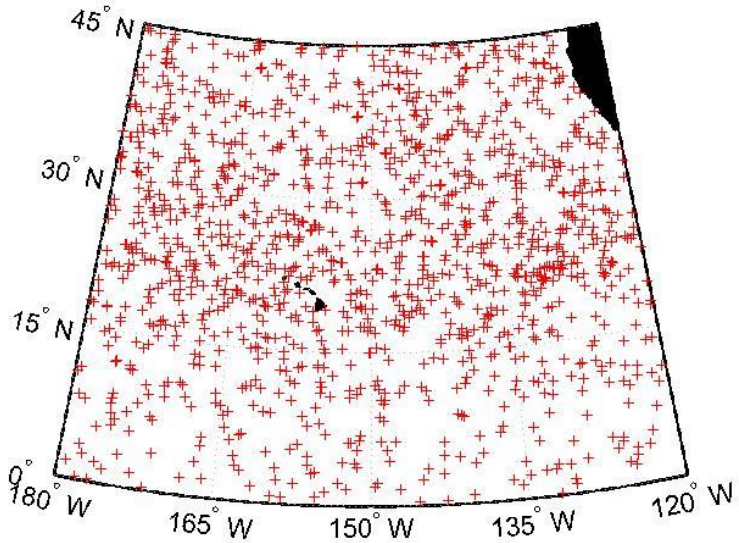

Figure A.1.9. Map of GPS RO analysis region (5˚N-45˚N, 120˚W-180˚W) during the month of January 2010. Red crosses show the location (surface coordinates) of each observation.

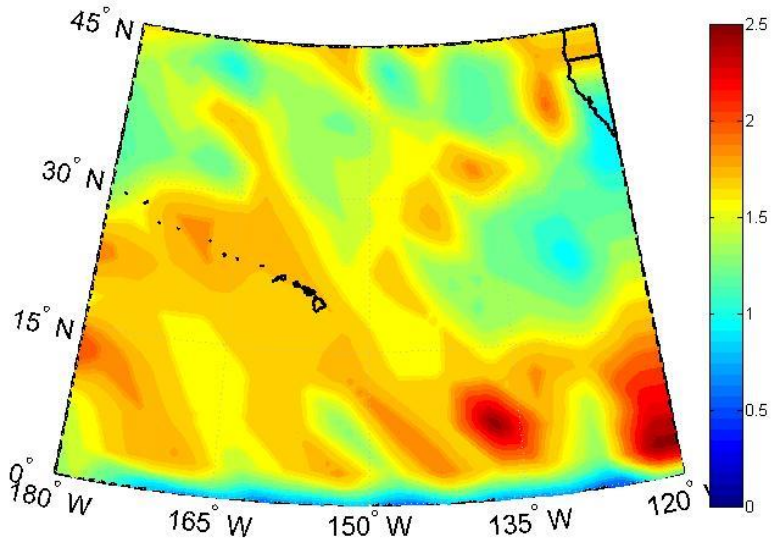

Figure A.1.10. Median z_i over the analysis (5˚N-45˚N, 120˚W-180˚W) during the month of January, 2010.

A.1.4 Observation and Interpolation

This brief case study serves multiple purposes. First, it shows the number of observations that occur over a given period of time. In this case, it showed observations for a day, week, and month for time periods within JJA 2010 and DJF 2010. Additionally, it shows calculated z_i for weekly and monthly observations. It can be seen that values of zi decrease as the number of observations increases from 1 week to 1 month. This result is anticipated as more samples will lead to a better estimate of z_i. More importantly, this case study shows the nature of data interpolation can lead to erroneous values between grid boxes. While the data in each grid box is valid, the nature of evenly spaced grid points can lead to less than valid values between grid boxes. When presenting a horizontal distribution of data, it must be kept in mind that values between grid points are only interpolated values meant to logically transition from one point to another, and the data between points is computer estimated.

Appendix 2: Sample Soundings

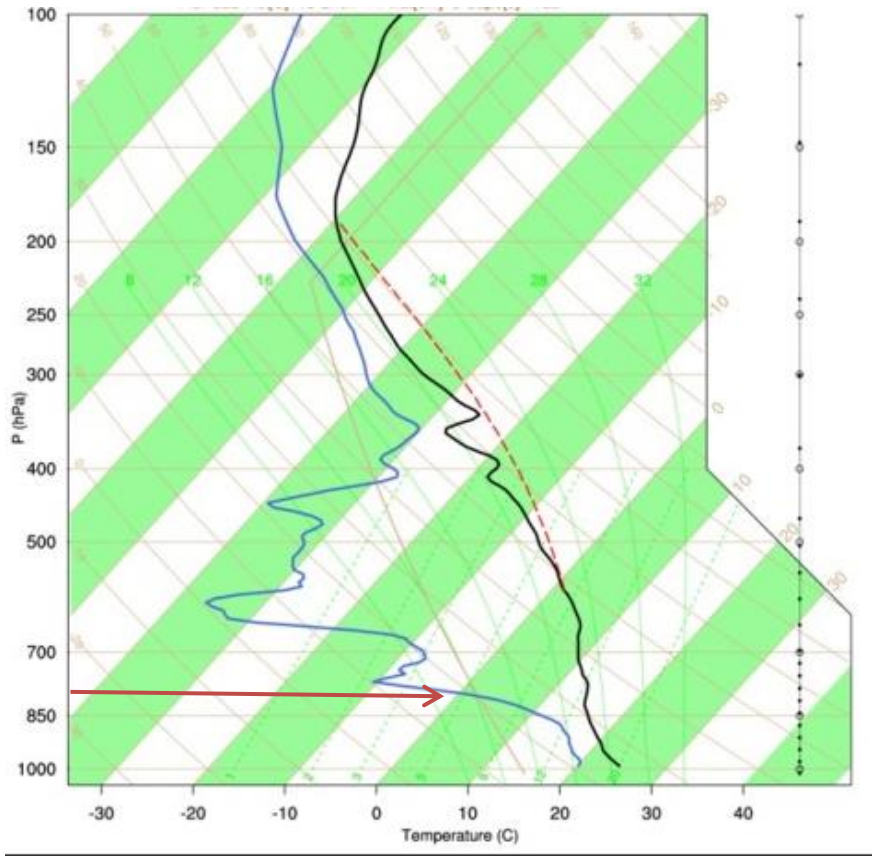

Figure A.2.1. Example sounding from 0820 HST 23 July, 2008. The blue line (left) represents the dewpoint temperature profile. The black line (right) represents the temperature profile. Red arrow illustrates the reference pressure level of minimum refractivity gradient. Location of observation is approximately 17.49˚N – 163.58˚W. Inversion Base is observed at the approximate height of 2.1 km and a corresponding pressure level of 794 hPa. Sounding data was obtained from the Taiwan Analysis Center for COSMIC (http://tacc.cwb.gov.tw/cdaac/ 2014).

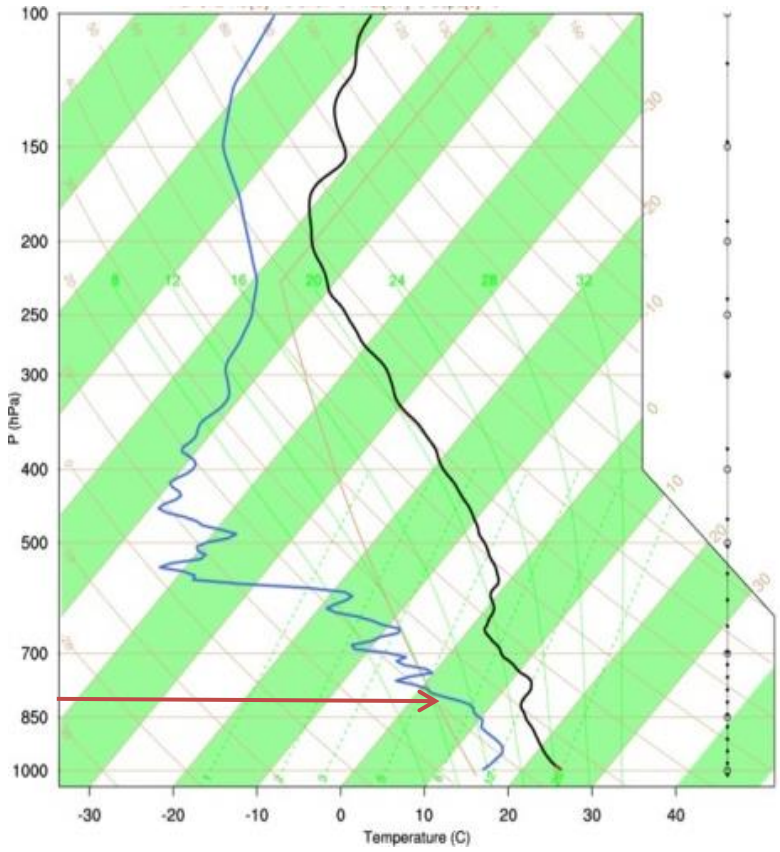

Figure A.2.2. Example sounding from 1145 HST 25 July, 2010. The blue line (left) represents the dewpoint temperature profile. The black line (right) represents the temperature profile. Red arrow illustrates the reference pressure level of minimum refractivity gradient. Location of observation is approximately 19.51˚N – 160.27˚W. Inversion Base is observed at the approximate height of 2.1 km and a corresponding pressure level of 807 hPa. Sounding data was obtained from the Taiwan Analysis Center for COSMIC (http://tacc.cwb.gov.tw/cdaac/ 2014).

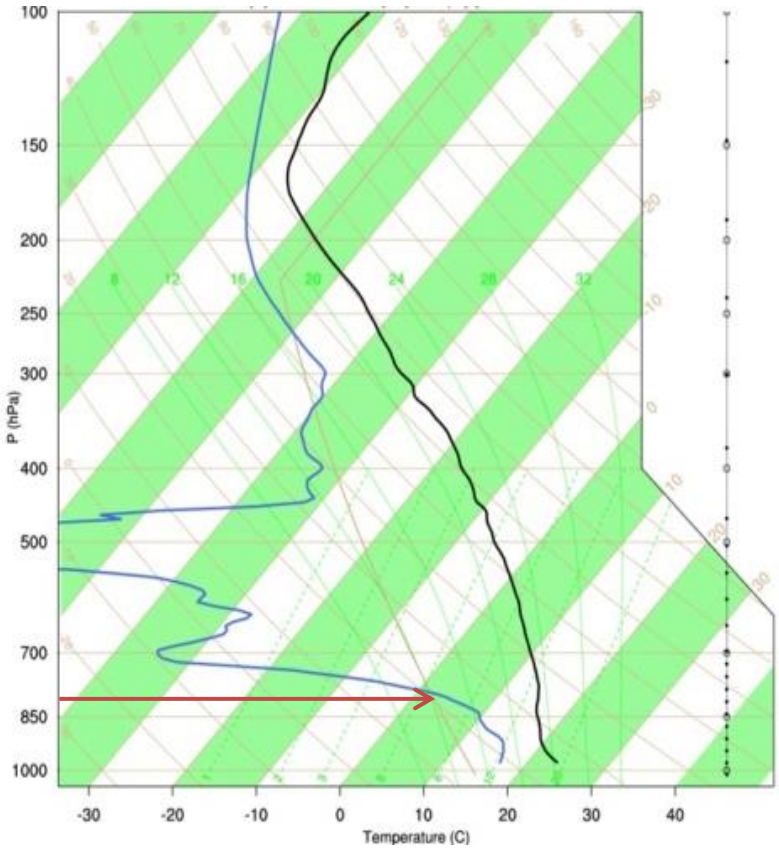

Figure A.2.3. Example sounding from 0419 HST 10 July, 2007. The blue line (left) represents the dewpoint temperature profile. The black line (right) represents the temperature profile. Red arrow illustrates the reference pressure level of minimum refractivity gradient. Location of observation is approximately 19.58˚N – 164.25˚W. Inversion Base Height is observed at the approximate height of 2.1 km and a corresponding pressure level of 795 hPa. Sounding data was obtained from the Taiwan Analysis Center for COSMIC (http://tacc.cwb.gov.tw/cdaac/ 2014).

Appendix 3. Additional GPS RO Observations

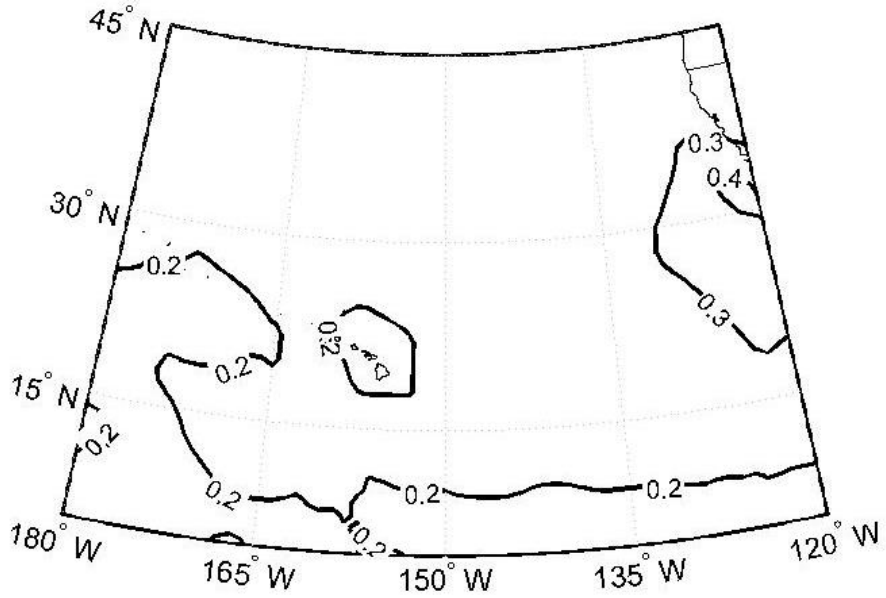

Figure A.3.1. Climatology standard deviation (km) of RMG (unitless) for JJA-C 2007-2012 over 5˚x5˚analysis region (5˚N-45˚N, 120˚W-180˚W).

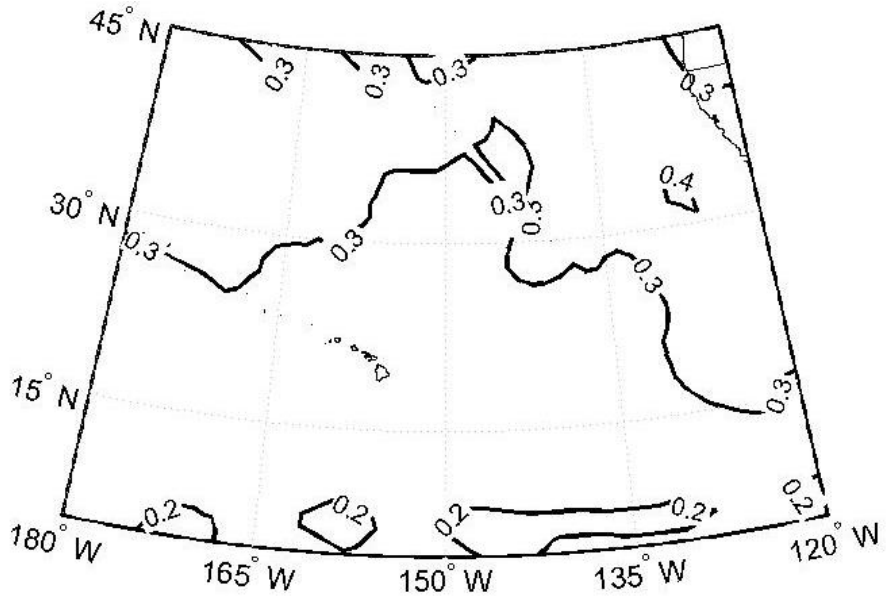

Figure A.3.2. Climatology standard deviation (km) of RMG (unitless) for DJF-C 2007-2012 over 5˚x5˚analysis region (5˚N-45˚N, 120˚W-180˚W).

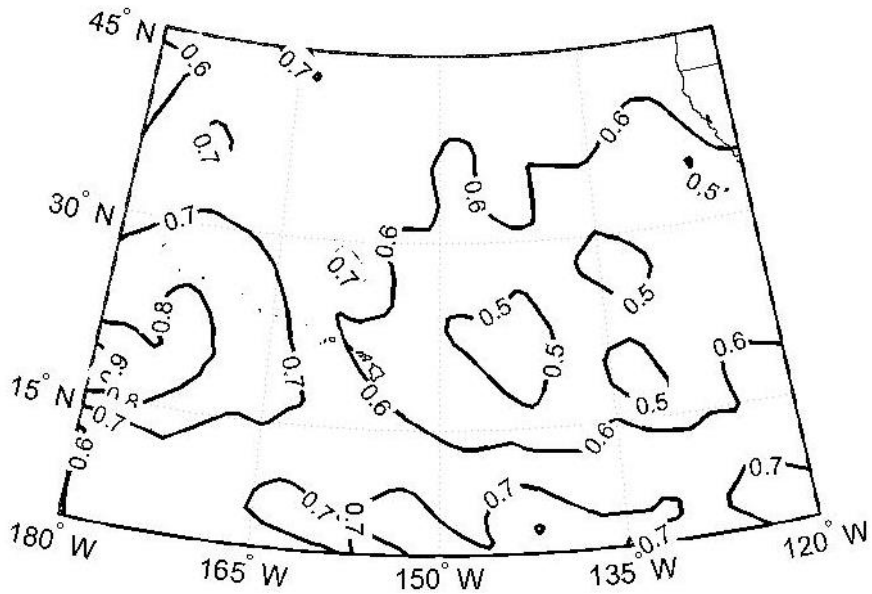

Figure A.3.3. Standard deviation of median inversion base height (km) for JJA 2007-2012 trade wind flow.

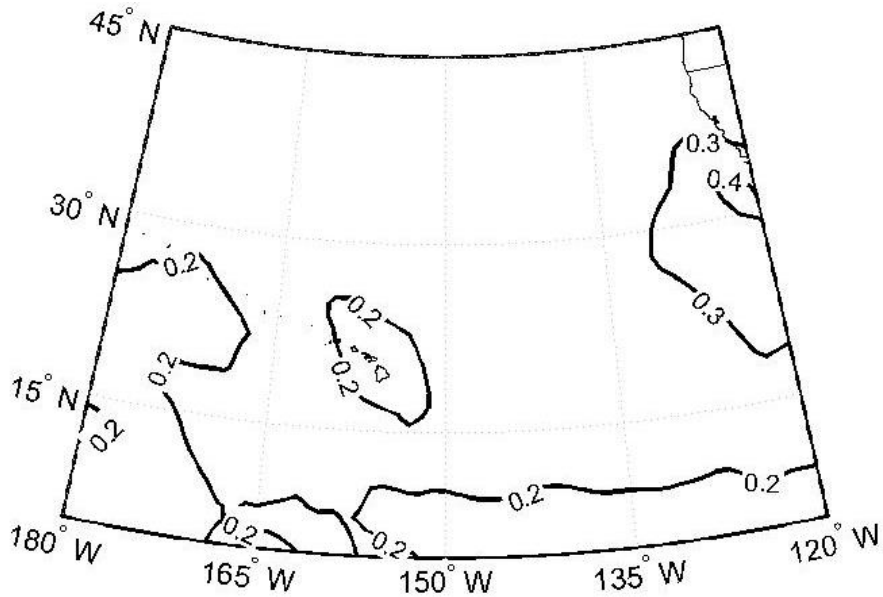

Figure A.3.4. Trade wind climatology standard deviation (km) of RMG (unitless) for JJA-TW 2007-2012 over 5˚x5˚analysis region (5˚N-45˚N, 120˚W-180˚W).

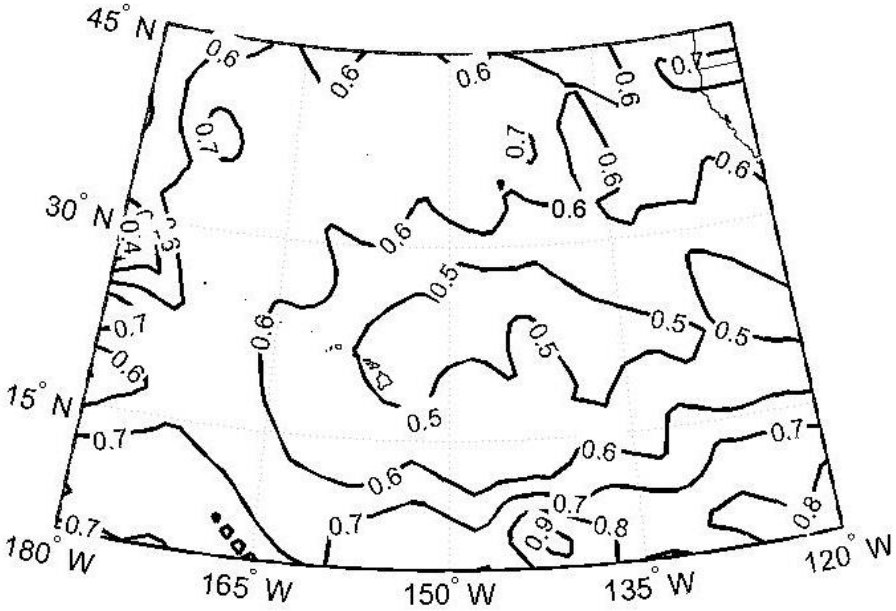

Figure A.3.5. Standard deviation (km) of median inversion base height for DJF 2007 – 2012 trade wind flow.

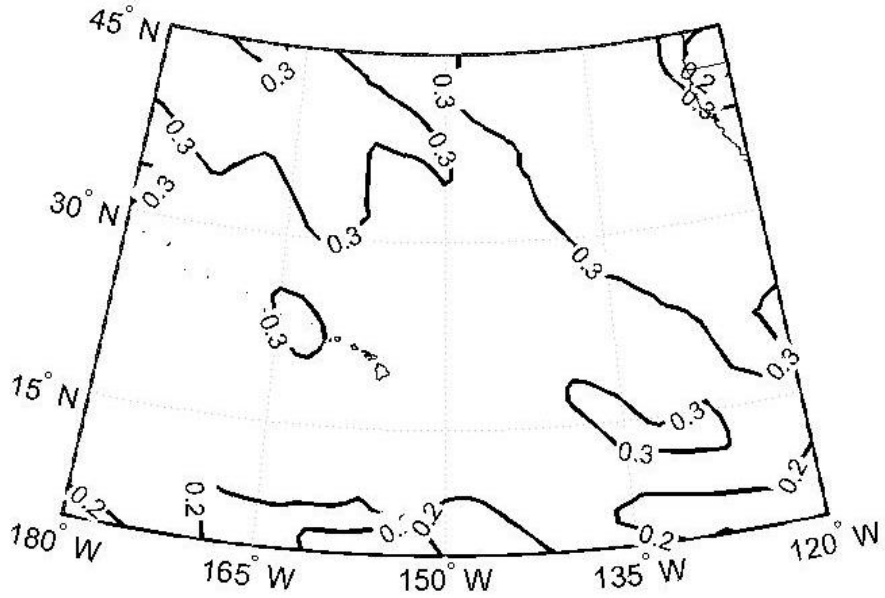

Figure A.3.6. Trade wind climatology standard deviation (km) of RMG (unitless) for DJF-TW 2007-2012 over 5˚x5˚analysis region (5˚N-45˚N, 120˚W-180˚W).

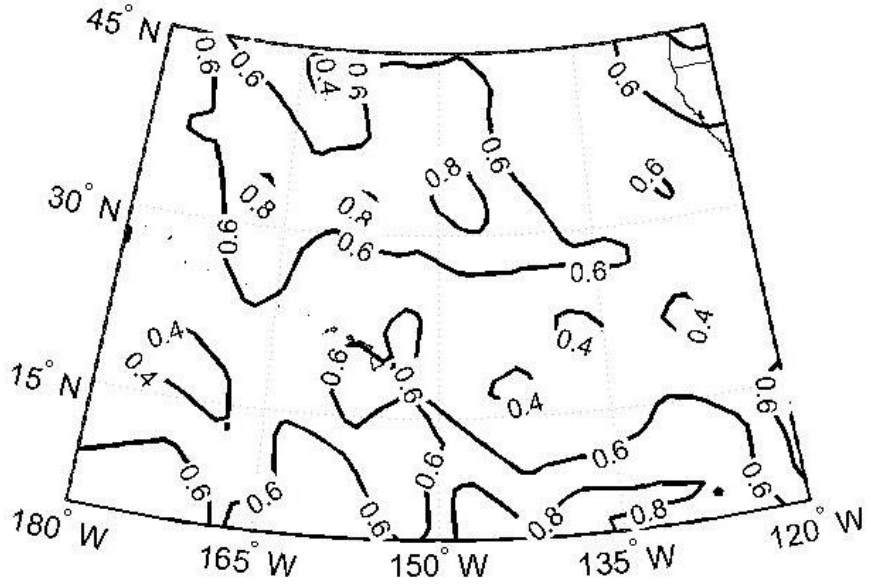

Figure A.3.7. Median inversion base height standard deviation (km) for El Niño (DJF 2010).

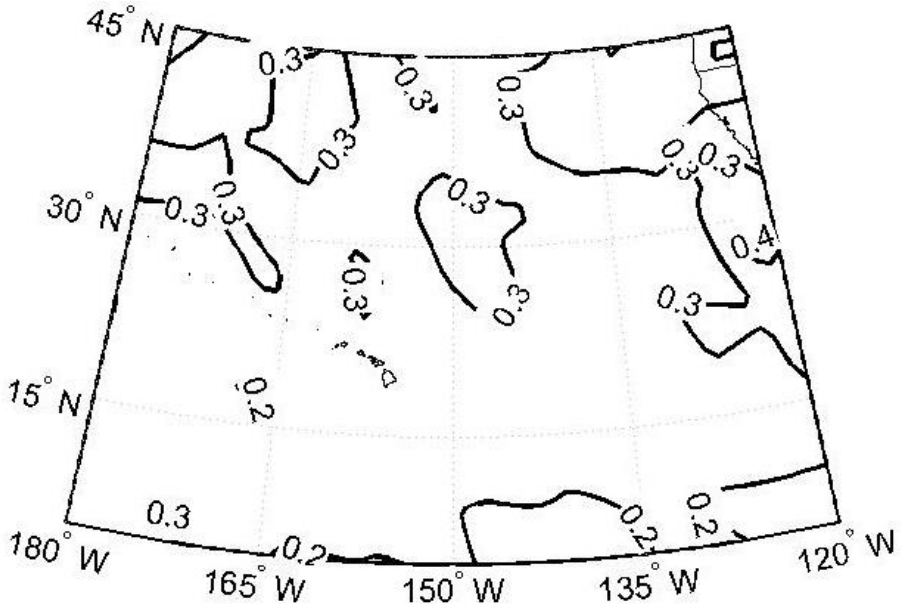

Figure A.3.8. El Niño standard deviation (km) of RMG (unitless) for DJF 2010 over 5˚x5˚analysis region (5˚N-45˚N, 120˚W-180˚W).

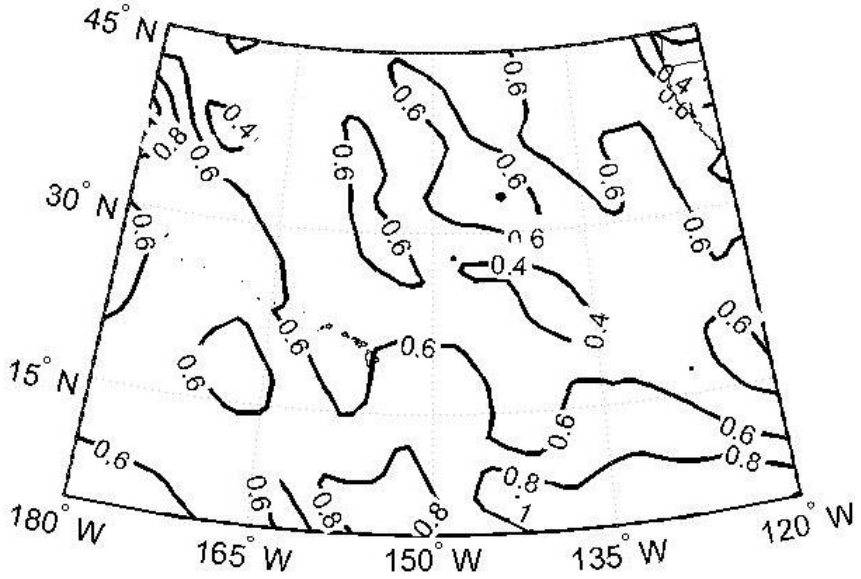

Figure A 3.9. Median inversion base height standard deviation (km) for La Niña (DJF 2011).

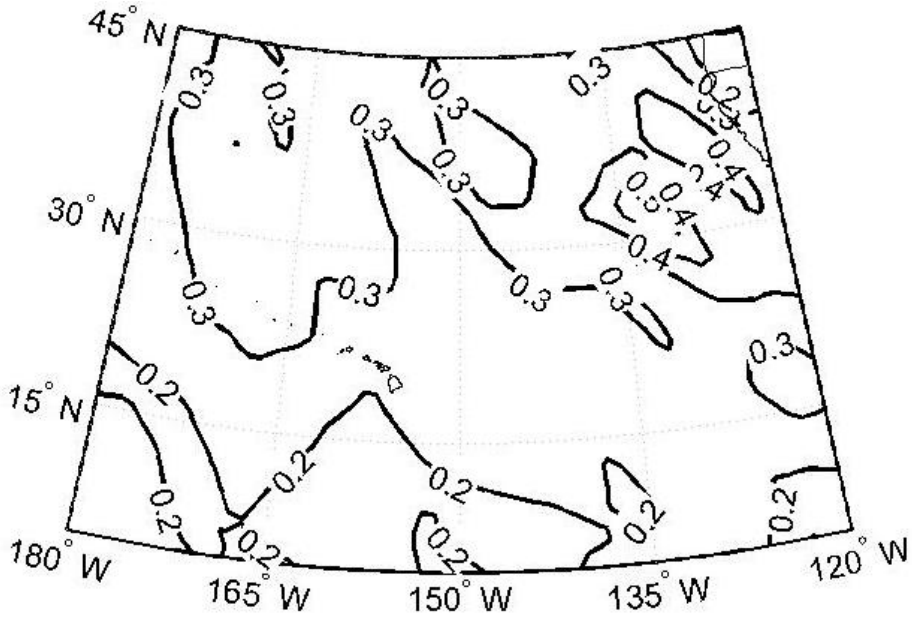

Figure A.3.10. La Niña standard deviation (km) of RMG (unitless) for DJF 2011 over 5˚x5˚analysis region (5˚N-45˚N, 120˚W-180˚W).

Appendix 4. Calendar of Trade Wind Dates

Table A.4.1. Calendar of trade wind climatology dates for JJA 2007-2012.

Table of JJA Trade Wind Days (2007-2012)					
2007	**2008**	**2009**	**2010**	**2011**	**2012**
6/1/2007	6/1/2008	6/1/2009	6/1/2010	6/1/2011	6/1/2012
6/2/2007	6/2/2008	6/2/2009	6/2/2010	6/2/2011	6/2/2012
6/4/2007	6/3/2008	6/3/2009	6/3/2010	6/3/2011	6/3/2012
6/5/2007	6/4/2008	6/4/2009	6/4/2010	6/4/2011	6/4/2012
6/6/2007	6/5/2008	6/5/2009	6/5/2010	6/5/2011	6/5/2012
6/7/2007	6/6/2008	6/6/2009	6/6/2010	6/8/2011	6/6/2012
6/8/2007	6/7/2008	6/7/2009	6/7/2010	6/9/2011	6/7/2012
6/9/2007	6/8/2008	6/10/2009	6/8/2010	6/10/2011	6/8/2012
6/10/2007	6/9/2008	6/11/2009	6/9/2010	6/11/2011	6/9/2012
6/11/2007	6/10/2008	6/12/2009	6/10/2010	6/12/2011	6/16/2012
6/12/2007	6/11/2008	6/13/2009	6/11/2010	6/13/2011	6/17/2012
6/13/2007	6/13/2008	6/14/2009	6/12/2010	6/14/2011	6/18/2012
6/14/2007	6/14/2008	6/15/2009	6/13/2010	6/15/2011	6/19/2012
6/16/2007	6/15/2008	6/16/2009	6/14/2010	6/16/2011	6/20/2012
6/17/2007	6/16/2008	6/17/2009	6/15/2010	6/17/2011	6/21/2012
6/18/2007	6/19/2008	6/18/2009	6/16/2010	6/18/2011	6/22/2012
6/19/2007	6/20/2008	6/19/2009	6/17/2010	6/19/2011	6/23/2012
6/20/2007	6/21/2008	6/20/2009	6/19/2010	6/20/2011	6/24/2012
6/21/2007	6/22/2008	6/21/2009	6/20/2010	6/23/2011	6/25/2012
6/22/2007	6/23/2008	6/22/2009	6/21/2010	6/24/2011	6/26/2012
6/23/2007	6/24/2008	6/23/2009	6/22/2010	6/25/2011	6/27/2012
6/24/2007	6/25/2008	6/24/2009	6/23/2010	6/26/2011	6/30/2012
6/25/2007	6/26/2008	6/25/2009	6/24/2010	6/27/2011	7/1/2012
6/26/2007	6/27/2008	6/26/2009	6/25/2010	6/28/2011	7/2/2012
6/27/2007	6/28/2008	6/27/2009	6/26/2010	6/29/2011	7/3/2012
6/28/2007	7/2/2008	6/28/2009	6/27/2010	6/30/2011	7/4/2012
6/29/2007	7/3/2008	6/29/2009	6/28/2010	7/1/2011	7/5/2012
6/30/2007	7/4/2008	7/1/2009	6/29/2010	7/2/2011	7/6/2012
7/1/2007	7/5/2008	7/2/2009	6/30/2010	7/3/2011	7/7/2012
7/2/2007	7/6/2008	7/3/2009	7/1/2010	7/4/2011	7/8/2012
7/3/2007	7/7/2008	7/5/2009	7/2/2010	7/5/2011	7/9/2012
7/4/2007	7/8/2008	7/6/2009	7/3/2010	7/6/2011	7/10/2012
7/5/2007	7/11/2008	7/7/2009	7/4/2010	7/7/2011	7/12/2012
7/6/2007	7/12/2008	7/8/2009	7/5/2010	7/8/2011	7/16/2012

7/7/2007	7/13/2008	7/9/2009	7/8/2010	7/9/2011	7/17/2012
7/8/2007	7/14/2008	7/10/2009	7/9/2010	7/10/2011	7/18/2012
7/9/2007	7/15/2008	7/11/2009	7/10/2010	7/11/2011	7/19/2012
7/10/2007	7/16/2008	7/12/2009	7/11/2010	7/12/2011	7/20/2012
7/11/2007	7/17/2008	7/13/2009	7/12/2010	7/13/2011	7/21/2012
7/12/2007	7/18/2008	7/14/2009	7/13/2010	7/14/2011	7/22/2012
7/13/2007	7/19/2008	7/15/2009	7/14/2010	7/15/2011	7/23/2012
7/14/2007	7/20/2008	7/16/2009	7/15/2010	7/16/2011	7/24/2012
7/15/2007	7/21/2008	7/17/2009	7/16/2010	7/17/2011	7/25/2012
7/16/2007	7/22/2008	7/18/2009	7/17/2010	7/18/2011	7/26/2012
7/17/2007	7/24/2008	7/19/2009	7/18/2010	7/19/2011	7/27/2012
7/18/2007	7/25/2008	7/21/2009	7/19/2010	7/20/2011	7/28/2012
7/19/2007	7/26/2008	7/22/2009	7/20/2010	7/21/2011	7/29/2012
7/22/2007	7/27/2008	7/23/2009	7/21/2010	7/22/2011	7/30/2012
7/23/2007	7/28/2008	7/24/2009	7/22/2010	7/23/2011	7/31/2012
7/24/2007	7/29/2008	7/25/2009	7/25/2010	7/24/2011	8/1/2012
7/25/2007	7/30/2008	7/26/2009	7/26/2010	7/25/2011	8/2/2012
7/26/2007	7/31/2008	7/27/2009	7/27/2010	7/26/2011	8/6/2012
7/27/2007	8/1/2008	7/28/2009	7/28/2010	7/27/2011	8/7/2012
7/28/2007	8/3/2008	7/29/2009	7/29/2010	7/28/2011	8/8/2012
7/29/2007	8/5/2008	7/30/2009	7/30/2010	7/29/2011	8/9/2012
8/1/2007	8/6/2008	8/1/2009	7/31/2010	7/30/2011	8/10/2012
8/2/2007	8/8/2008	8/2/2009	8/1/2010	7/31/2011	8/11/2012
8/3/2007	8/9/2008	8/3/2009	8/2/2010	8/1/2011	8/12/2012
8/4/2007	8/10/2008	8/4/2009	8/3/2010	8/2/2011	8/13/2012
8/5/2007	8/11/2008	8/5/2009	8/4/2010	8/3/2011	8/14/2012
8/6/2007	8/12/2008	8/6/2009	8/5/2010	8/4/2011	8/15/2012
8/7/2007	8/13/2008	8/7/2009	8/6/2010	8/5/2011	8/16/2012
8/8/2007	8/14/2008	8/8/2009	8/7/2010	8/6/2011	8/17/2012
8/9/2007	8/16/2008	8/9/2009	8/8/2010	8/7/2011	8/18/2012
8/10/2007	8/17/2008	8/10/2009	8/9/2010	8/8/2011	8/19/2012
8/11/2007	8/18/2008	8/11/2009	8/10/2010	8/9/2011	8/20/2012
8/12/2007	8/19/2008	8/16/2009	8/11/2010	8/10/2011	8/21/2012
8/13/2007	8/20/2008	8/21/2009	8/12/2010	8/11/2011	8/26/2012
8/17/2007	8/21/2008	8/22/2009	8/13/2010	8/12/2011	8/27/2012
8/18/2007	8/22/2008	8/23/2009	8/15/2010	8/15/2011	8/28/2012
8/19/2007	8/23/2008	8/24/2009	8/16/2010	8/16/2011	8/29/2012
8/20/2007	8/24/2008	8/25/2009	8/17/2010	8/17/2011	8/30/2012
8/21/2007	8/25/2008	8/26/2009	8/18/2010	8/18/2011	8/31/2012
8/22/2007	8/26/2008	8/27/2009	8/19/2010	8/19/2011	

8/23/2007	8/27/2008	8/28/2009	8/20/2010	8/20/2011	
8/24/2007	8/29/2008	8/29/2009	8/21/2010	8/21/2011	
8/25/2007	8/30/2008	8/30/2009	8/22/2010	8/22/2011	
8/26/2007			8/23/2010	8/25/2011	
8/27/2007			8/24/2010	8/26/2011	
8/28/2007			8/25/2010	8/27/2011	
			8/26/2010	8/28/2011	
			8/27/2010	8/29/2011	
			8/28/2010	8/30/2011	
			8/29/2010	8/31/2011	
			8/30/2010		
			8/31/2010		

Table A.4.2. Calendar of trade wind climatology dates for DJF 2007-2012.

Table of DJF Trade Wind Days (2007-2012)					
2006-2007	**2007-2008**	**2008-2009**	**2009-2010**	**2010-2011**	**2011-2012**
12/3/2006	12/13/2007	12/4/2008	12/1/2009	12/3/2010	12/4/2011
12/4/2006	12/14/2007	12/5/2008	12/8/2009	12/4/2010	12/5/2011
12/10/2006	12/15/2007	12/6/2008	12/9/2009	12/5/2010	12/6/2011
12/11/2006	12/16/2007	12/7/2008	12/10/2009	12/6/2010	12/8/2011
12/12/2006	12/17/2007	12/10/2008	12/11/2009	12/15/2010	12/9/2011
12/13/2006	12/18/2007	12/11/2008	12/12/2009	12/16/2010	12/10/2011
12/14/2006	12/19/2007	12/18/2008	12/13/2009	12/26/2010	12/11/2011
12/16/2006	12/20/2007	12/19/2008	12/20/2009	12/27/2010	12/15/2011
12/17/2006	12/21/2007	12/20/2008	12/21/2009	12/28/2010	12/16/2011
12/18/2006	12/26/2007	12/21/2008	12/25/2009	1/2/2011	12/17/2011
12/29/2006	1/1/2008	12/22/2008	12/26/2009	1/3/2011	12/18/2011
12/30/2006	1/2/2008	1/7/2009	12/27/2009	1/4/2011	12/22/2011
12/31/2006	1/3/2008	1/8/2009	12/28/2009	1/16/2011	12/23/2011
1/4/2007	1/4/2008	1/11/2009	1/9/2010	1/17/2011	12/24/2011
1/5/2007	1/5/2008	1/18/2009	1/11/2010	1/20/2011	12/25/2011
1/6/2007	1/6/2008	1/19/2009	1/12/2010	1/21/2011	12/26/2011
1/7/2007	1/18/2008	1/21/2009	1/13/2010	1/22/2011	12/27/2011
1/15/2007	1/19/2008	1/22/2009	1/14/2010	1/23/2011	12/28/2011
1/16/2007	1/20/2008	1/23/2009	1/15/2010	1/24/2011	12/29/2011
1/17/2007	1/21/2008	1/24/2009	1/16/2010	1/26/2011	12/30/2011
1/24/2007	1/22/2008	2/2/2009	1/17/2010	1/27/2011	1/1/2012
1/25/2007	1/23/2008	2/3/2009	1/21/2010	1/28/2011	1/5/2012

1/26/2007	1/24/2008	2/4/2009	1/22/2010	1/29/2011	1/6/2012
1/27/2007	1/25/2008	2/6/2009	1/23/2010	2/1/2011	1/7/2012
2/12/2007	1/27/2008	2/7/2009	1/25/2010	2/2/2011	1/8/2012
2/13/2007	1/28/2008	2/14/2009	1/26/2010	2/3/2011	1/9/2012
2/14/2007	1/29/2008	2/15/2009	1/27/2010	2/8/2011	1/10/2012
2/15/2007	2/13/2008	2/16/2009	2/1/2010	2/9/2011	1/11/2012
2/18/2007	2/14/2008	2/17/2009	2/2/2010	2/10/2011	1/20/2012
2/19/2007	2/15/2008	2/18/2009	2/4/2010	2/19/2011	1/21/2012
2/20/2007	2/29/2008	2/19/2009	2/5/2010	2/20/2011	1/22/2012
2/21/2007		2/24/2009	2/6/2010	2/21/2011	1/23/2012
2/22/2007		2/25/2009	2/8/2010	2/22/2011	1/27/2012
		2/26/2009	2/9/2010	2/23/2011	1/28/2012
		2/27/2009	2/10/2010	2/27/2011	1/29/2012
		2/28/2009	2/12/2010	2/28/2011	1/30/2012
			2/13/2010		1/31/2012
			2/14/2010		2/2/2012
			2/15/2010		2/7/2012
			2/16/2010		2/9/2012
			2/20/2010		2/10/2012
			2/21/2010		2/11/2012
			2/24/2010		2/12/2012
			2/27/2010		2/13/2012
			2/28/2010		2/14/2012
					2/15/2012
					2/16/2012
					2/17/2012
					2/18/2012
					2/19/2012
					2/20/2012
					2/21/2012
					2/22/2012
					2/23/2012

Appendix 5. Two Tailed t-test

Two tailed t-test for difference of means of independent samples (Panofsky and Brier 1958):

$$t = \frac{\bar{X}_1 - \bar{X}_2}{\sqrt{\frac{N_1 s_1^2 + N_2 s_2^2}{N_1 + N_2 - 2}\left(\frac{1}{N_1} + \frac{1}{N_2}\right)}} \qquad \text{(Eq. A.5.1)}$$

Where:

$\bar{X}_1$ = Mean of independent sample 1

$\bar{X}_2$ = Mean of independent sample 2

N_1 = Population of sample 1

N_2 = Population of sample 2

s_1 = Standard deviation of sample 1 population

s_2 = Standard deviation of sample 2 population

$N_1 + N_2 - 2$ = Degrees of Freedom

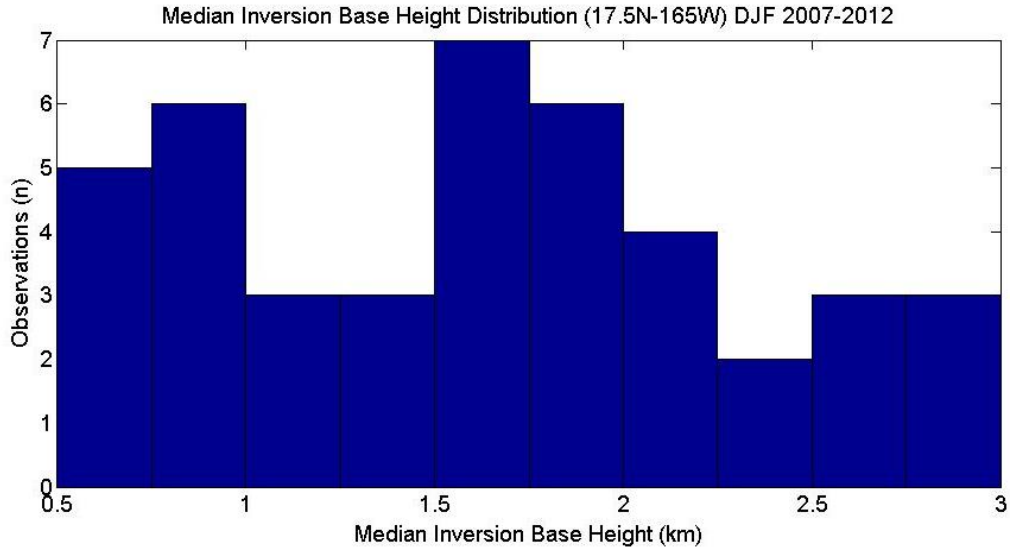

Figure A.5.1. Histogram of observed median inversion base height z_i (km) for 2.5˚x2.5˚ grid box centered on 17.5˚N, 165˚W during DJF 2007-2012.

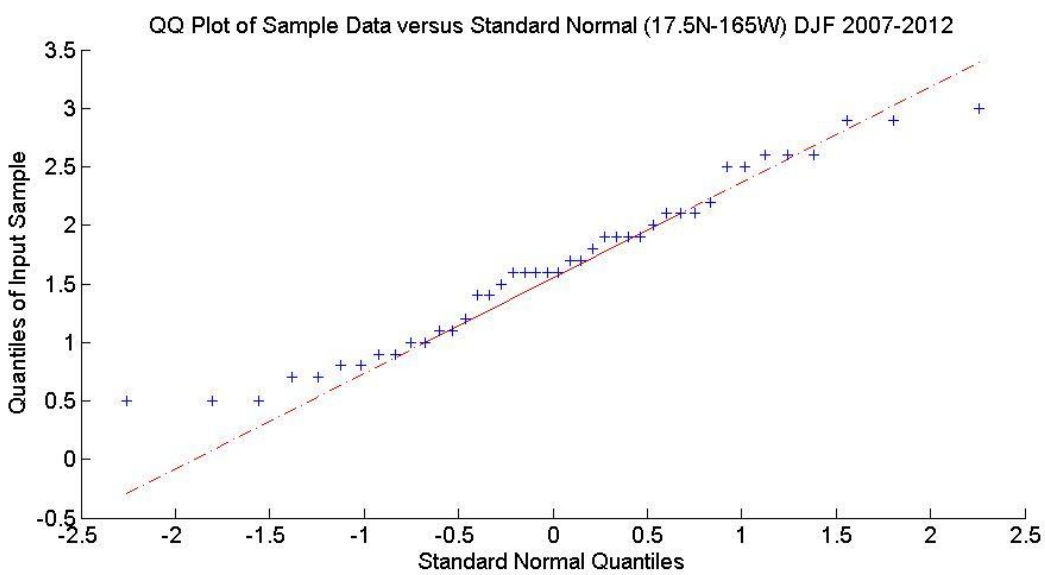

Figure A.5.2. Quantile-quantile plot (q-q plot) of observed median inversion base height z_i (km) for 2.5˚x2.5˚ grid box centered on 17.5˚N, 165˚W during DJF 2007-2012. X-axis represents standard normal quantiles; Y-axis represents quantiles of input samples. Each observation is represented by a blue cross. The red line represents the 1-to-1 relationship between a standard normal data distribution and the sampled data set. If blue crosses are oriented along the red diagonal line, the population distribution is considered to be "normal".

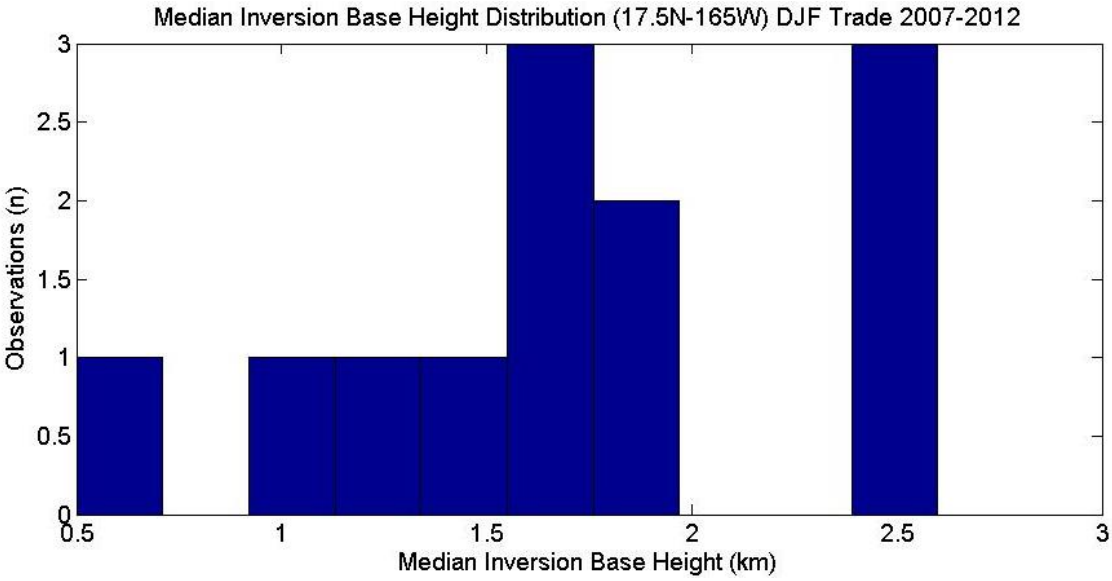

Figure A.5.3. Histogram of observed median inversion base height z_i (km) for 2.5˚x2.5˚ grid box centered on 17.5˚N, 165˚W during DJF-TW 2007-2012.

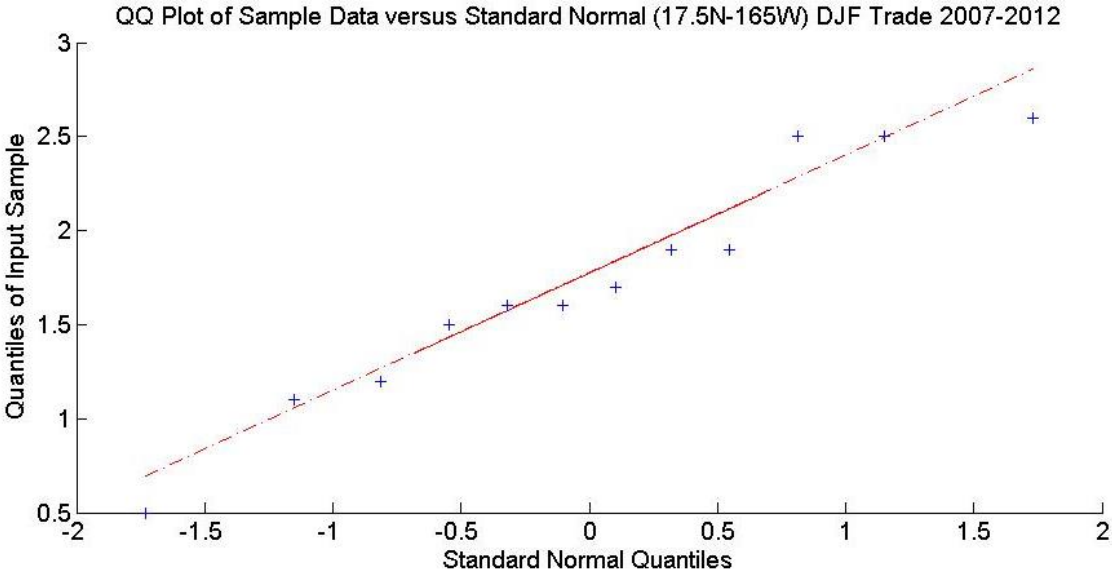

Figure A.5.4. Quantile-quantile plot (q-q plot) of observed median inversion base height z_i (km) for 2.5˚x2.5˚ grid box centered on 17.5˚N, 165˚W during DJF-TW 2007-2012. X-axis represents standard normal quantiles; Y-axis represents quantiles of input samples. Each observation is represented by a blue cross. The red line represents the 1-to-1 relationship between a standard normal data distribution and the sampled data set. If blue crosses are oriented along the red diagonal line, the population distribution is considered to be "normal".

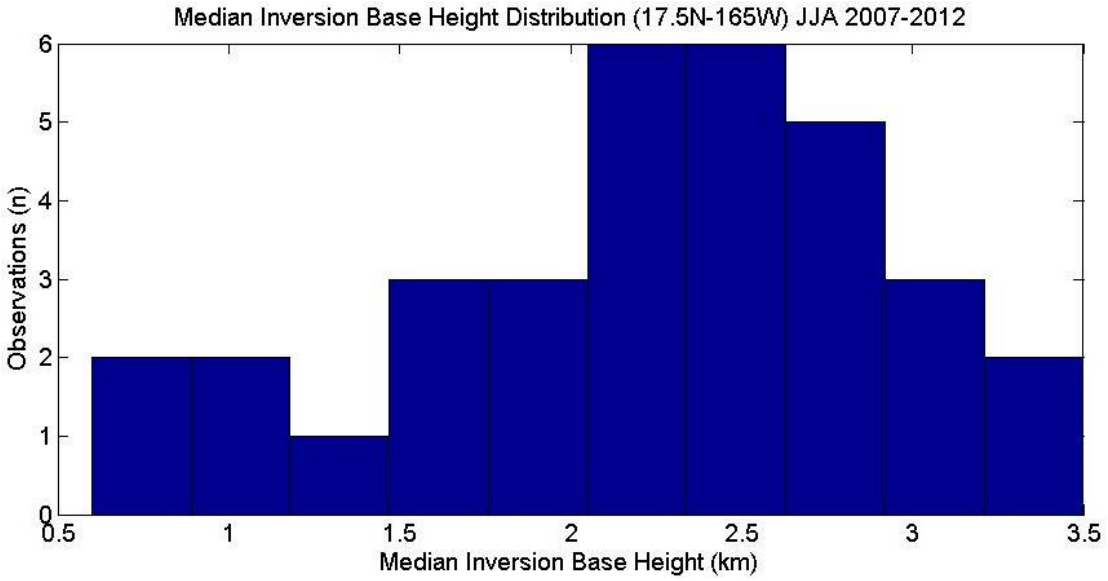

Figure A.5.5. Histogram of observed median inversion base height z_i (km) for 2.5˚x2.5˚ grid box centered on 17.5˚N, 165˚W during JJA 2007-2012.

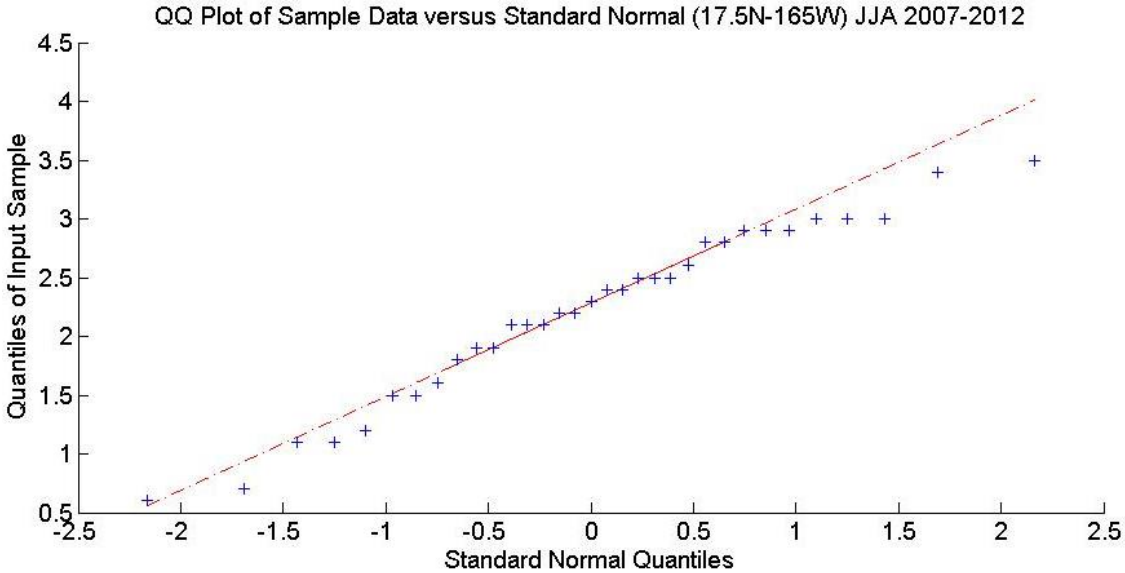

Figure A.5.6. Quantile-quantile plot (q-q plot) of observed median inversion base height z_i (km) for 2.5˚x2.5˚ grid box centered on 17.5˚N, 165˚W during JJA 2007-2012. X-axis represents standard normal quantiles; Y-axis represents quantiles of input samples. Each observation is represented by a blue cross. The red line represents the 1-to-1 relationship between a standard normal data distribution and the sampled data set. If blue crosses are oriented along the red diagonal line, the population distribution is considered to be "normal".

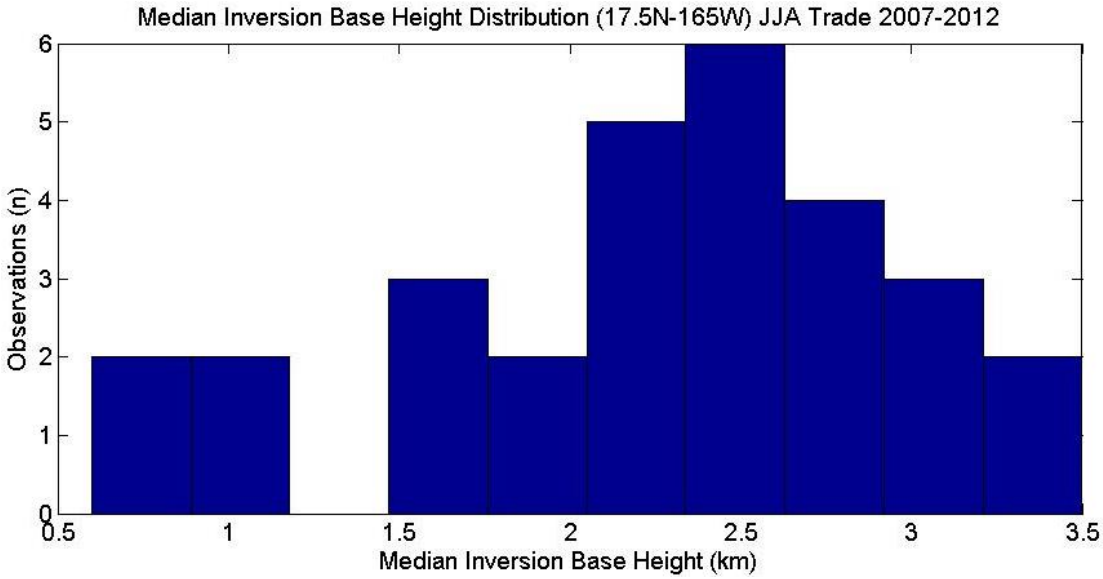

Figure A.5.7. Histogram of observed median inversion base height z_i (km) for 2.5˚x2.5˚ grid box centered on 17.5˚N, 165˚W during JJA-TW 2007-2012.

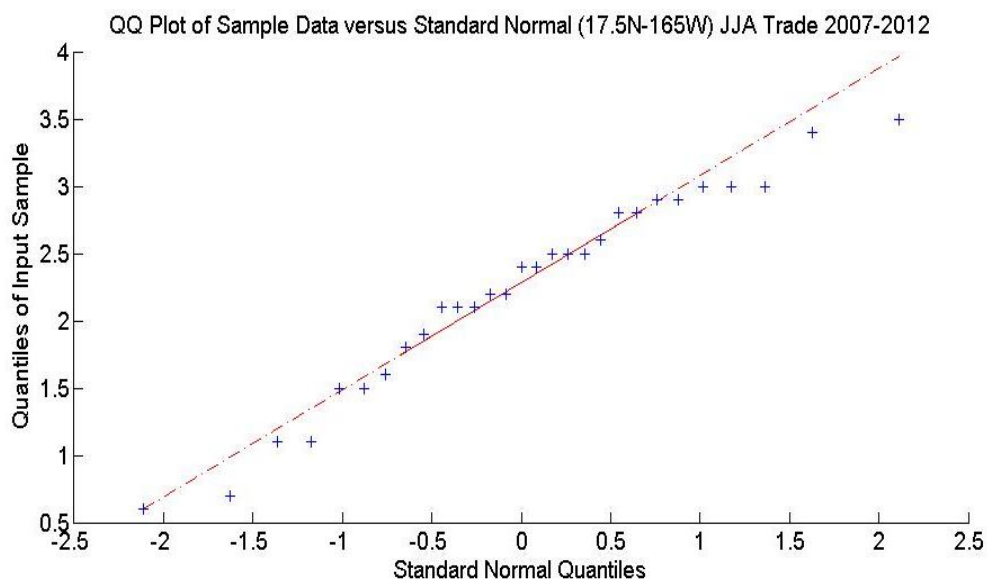

Figure A.5.8. Quantile-quantile plot (q-q plot) of observed median inversion base height z_i (km) for 2.5˚x2.5˚ grid box centered on 17.5˚N, 165˚W during JJA-TW 2007-2012. X-axis represents standard normal quantiles; Y-axis represents quantiles of input samples. Each observation is represented by a blue cross. The red line represents the 1-to-1 relationship between a standard normal data distribution and the sampled data set. If blue crosses are oriented along the red diagonal line, the population distribution is considered to be "normal".

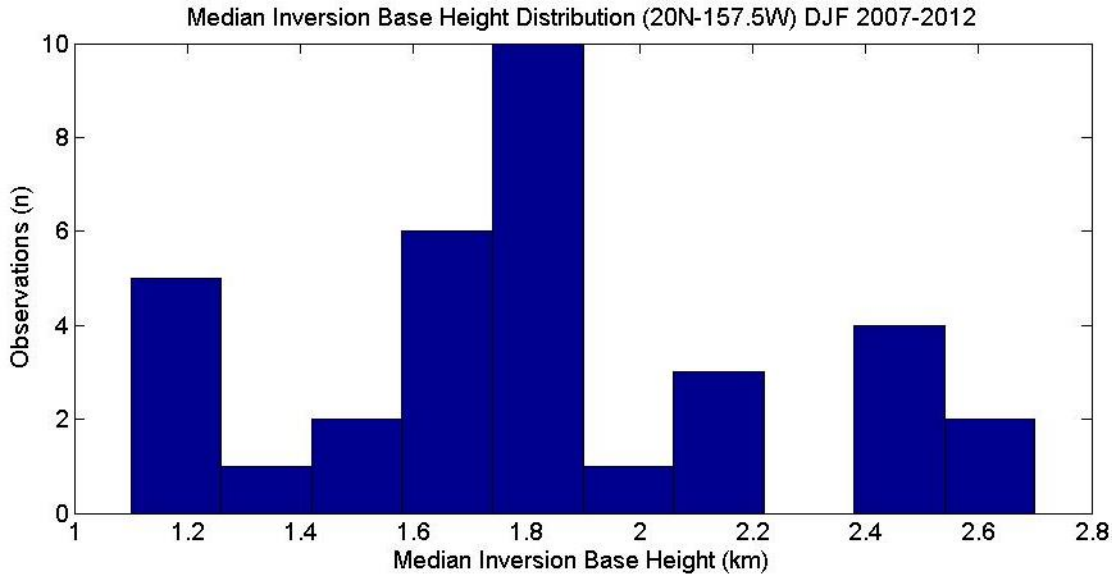

Figure A.5.9. Histogram of observed median inversion base height z_i (km) for 2.5˚x2.5˚ grid box centered on 20˚N, 157.5˚W during DJF 2007-2012.

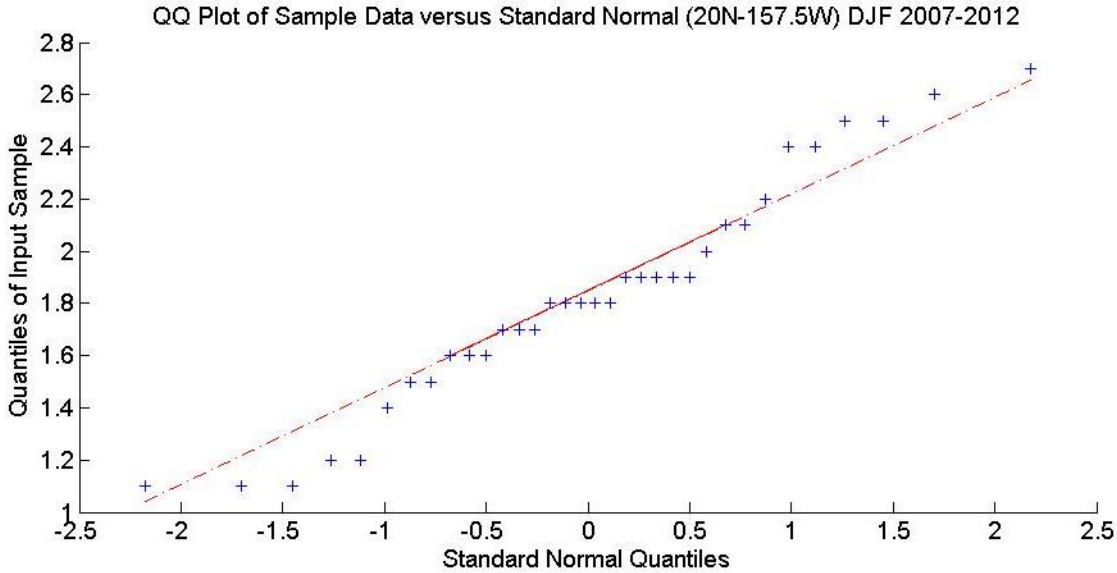

Figure A.5.10. Quantile-quantile plot (q-q plot) of observed median inversion base height z_i (km) for 2.5˚x2.5˚ grid box centered on 20˚N, 157.5˚W during DJF 2007-2012. X-axis represents standard normal quantiles; Y-axis represents quantiles of input samples. Each observation is represented by a blue cross. The red line represents the 1-to-1 relationship between a standard normal data distribution and the sampled data set. If blue crosses are oriented along the red diagonal line, the population distribution is considered to be "normal".

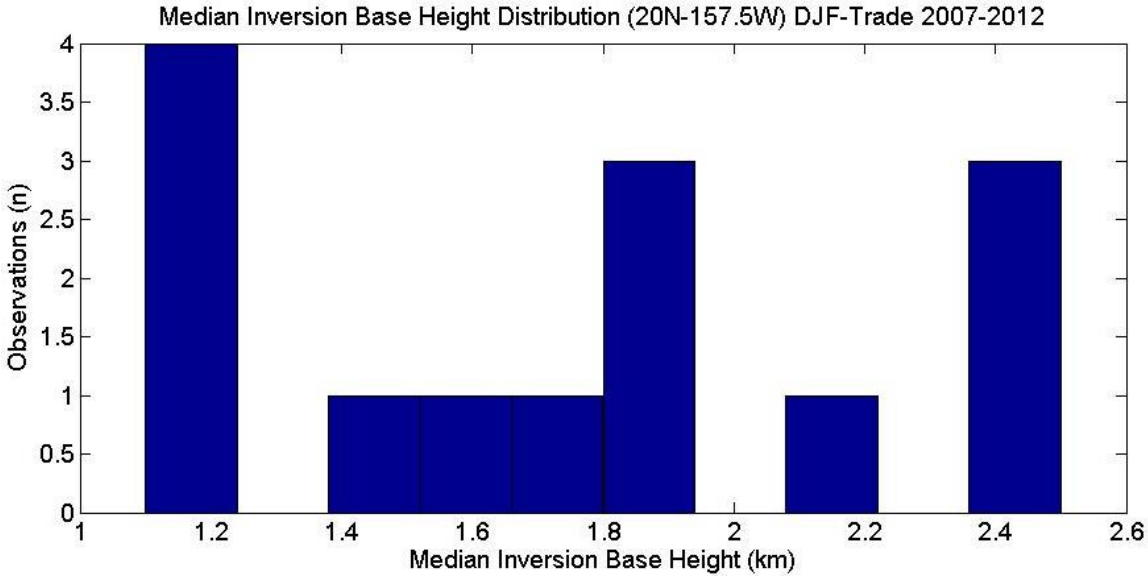

Figure A.5.11. Histogram of observed median inversion base height z_i (km) for 2.5˚x2.5˚ grid box centered on 20˚N, 157.5˚W during DJF-TW 2007-2012.

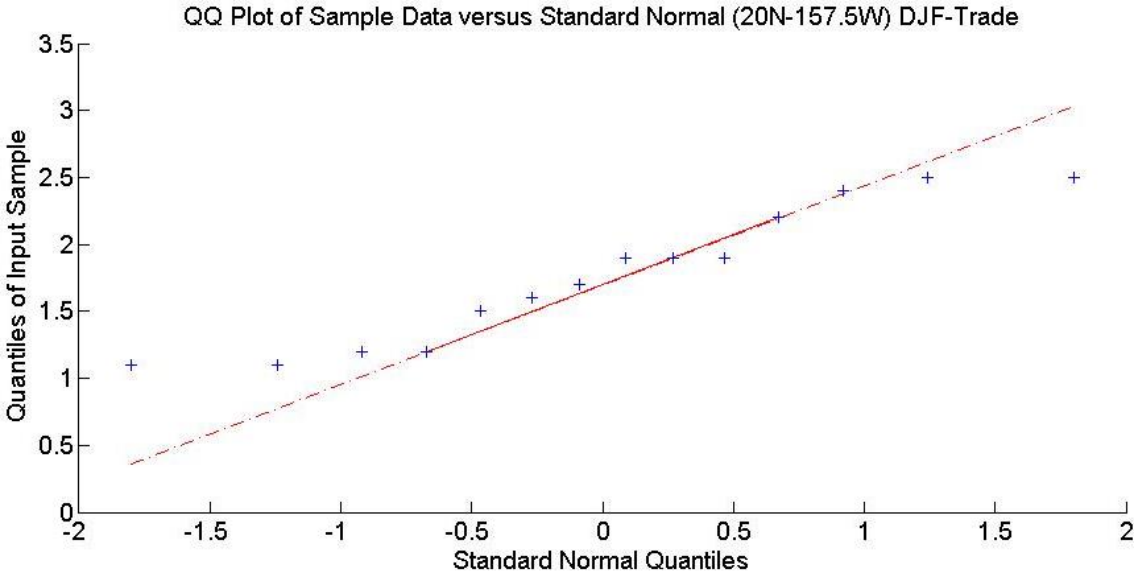

Figure A.5.12. Quantile-quantile plot (q-q plot) of observed median inversion base height z_i (km) for 2.5˚x2.5˚ grid box centered on 20˚N, 157.5˚W during DJF-TW 2007-2012. X-axis represents standard normal quantiles; Y-axis represents quantiles of input samples. Each observation is represented by a blue cross. The red line represents the 1-to-1 relationship between a standard normal data distribution and the sampled data set. If blue crosses are oriented along the red diagonal line, the population distribution is considered to be "normal".

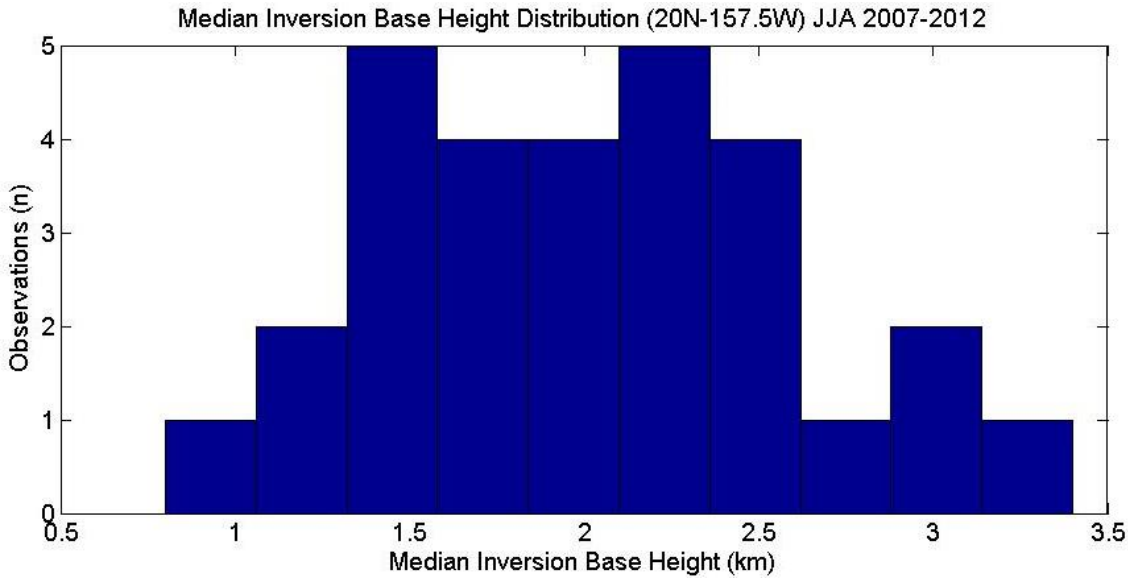

Figure A.5.13. Histogram of observed median inversion base height z_i (km) for 2.5˚x2.5˚ grid box centered on 20˚N, 157.5˚W during JJA 2007-2012.

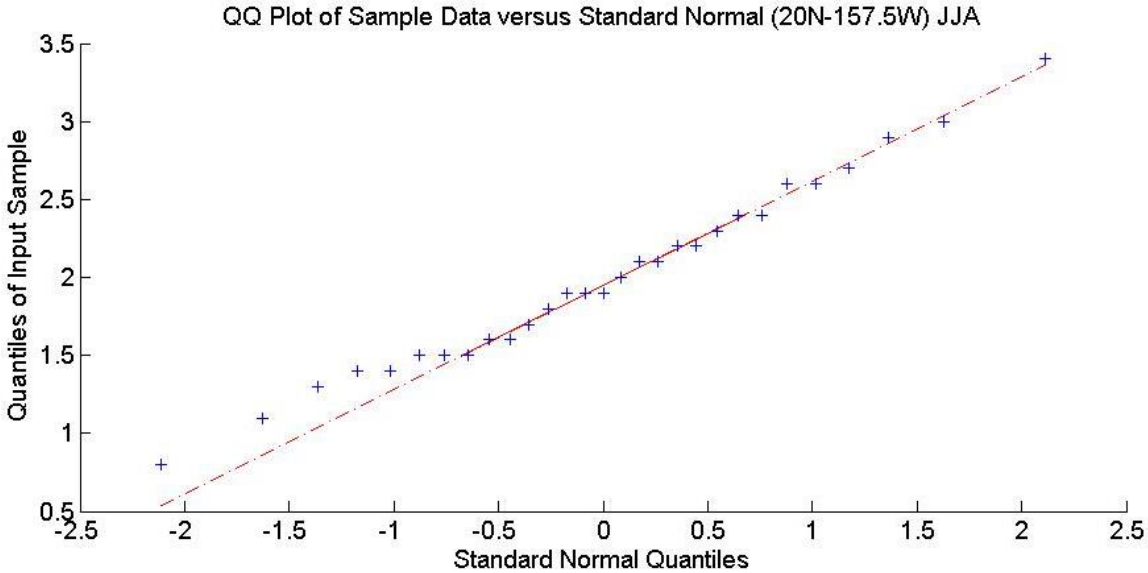

Figure A.5.14. Quantile-quantile plot (q-q plot) of observed median inversion base height z_i (km) for 2.5˚x2.5˚ grid box centered on 20˚N, 157.5˚W during JJA 2007-2012. X-axis represents standard normal quantiles; Y-axis represents quantiles of input samples. Each observation is represented by a blue cross. The red line represents the 1-to-1 relationship between a standard normal data distribution and the sampled data set. If blue crosses are oriented along the red diagonal line, the population distribution is considered to be "normal".

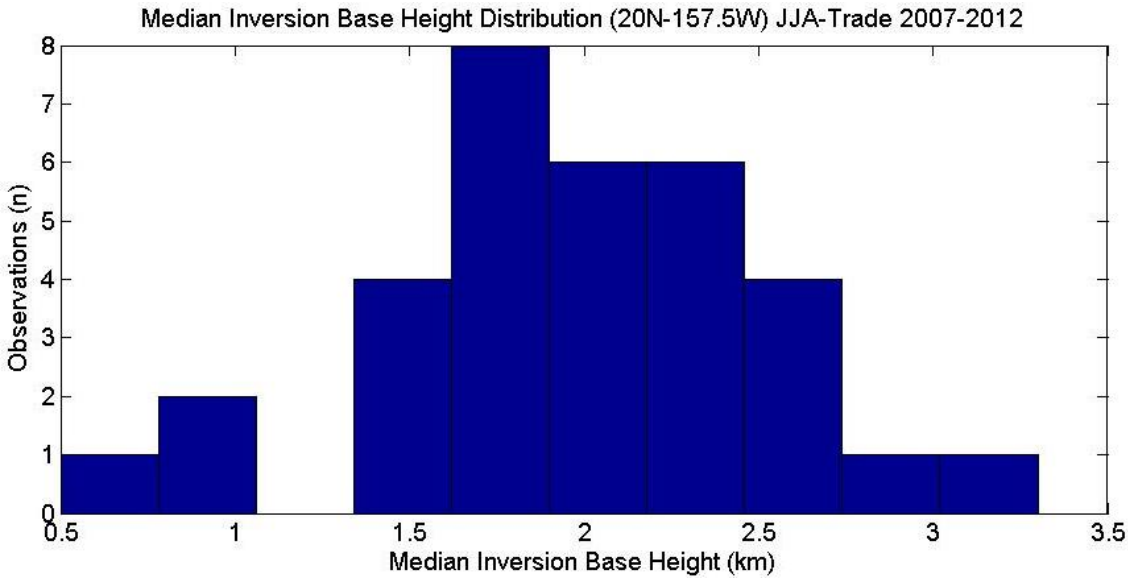

Figure A.5.15. Histogram of observed median inversion base height z_i (km) for 2.5˚x2.5˚ grid box centered on 20˚N, 157.5˚W during JJA-TW 2007-2012.

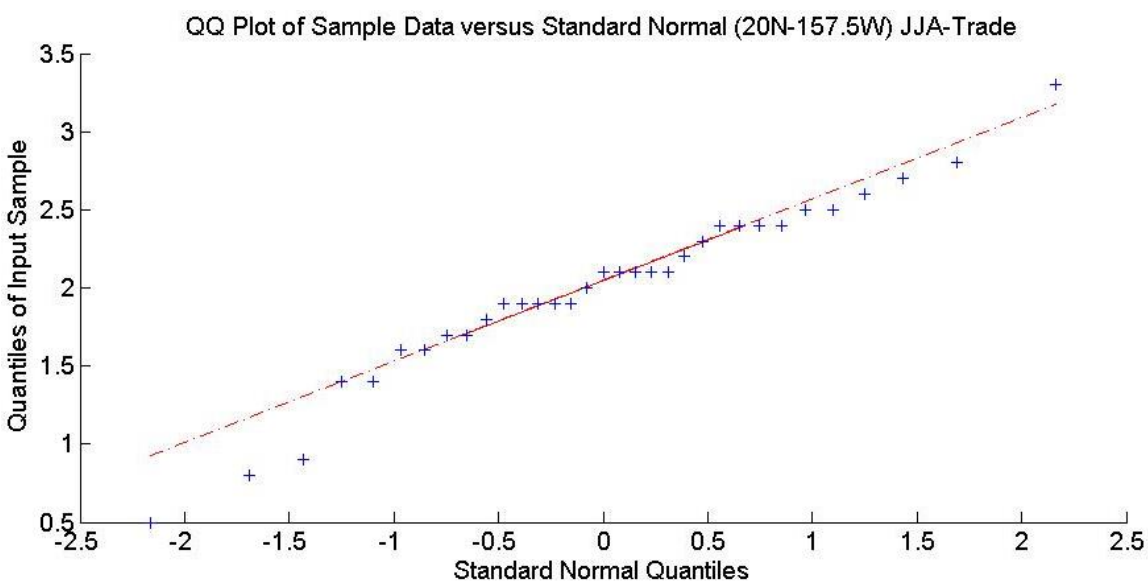

Figure A.5.16. Quantile-quantile plot (q-q plot) of observed median inversion base height z_i (km) for 2.5˚x2.5˚ grid box centered on 20˚N, 157.5˚W during JJA-TW 2007-2012. X-axis represents standard normal quantiles; Y-axis represents quantiles of input samples. Each observation is represented by a blue cross. The red line represents the 1-to-1 relationship between a standard normal data distribution and the sampled data set. If blue crosses are oriented along the red diagonal line, the population distribution is considered to be "normal".

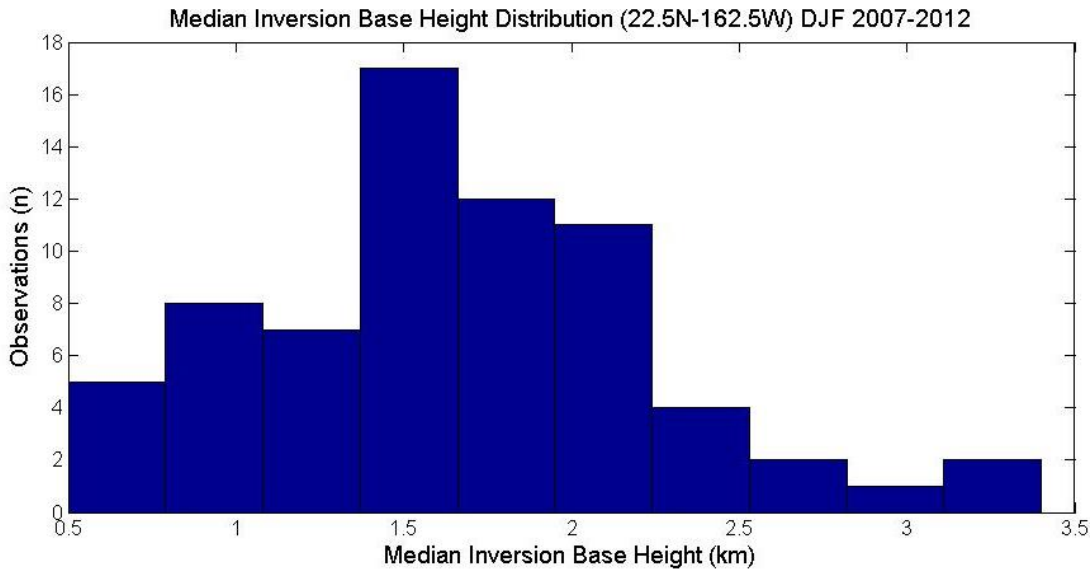

Figure A.5.17. Histogram of observed median inversion base height z_i (km) for 2.5˚x2.5˚ grid box centered on 22.5˚N, 162.5˚W during DJF 2007-2012.

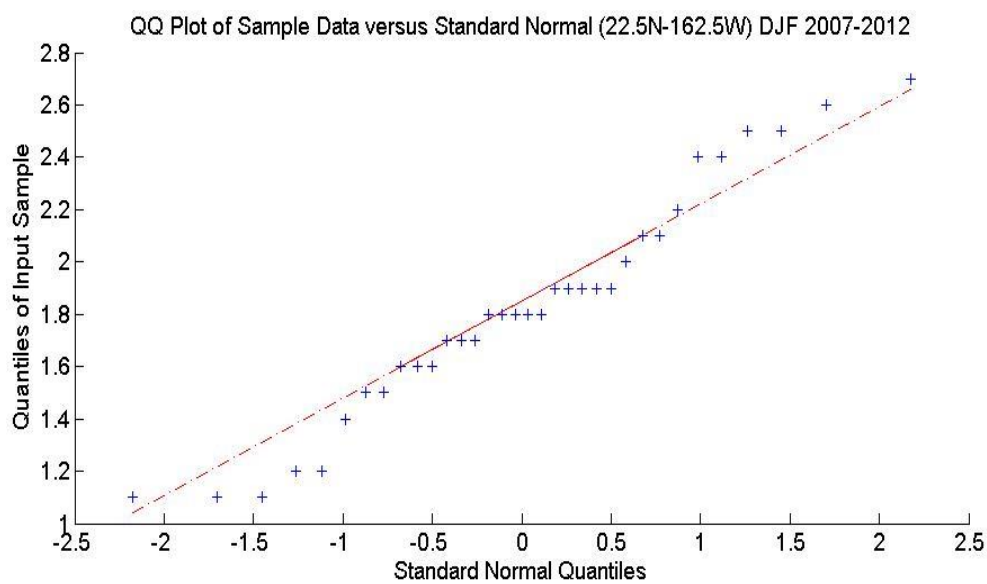

Figure A.5.18. Quantile-quantile plot (q-q plot) of observed median inversion base height z_i (km) for 2.5˚x2.5˚ grid box centered on 22.5˚N, 162.5˚W during DJF 2007-2012. X-axis represents standard normal quantiles; Y-axis represents quantiles of input samples. Each observation is represented by a blue cross. The red line represents the 1-to-1 relationship between a standard normal data distribution and the sampled data set. If blue crosses are oriented along the red diagonal line, the population distribution is considered to be "normal".

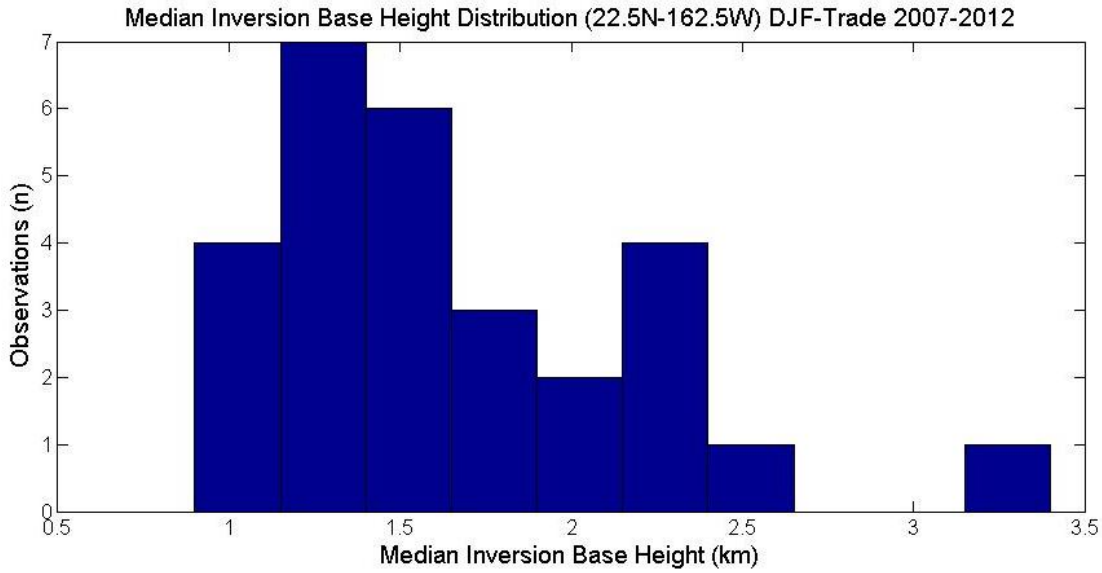

Figure A.5.19. Histogram of observed median inversion base height z_i (km) for 2.5˚x2.5˚ grid box centered on 22.5˚N, 162.5˚W during DJF-TW 2007-2012.

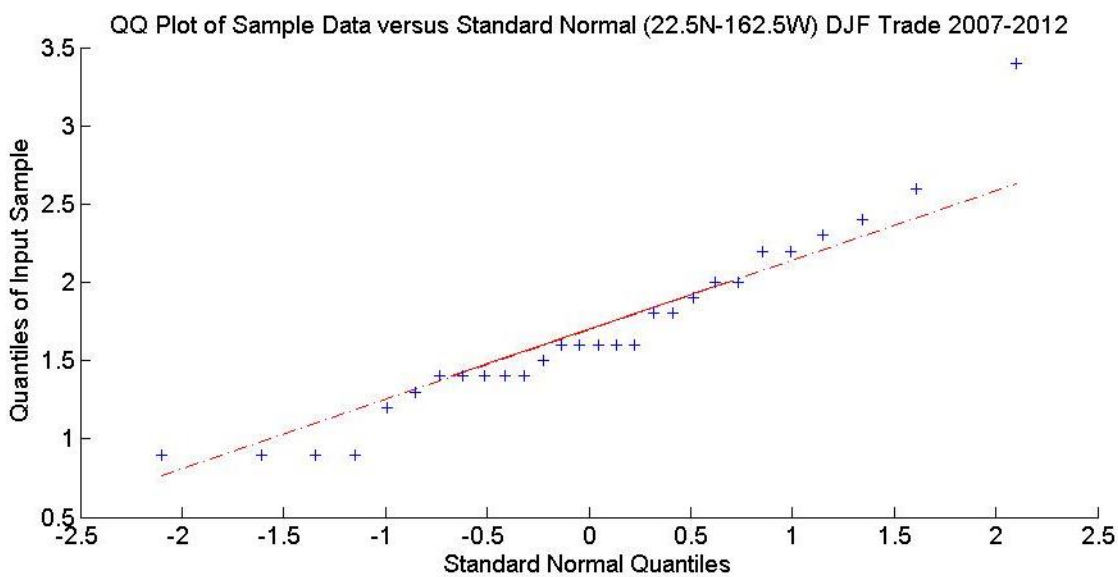

Figure A.5.20. Quantile-quantile plot (q-q plot) of observed median inversion base height z_i (km) for 2.5˚x2.5˚ grid box centered on 22.5˚N, 162.5˚W during DJF-TW 2007-2012. X-axis represents standard normal quantiles; Y-axis represents quantiles of input samples. Each observation is represented by a blue cross. The red line represents the 1-to-1 relationship between a standard normal data distribution and the sampled data set. If blue crosses are oriented along the red diagonal line, the population distribution is considered to be "normal".

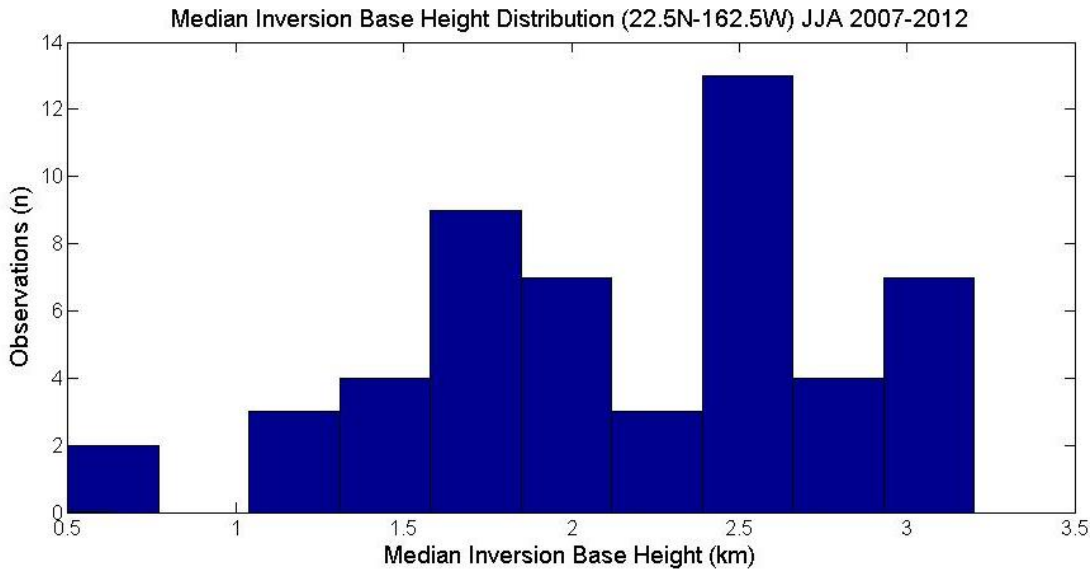

Figure A.5.21. Histogram of observed median inversion base height z_i (km) for 2.5˚x2.5˚ grid box centered on 22.5˚N, 162.5˚W during JJA 2007-2012.

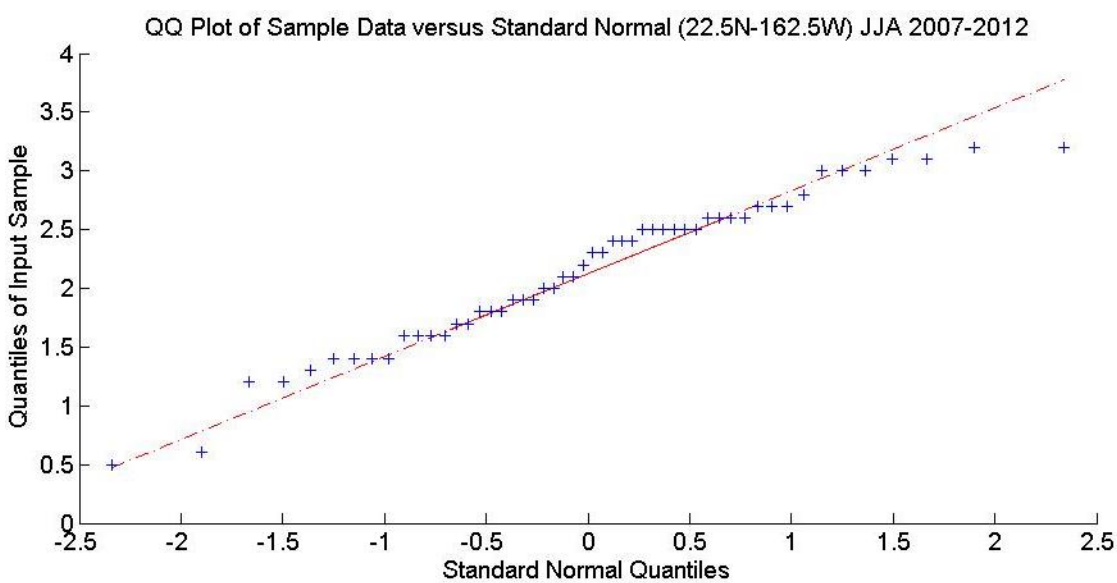

Figure A.5.22. Quantile-quantile plot (q-q plot) of observed median inversion base height z_i (km) for 2.5˚x2.5˚ grid box centered on 22.5˚N, 162.5˚W during JJA 2007-2012. X-axis represents standard normal quantiles; Y-axis represents quantiles of input samples. Each observation is represented by a blue cross. The red line represents the 1-to-1 relationship between a standard normal data distribution and the sampled data set. If blue crosses are oriented along the red diagonal line, the population distribution is considered to be "normal".

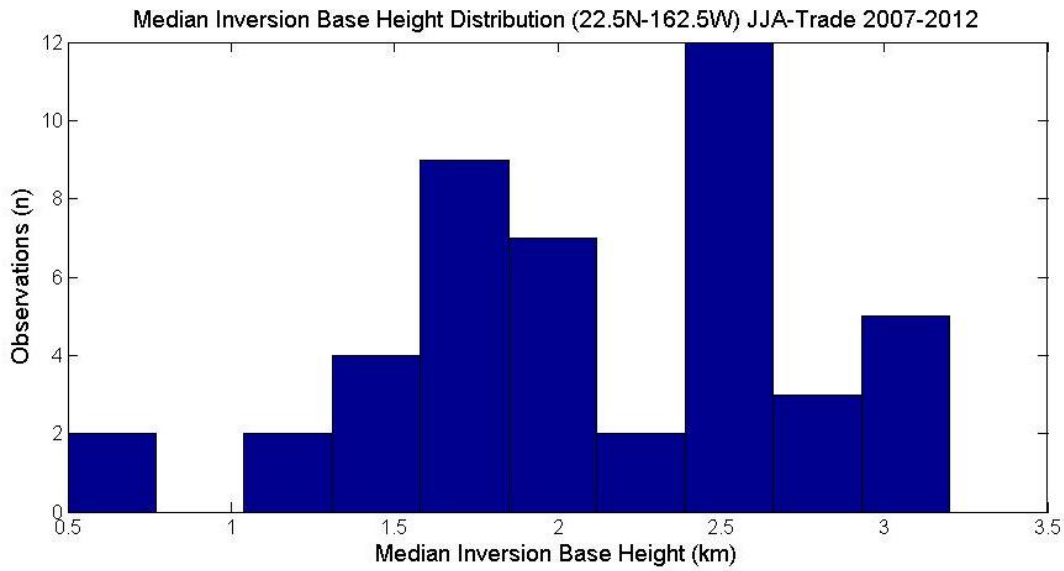

Figure A.5.23. Histogram of observed median inversion base height z_i (km) for 2.5˚x2.5˚ grid box centered on 22.5˚N, 162.5˚W during JJA-TW 2007-2012.

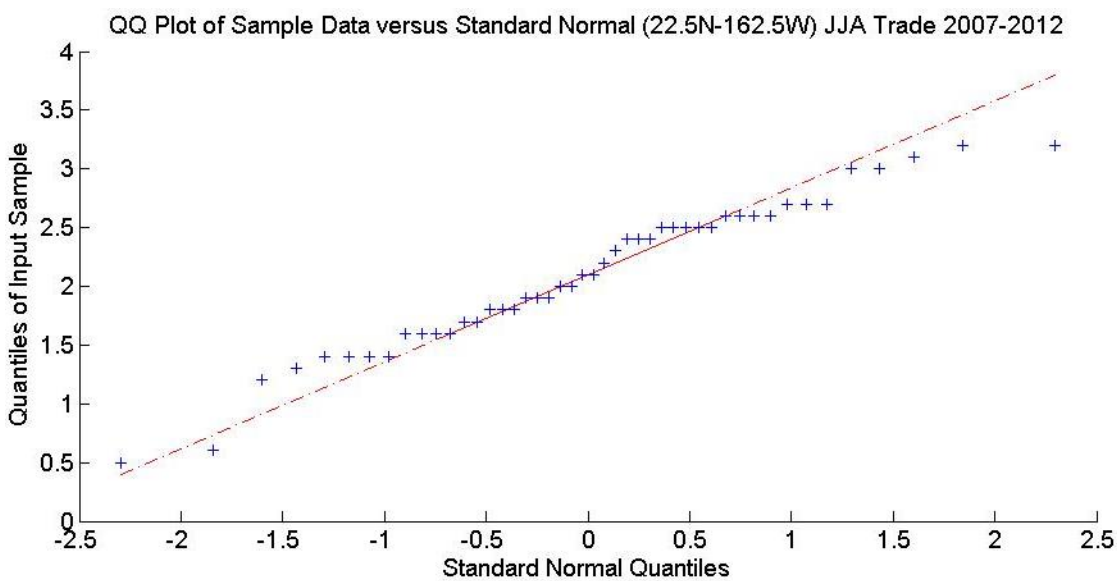

Figure A.5.24. Quantile-quantile plot (q-q plot) of observed median inversion base height z_i (km) for 2.5˚x2.5˚ grid box centered on 22.5˚N, 162.5˚W during JJA-TW 2007-2012. X-axis represents standard normal quantiles; Y-axis represents quantiles of input samples. Each observation is represented by a blue cross. The red line represents the 1-to-1 relationship between a standard normal data distribution and the sampled data set. If blue crosses are oriented along the red diagonal line, the population distribution is considered to be "normal".

Bibliography

Albrecht, B. A., A.K. Betts, W.H. Schubert, and S.K. Cox, 1979: A model of the thermodynamic structure of the trade-wind boundary layer: Part I. Theoretical formulation and sensitivity tests. *J Atmos. Sci.*, **36**, 73-89.

Albrecht, B. A., C. S. Bretherton, D. Johnson, W. H. Schubert, and A. S. Frisch, 1995: The Atlantic Stratocumulus Transition Experiment—ASTEX. *Bull. Amer. Meteor. Soc.*, **76**, 889–904. doi: http://dx.doi.org/10.1175/1520-0477(1995)076<0889:TASTE>2.0.CO;2

Anthes, R. A., C. Rocken, and Y.H. Kuo, 2000: Applications of COSMIC to meteorology and climate. *Terrestrial Atmospheric and Oceanic Sciences*, **11**(**1**), 115-156.

Anthes, R.A., and Coauthors 2008: The COSMIC/FORMOSAT-3 Mission – Early Results. *Bull. Amer. Meteor. Soc.,* **89-3,** 313-333. DOI:10.1175/BAMS-89-3-313.

Ao, C. O., D. E. Waliser, S. K. Chan, J.-L. Li, B. Tian, F. Xie, and A. J. Mannucci, 2012: Planetary boundary layer heights from GPS radio occultation refractivity and humidity profiles, *J. Geophys. Res.*, **117**, D16117, doi:10.1029/2012JD017598.

Ao, C.O., T. K. Chan, B. A. Iijima, J.L. Li, A. J. Mannucci, T. Teixeira, B. Tian, and D. E. Waliser, 2008: Planetary boundary layer information from GPS radio occultation measurements. *Proc. GRAS SAF Workshop on Applications of GPSRO Measurements*, Reading, U. K., The EUMESTAT Network of Satellite Application Facilities, 123–131. http://www.romsaf.org/Workshops/agrom_prog/Ao.pdf

Aumann, H. H., M.T. Chahine, C. Gautier, M.D. Goldberg, E. Kalnay, L.M. McMillin, and J. Susskind, 2003: AIRS/AMSU/HSB on the Aqua mission: Design, science objectives, data products, and processing systems. *IEEE Transactions on Geoscience and Remote Sensing*, **41**(**2**), 253-264.

Basha, G., and M. V. Ratnam, 2009: Identification of atmospheric boundary layer height over a tropical station using high-resolution radiosonde refractivity profiles: Comparison with GPS radio occultation measurements, *J. Geophys. Res.*, **114**, D16101, doi:10.1029/2008JD011692.

Bean, B. R., and E. J. Dutton, 1968: *Radio Meteorology*. Dover, 435 pp.

Betts, Alan K., and W. Ridgway, 1989: Climatic equilibrium of the atmospheric convective boundary layer over a tropical ocean. *J. Atmos. Sci.*, **46**, 2621–2641. doi:http://dx.doi.org/10.1175/1520-0469(1989)046<2621:CEOTAC>2.0.CO;2

Bingaman, J. B., 2005: Characteristics of the trade wind inversion over Hawaii. M.S. thesis, Dept. of Meteorology, University of Hawaii at Mānoa, 158 pp.

Blake, D., 1933: Remarkably low humidities aloft over San Diego, California. *Mon Wea. Rev.*, **61**, 170.

Bowie, E.H., 1933: The summer night-time clouds of Santa Clara Valley, California. *Mon. Wea. Rev.*, **61**, 40-41.

Braun S.A., and W.K. Tao, 2000: Sensitivity of high-resolution simulations of hurricane Bob (1991) to planetary boundary layer parameterizations. *Mon Wea. Rev.*, **128**, 3941–3961.

Brill, K., and B. Albrecht, 1982: Diurnal variation of the trade-wind boundary layer. *Mon. Wea. Rev.*, **110**, 601–613. doi:http://dx.doi.org/10.1175/1520-0493(1982)110<0601:DVOTTW>2.0.CO;2

Cao, G., T.W. Giambelluca, D.E. Stevens, and T.A. Schroeder, 2007: Inversion variability in the Hawaiian trade wind regime. *J. Clim.*, **20**, 1145-1158.

Carbone, R.E., J.D. Tuttle, W.A. Cooper, V. Grubišic, and W.C. Lee, 1998: Trade-wind rainfall near the windward coast of Hawaii. *Mon. Wea. Rev.*, **126**, 2847-2863. doi: 10.1175/1520-0493(1998)126%3C2847:TWRNTW%3E2.0.CO;2.

Chen, Y.L., and A. J. Nash, 1994: Diurnal variation of surface airflow and rainfall frequencies on the island of Hawaii. *Mon. Wea. Rev.*, **122**, 34–56. doi: http://dx.doi.org.eres.library.manoa.hawaii.edu/10.1175/1520-0493(1994)122<0034:DVOSAA>2.0.CO;2

Chen, Y.L., and J. Feng, 1995: The influences of inversion height on precipitation and airflow over the island of Hawaii. *Mon. Wea. Rev.*, **123**, 1660–1676. doi: http://dx.doi.org/10.1175/1520-0493(1995)123<1660:TIOIHO>2.0.CO;2

Chen, Y. L., and J. Feng, 2001: Numerical simulations of airflow and cloud distributions over the windward side of the island of Hawaii. Part I: The effects of the trade-wind inversion*. *Mon. Wea. Rev.*, **129**, 1117–1134. doi: http://dx.doi.org/10.1175/1520-0493(2001)129<1117:NSOAAC>2.0.CO;2

Cheng, C.Z., Y.H. Kuo, R. A. Anthes, and L. Wu, 2006: Satellite constellation monitors global and space weather. *EOS, Trans. Amer. Geophys. Union,* **87,** 166–167.

Chu, P.S., 1995: Hawaii rainfall anomalies and El Niño. *J. Climate*, **8**, 1697–1703. doi:http://dx.doi.org.eres.library.manoa.hawaii.edu/10.1175/1520-0442(1995)008<1697:HRAAEN>2.0.CO;2

Ciesielski, P.E., W.H. Schubert, and R. H. Johnson, 2001: Diurnal variability of the marine boundary layer during ASTEX. *J. Atmos. Sci.*, **58(16)**, 2355-2376.

COSMIC Data Analysis and Archive Center, Constellation (CDAAC) Observing System for Meteorology, Ionosphere and Climate, University Corporation for Atmospheric Research, 2013: Atmospheric Profiles from COSMIC Occultation Data. Research Data Archive at the National Center for Atmospheric Research, Computational and Information Systems Laboratory, Boulder, CO. [Available online at http://rda.ucar.edu/datasets/ds723.0.] Accessed§ 03 April 2014.

Climate Prediction Center/National Centers for Environmental Prediction/National Weather Service/NOAA/U.S. Department of Commerce, 2011: NOAA CPC Morphing Technique (CMORPH) Global Precipitation Analyses. Research Data Archive at the National Center for Atmospheric Research, Computational and Information Systems Laboratory, Boulder, CO. [Available online at http://rda.ucar.edu/datasets/ds502.0/.] Accessed§ 27 March 2014.

Cucurull, L., Y.H. Kuo, D. Barker, S., and R. H. Rizvi, 2006: Assessing the impact of simulated COSMIC GPS radio occultation data on weather analysis over the Antarctic: A case study. *Mon. Wea. Rev.*, **134**, 3283–3296. doi: http://dx.doi.org/10.1175/MWR3241.1

DeCaria, A. J., 2007: Relating static energy to potential temperature: A caution. *J. Atmos. Sci.*, **64**, 1410–1412. doi: http://dx.doi.org/10.1175/JAS3906.1

Earth Systems Research Laboratory (ERSL), cited 2014: Multivariate ENSO index. [Available online at http://www.esrl.noaa.gov/psd/enso/mei/]

Esteban, M. A., and Y.L. Chen, 2008: The impact of trade wind strength on precipitation over the windward side of the Island of Hawaii. *Mon. Wea. Rev.*, **136(3)**, 913-928.

Garza, J. A., P.S. Chu, C. W. Norton, and T. A. Schroeder, 2012: Changes of the prevailing trade winds over the island of Hawaii and the North Pacific, *J. Geophys. Res.*, **117**, D11109, doi:10.1029/2011D016888

The Grid Analysis and Display System (GrADS), 2011 (Version 2.0) [Software], Calverton, MD, COLA/IGES. http://www.iges.org/grads/.

Grindinger, C.M., 1992: Temporal variability of the trade wind inversion measured with a boundary layer vertical profiler. M.S. thesis, Dept. of Meteorology, University of Hawaii at Mānoa, 93 pp.

Guo, P., Y. H. Kuo, S.V. Sokolovskiy, and D.H. Lenschow, 2011: Estimating atmospheric boundary layer depth using COSMIC radio occultation data. *J. Atmos. Sci.*, **68**, 1703-1713. DOI: 10.1175/2011JAS3612.1

Hafner, J., S. P. Xie, 2003: Far-field simulation of the Hawaiian wake: Sea surface temperature and orographic effects*. *J. Atmos. Sci.*, **60**, 3021–3032. doi: http://dx.doi.org/10.1175/1520-0469(2003)060<3021:FSOTHW>2.0.CO;2

Hajj, G. A., C. O. Ao, B. A. Iijima, D. Kuang, E. R. Kursinski, A. J. Mannucci, T. K. Meehan, L. J. Romans, M. de la Torre Juarez, and T. P. Yunck, 2004: CHAMP and SAC-C atmospheric occultation results and intercomparison. *J. Geophys. Res.*, **109**, D06109,doi:10.1029/2003JD003909.

Hartley, T. M., and Y. L. Chen, 2010: Characteristics of summer trade wind rainfall over Oahu. *Wea. Forecasting*,**25**,1797–1815.doi: http://dx.doi.org.eres.library.manoa.hawaii.edu/10.1175/2010WAF2222328.1

Healy, S. B., 2008: Assimilation of GPS radio occultation measurements at ECMWF. *Proc. GRAS SAF Workshop on Assimilation of GPS Radio Occultation Measurements (AGROM)*, Reading, UK, The EUMESTAT Network of Satellite Application Facilities, 99–109.

Healy, S. B., A. M. Jupp, and C. Marquardt, 2005: Forecast impact experiment with GPS radio occultation measurements, *Geophys. Res. Lett.*, **32**, L03804. doi:10.1029/2004GL020806.

Hitzl, D.E., 2013: Numerical Simulations and Observations of Airflow Through the Alenuihāhā Channel. M.S. thesis, Dept. of Meteorology, University of Hawaii at Mānoa, 121 pp.

Hitzl., D.E., Y.L. Chen, and H.V. Nguyen, 2014: Numberical simulations and observations of airflow through the ʻAlenuihāhā Channel, Hawaii, *Mon. Wea. Rev.* (*submitted*).

Holtslag, A. A., and M. Boville, 1993: Local versus nonlocal boundary-layer diffusion in a global climate model. *J Clim*., **6**, 1825-1842.

Hong S.Y., and H.L. Pan, 1996: Nonlocal boundary layer vertical diffusion in a medium-range forecast model. *Mon. Wea. Rev.*, **124,** 2322–2339.

Joyce, R. J., J. E. Janowiak, P. A. Arkin, and P. Xie, 2004: CMORPH: A method that produces global precipitation estimates from passive microwave and infrared data at high spatial and temporal resolution. *J. Hydromet.*, 5, 487-503.

Jia, Y., H. R. Calil, E. P. Chassignet, E. J. Metzger, J. T. Potemra, K. J. Richards, and A. J. Wallcraft, 2011: Generation of mesoscale eddies in the lee of the Hawaiian islands. *J. Geophys. Res.*, **116**, C11009, doi:10.1029/2011JC007305.

Juvik S., 1998: *Atlas of Hawai'i* 3rd Ed., University of Hawaii Press. 333 pp.

Kloesel, K. A., 1992: A 70-year history of marine stratocumulus cloud field experiments off the coast of California. *Bull. Amer. Meteor. Soc.*, **73**, 1581–1585. doi: http://dx.doi.org/10.1175/1520-0477(1992)073<1581:AYHOMS>2.0.CO;2

Kodama, K.R., and G.M, Barnes, 1997: Heavy rain events over the south-facing slopes of Hawaii: Attendant conditions. *Wea. Forecasting*, **12**, 347-367.

Kodama, K.R. and S. Businger, 1998: Weather and forecasting challenges in the Pacific Region of the National Weather Service. *Wea. Forecasting*, **13,** 253–276.

Kuo, Y.H., S. Sokolovskiy, R. A. Anthes, and F. Vandenberghe, 2000: Assimilation of GPS radio occultation data for numerical weather prediction. *Applications of Constellation Observing System for Meteorology, Ionosphere and Climate*, L.-C. Lee, C. Rocken, and R. Kurinski, Eds., Springer, 157–186.

Kuo, Y. H., C. Rocken, R.A. Anthes, 2005: Constellation Observing System for Meteorology, Ionosphere, and Climate (COSMIC): An Overview. University Corporation for Atmospheric Research, Boulder, CO. [Available online at http://nldr.library.ucar.edu/repository/assets/osgc/OSGC-000-000-001-230.pdf]

Kuo, Y.H., H. Liu, Z. Ma, S. Sokolovskiy, P. Guo, R. A. Anthes, N. Yen, and J-J. Miau, 2008: COSMIC Status and Prospects for COSMIC-II. *Proc. GRAS SAF Workshop on Assimilation of GPS Radio Occultation Measurements (AGROM)*, Reading, UK, The EUMESTAT Network of Satellite Application Facilities, 23-35.

Kursinski, E. R., G.A. Hajj, J.T. Schofield, R.P. Linfield, K.R, Hardy, 1997: Observing Earth's atmosphere with radio occultation measurements using the global positioning System. *J. Geophys. Res.: Atmospheres (1984–2012)*, **102(D19)**, 23429-23465.

Leopold, L. B., 1949: The interaction of trade-wind and sea breeze over Hawaii. *J. Meteor.*, **6**, 312–320. doi: http://dx.doi.org/10.1175/1520-0469(1949)006<0312:TIOTWA>2.0.CO;2

Li X., and Z. Pu, 2008: Sensitivity of numerical simulation of early rapid intensification of hurricane Emily (2005) to cloud microphysical and planetary boundary layer parameterizations. *Mon. Wea. Rev.*, **136**, 4819–4838

Lilly, D.K., 1968: Models of cloud-topped mixed layers under strong inversions. *Quart. J. Roy. Meteor. Soc.*, **94**, 292-309.

Malkus, J.S., 1956: On the maintenance of the trade-winds., *Tellus* VIII, **3**, 335-350.

Medeiros, B., A. Hall, and B. Stevens, 2005: What controls the mean depth of the PBL?, *J. Clim.*, **18**, 3157–3172.

The NCAR Command Language, 2012: (Version 6.1.0) [Software]. Boulder, CO: UCAR/NCAR/CISL/VETS. http://dx.doi.org/10.5065/D6WD3XH5

National Centers for Environmental Prediction/National Weather Service/NOAA/U.S. Department of Commerce, 2000: NCEP FNL Operational Model Global Tropospheric Analyses, continuing from July 1999. Research Data Archive at the National Center for Atmospheric Research, Computational and Information Systems Laboratory, Boulder, CO. [Available online at http://rda.ucar.edu/datasets/ds083.2.] Accessed§ 28 February 2014.

Neiburger, M., 1960: The relation of air mass structure to the field of motion over the eastern North Pacific ocean in summer. *Tellus*, **12**, 31-40.

Neiburger, M., D. S. Johnson, and C.W. Chien, 1961: Studies of the structure of the atmosphere over the Eastern Pacific Ocean in summer I: The inversion over the Eastern North Pacific Ocean. Univ. of Calif. Publications in Meteorology, Vol. 1, No. 1, 94pp. http://derecho.math.uwm.edu/classes/TropMet/inversion.pdf

Nickerson, E.C., and M.A. Dias, 1981: On the existence of atmospheric vortices downwind of Hawaii during the HAMEC project. *J. App. Met.*, **20**, 868-873.

Nutter, P. A., S. L. Mullen, and D. P. Baumhefner, 1998: The impact of initial condition uncertainty on numerical simulations of blocking. *Mon. Wea. Rev*., **126**, 2482–2502.

Panofsky, H.A. and G.W. Brier, 1958: *Some Applications of Statistics to Meteorology*. Pennsylvania State University, 224 pp.

Petterssen, S., 1938: On the causes and forecasting of the California fog. *Bull. Amer. Meteor. Soc.*, **19**, 49.

Piazzi-Smyth, C., 1858: Astronomical expedition on the Peak of Teneriffa. *Trans. Roy. Soc. London*, **148**, 465-533.

Ramage, C. S., and T. A. Schroeder, 1999: Trade Wind Rainfall atop Mount Waialeale, Kauai*. *Mon. Wea. Rev.*, **127**, 2217–2226. doi: http://dx.doi.org/10.1175/1520-0493(1999)127<2217:TWRAMW>2.0.CO;2

Riehl, H., T.C. Yeh, J.J. Malkus, and N.E. LaSeur, 1951: The northeast trade of the Pacific Ocean. *Quart. J. Roy. Meteor. Soc.*, **77**, 598-626.

Riehl, H., 1962: Jet streams of the atmosphere. *Atmospheric Science Paper No. 32*, Colorado State University, Fort Collins Colorado CER63HR35. 125 pp.

Riehl, H., 1979: *Climate and Weather in the Tropics*, Academic, London, UK, 611 pp.

Saha, S., and Coauthors, 2010: The NCEP Climate Forecast System Reanalysis. Bull. Amer. Meteor. Soc., 91, 1015-1057. doi: http://dx.doi.org/10.1175/2010BAMS3001.1

Schreiner, W., D. Hunt, C. Rocken, and S. Sokolovskiy, 2002: Radio occultation data processing at the COSMIC Data Analysis and Archival Center (CDAAC). *1st CHAMP Science Meeting*, Potsdam, Germany, 12 pp.

Schreiner, W., C. Rocken, S. Sokolovsky, S. Syndergaard, and D. Hunt, 2007: Estimates of the precision of GPS radio occultations from the COSMIC/FORMOSAT-3 mission. *Geophys. Res. Lett*., **34**, L04808, doi:10.1029/2006GL027557.

Schroeder T.A., B.J. Kilonsky, and B.N. Meisner, 1977: Diurnal variation in rainfall and cloudiness. WRRC technical report, 112. 75 pp. University of Hawaii at Mānoa. [Available online at http://scholarspace.manoa.hawaii.edu/bitstream/handle/10125/1852/wrrctr112.PDF?sequence=1]

Schroeder, T. A., 1993: Climate controls. *Prevailing Trade Winds: Weather and Climate in Hawai'i*, M. Sanderson, Ed., University of Hawaii Press, 12-36.

Schroeder, T.A., and T. Giambelluca, 1998: Climate. Atlas of Hawaii, S. Juvik, 3rd Ed., University of Hawai'i Press, 49-59.

Seidel, D. J., C. O. Ao, and K. Li, 2010: Estimating climatological planetary boundary layer heights from radiosonde observations: Comparison of methods and uncertainty analysis, *J. Geophys. Res.*, **115**, D16113, doi:10.1029/2009JD013680.

Shin, H. H., S.Y.Hong, 2011: Intercomparison of planetary boundary-layer parameterizations in the WRF model for a single day from CASES-99. *Boundary-Layer Meteorology*, **139(2)**, 261-281.

Simon, R. L., 1977: The summertime stratus over the offshore waters of California. *Mon. Wea. Rev.*, **105**, 1310-1314.

Skamarock W.C., J.B. Klemp, J. Dudhia, D.O. Gill, D.M. Barker, M.G Duda, X.Y. Huang, W.Wang, and J.G. Powers, 2008: A description of the advanced research WRF Version 3. NCAR Technical Note NCAR/TN-475+STR, 125 pp.

Small, R. J., S.P. Xie, J. Hafner, 2005: Satellite observations of mesoscale ocean features and copropagating atmospheric surface fields in the tropical belt, *J. Geophys. Res.*, **110**, C02021, doi:10.1029/2004JC002598.

Smolarkiewicz, P. K., R. M. Rasmussen, and T. L. Clark, 1988: On the dynamics of Hawaiian cloud bands: Island forcing. *J. Atmos. Sci.*, **45**, 1872–1905. doi: http://dx.doi.org/10.1175/1520-0469(1988)045<1872:OTDOHC>2.0.CO;2

Sokolovskiy, S. V., 2003: Effect of superrefraction on inversions of radio occultation signals in the lower troposphere, *Radio Sci.*, **38**, 1058, doi:10.1029/2002RS002728.

Sokolovskiy, S. V., Y.-H. Kuo, C. Rocken, W. S. Schreiner, D. Hunt, and R. A. Anthes, 2006: Monitoring the atmospheric boundary layer by GPS radio occultation signals recorded in the open-loop mode, *Geophys.Res. Lett.*, **33**, L12813, doi:10.1029/2006GL025955.

Sokolovskiy, S. V., C. Rocken, D. H. Lenschow, Y.-H. Kuo, R. A. Anthes,W. S. Schreiner, and D. Hunt, 2007: Observing the moist troposphere with radio occultation signals from COSMIC, *Geophys. Res. Lett.*, **34**,L18802, doi:10.1029/2007GL030458.

Stull, R.B., 2000: *Meteorology for Scientists and Engineers 2nd Ed.*, Brooks/Cole, 502 pp.

Sverdrup, H. U., 1917: Der nordatlantische Passatinversion *Veroffentl. D Geoph. Inst .d Univ. Leipzig*, Bd. II, Heft I

Tran, L. T., 1995: Relationship between the inversion and rainfall on the Island of Maui. M.S. thesis, Dept. of Geography, University of Hawaii at Mānoa, 115 pp.

Trenberth K. E., and D. P. Stepaniak, 2003: Seamless poleward atmospheric energy transport and implications for the Hadley circulation. *J. Clim.*, **16,** 3706–3722.

Vernon, E..M., 1936: The diurnal variation in ceiling height beneath stratus clouds. *Mon Wea Rev.*, **64**, 14-16.

von Engeln, A., J. Teixeira, J. Wickert, and S. A. Buehler, 2005: Using CHAMP radio occultation data to determine the top altitude of the planetary boundary layer, *Geophys. Res. Lett.*, **32,** L06815, doi:10.1029/2004GL022168.

VonFicker, H., 1936: Die Passatinversion. *Veroffentl.d. Meteorol. Inst. d. Univ. Berlin*, Dd., I, Heft 4.

Ware, R., and Coauthors, 1996: GPS sounding of the atmosphere from low Earth orbit: Preliminary results. *Bull. Amer. Meteor. Soc.*, **77,** 19–40.

Weather Research and Forecasting Model Simulations at University of Hawaii – Mānoa: http://www.soest.hawaii.edu/MET/Faculty/wrf/arw/.

Wickert, J., C. Reigber, G. Beyerle, R. K¨onig,C. Marquardt, T. Schmidt, L. Grunwaldt, R. Galas, T. K. Meehan, W. G. Melbourne, and K. Hocke, 2001: Atmosphere sounding by GPS radio occultation: First results from CHAMP. *Geophys. Res. Lett.*, **28,** 3263–3266.

Wood, R., and C. S. Bretherton, 2004: Boundary layer depth, entrainment, and decoupling in the cloud-capped subtropical and tropical marine boundary layer. *J. Clim.*,**17**,3576–3588.doi:http://dx.doi.org/10.1175/1520-0442(2004)017<3576:BLDEAD>2.0.CO;2

Wood, R., and Coauthors., (2011) The VAMOS Ocean-Cloud-Atmosphere-Land Study Regional Experiment (VOCALS-REx): goals, platforms, and field operations. *Atmos. Chem. Phys.*, **11**, 627-654, doi:10.5194/acp-11-627-2011.

Wood, R., (2012) Stratocumulus Clouds. *Mon. Wea. Rev.*, **140**, 2373–2423. doi: http://dx.doi.org/10.1175/MWR-D-11-00121.1

Wu, X., X.Wang, and D. R. Lu, 2014: Retrieval of vertical distribution of tropospheric refractivity through ground based GPS observation. *Adv. Atmos. Sci.*, **31(1)**, 37–47, doi: 10.1007/s00376-013-2215-z.

Wulfmeyer, V., and T. Janjić, 2005: Twenty-four hour observations of the marine boundary layer using shipborne NOAA high-resolution doppler lidar. *J. Appl. Meteor.*, **44**, 1723–1744. doi: http://dx.doi.org/10.1175/JAM2296.1

Xie, F., S. Syndergaard, E.R. Kursinski, and B.M. Herman, 2006: An approach for retrieving marine boundary layer refractivity from GPS occultation data in the presence of super-refraction, *J. Atmos. Ocean Tech*, **23**, 1629-1644.

Xie, F., D. L. Wu, C. O. Ao, E. R. Kursinski, A. J. Mannucci, and S. Syndergaard, 2010: Super-refraction effects on GPS radio occultation refractivity in marine boundary layers, *Geophys. Res. Lett.*, **37**, L11805, doi:10.1029/2010GL043299.

Xie, F., D. L.Wu, C.O. Ao, and A.J. Mannucci, 2010: Atmospheric diurnal variations observed with GPS radio occultation soundings, *Atmos. Chem. Phys.*, **10**, 6889-6899. doi:10.5194/acp-10-6889-2010.

Xie, F., D.L. Wu, C.O. Ao, A.J. Mannucci, and E.R. Kursinski, 2012: Advances and limitations of atmospheric boundary layer observations with GPS occultation over southeast Pacific Ocean, *Atmos. Chem. Phys.*, **12**, 903-918. doi:10.5194/acp-12-903-2012.

Yang, Y., S.P. Xie, and J. Hafner, 2008a: The thermal wake of Kauai island: Satellite observations and numerical simulations, *J. Clim.*, **21**, 4568-4586, doi:10.1029/2008JD009889.

Yang, Y., S.P. Xie, and J. Hafner, 2008b: Cloud patterns lee of Hawaii Island: A synthesis of satellite observations and numerical simulation. J. Geophys. Res.-Atmos., 113, D1512

Yang, Y., J. Ma, and S.P. Xie, 2008: Observations of the trade wind wakes of Kauai and Oahu, *Geophys. Res. Lett.*, **35**, L04807, doi:10.1029/2007GL031742.

Yen, N.L., C. J. Fong, C. H. Chu, J.J. Miau, Y. A. Liou, and Y. H. Kuo 2010: Global GNSS Radio Occultation Mission for Meteorology, Ionosphere & Climate, *Aerospace Technologies Advancements*, Thawar T. Arif (Ed.), ISBN: 978-953-7619-96-1, InTech, DOI: 10.5772/6928. [Available online at: http://www.intechopen.com/books/aerospace-technologies-advancements/global-gnss-radio-occultation-mission-for-meteorology-ionosphere-amp-climate].

Zhang, C., Y. Wang, A. Lauer, K. Hamilton, and F. Xie, 2012: Cloud base and top heights in the Hawaiian region determined with satellite and ground-based measurements, *Geophys. Res. Lett.*, **39**, *L15706*, doi:10.1029/2012GL052355.

Zhou, C. and Y.L. Chen, 2014: Assimilation of GPS RO refractivity data and its impact on simulations of trade wind inversion and a winter cold front in Hawaii. A Special Issue on Weather Forecasting, *Nat. Sci.*, **6**, 605-614, doi:10.4236/ns.2014.68060.